Thesis for the Degree of Doctor of Engineering

Study on fabrication process with photopolymerization reaction under magnetic field for crystal-oriented ceramics

(磁場下での光重合反応を用いた結晶配向セラミックスの製造法に関する研究)

by

SHOKO BABA

(馬場 翔子)

Department of Science of Technology Innovation
Nagaoka University of Technology

March 2020

Acknowledgments

This thesis is based on the research work, which was performed under Assoc. Prof. Satoshi Tanaka in Department of Materials Science and Technology at Nagaoka University of Technology. I would like to express my sincere gratitude to Assoc. Prof. Satoshi Tanaka for his invaluable guidance, support and encouragement through 7 years. I could not complete this thesis without his guidance.

I would like to express my thanks to Prof. Tadachika Nakayama, Assoc. Prof. Tomoichiro Okamoto, Assoc. Prof. Tsuyoshi Honma in Nagaoka University of Technology and Prof. Yutaka Doshida in Ashikaga University for their fruitful discussions.

I would like to express my gratitude to all members of Tanaka laboratory for their support and friendship. The past and current students in Tanaka laboratory have contributed to making pleasant surroundings so that I could complete my work in doctoral course.

Additionally, thanks to Prof. Alexandre Maître in Ceramic Research laboratory at University of Limoges. I could get precious opportunities to study and to feel cultures in France. I'd like to express my thanks to him for his supports and kindness for me.

Finally, I am deeply grateful to my family; grandfather, grandmother, father, mother and sister, for their continuous support and understanding of what I want.

Shoko Baba
March 2020

Contents

Chapter 1

Introduction

1.1 GENERAL INTRODUCTION

Ceramics fabricated under the controlled techniques are newly called *advanced ceramics* to distinguish it from *traditional ceramics*. Now, they include ceramics for structural applications at elevated temperatures (structural ceramics) and ceramics for electrical, magnetic, electric, optical, and biological applications (occasionally referred to as functional ceramics) [1]. In the past few decades, the techniques for the fabrication of ceramics products have made progress to achieve the superior properties for the intended applications. And they have led to an expansion of ceramic applications. Purity, particle size distribution and availability of raw powders were carefully controlled. The forming methods to produce the required shapes were developed, and the conditions of sintering to obtain the preferable microstructure were carefully managed.

Recently, the needs of the market have demanded that the functional properties of advanced ceramics be further improved. Many of the functional properties of ceramics generally depend on their microstructure and crystals orientation as well as their chemical composition, crystal structure, and bonding type [2], as shown in Figure 1.1. However, many of the functional properties of polycrystalline ceramics (e.g., thermal conductivity, optical property, dielectric constant, and electrical conductivity) are lower than the intrinsic properties of a material, that is, properties of single-crystal. This is because each ceramic crystal grain has a random orientation (Figure 1.2 (a)). If crystals were oriented (Figure 1.2 (b), the excellent original properties are expected to appear. The crystal-oriented polycrystalline ceramics have attracted the attention of many researchers for over many years.

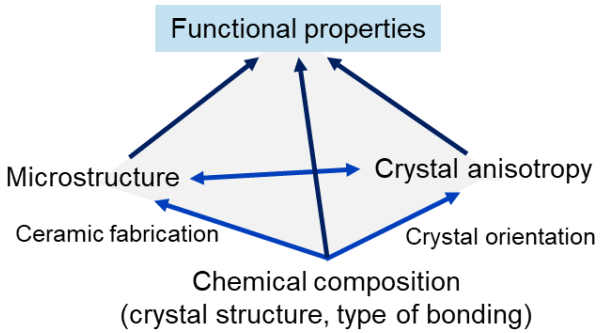

FIGURE 1.1 The important relationships in ceramic fabrication.

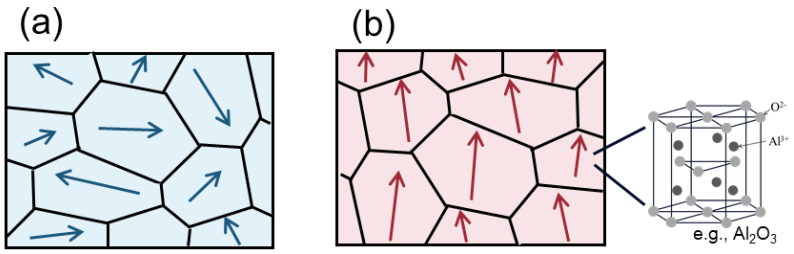

FIGURE 1.2 Microstructure of polycrystalline ceramics (a) random oriented and (b) crystal-oriented ceramics.

TABLE 1.1 Summary of major alignment techniques.

Technique	Particle shape versatility	Driving force	Alignment direction capability	Density of sintered body
Hot-working	Not well characterized	Pressure	Limited	Medium
Doctor blade	Limited	Shear force	Limited	Medium-high
Electric field	Moderate	Electric torque	Moderate	-
Magnetic field	High	Magnetic torque	High	Medium-high

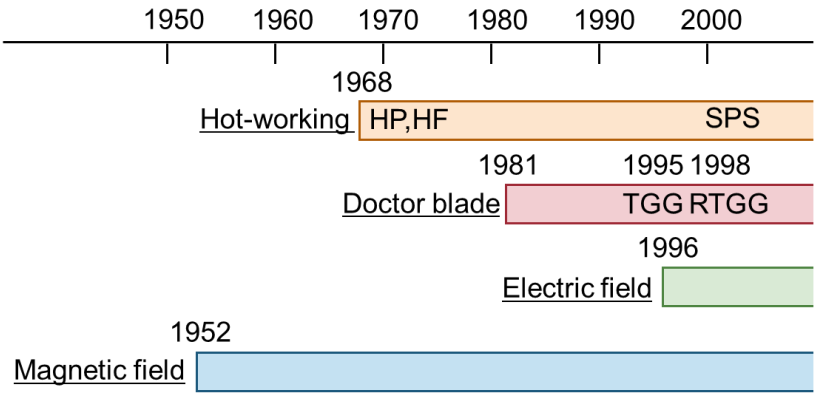

FIGURE 1.3 The history of development of orientation techniques.

1.2 CRYSTAL-ORIENTATION TECHNIQUES

The control of the crystal axes in polycrystalline ceramics is an important technique in order to give the excellent functional properties of ceramics. The fabrication methods are roughly divided into three groups; a mechanical stress field containing hot-working and doctor blade techniques, an electric field alignment or a magnetic field orientation [3]-[6]. The characteristics of those techniques are summarized in Table 1.1 and in more detail below. The history of the development of those orientation techniques is shown in Fig. 1.3.

1.2.1 Mechanical Stress Field

The textured ceramics have been produced by using the technique applied the mechanical stress field; hot-working techniques such as hot-pressing or hot-forging, doctor blade techniques including template grain growth and reactive template grain growth. The schematic diagrams of techniques are shown in Fig. 1.4. In the methods, the particles with anisotropic shapes, which are ceramics templates, whiskers, and fibers, are required as seed particles. The anisotropic shape of particles largely limits the orientation direction of particles.

1.2.1.1 Hot-Working Techniques

Hot-pressing (HP) and hot-forging (HF) are the sintering techniques which perform both heat treatment and pressing simultaneously [3],[7]-[13]. The raw powders are filled into a die and sintered under uniaxial pressure. HF is similar to HP, but without the sample confined in a die, as shown in Fig. 1.4 (a) [1]. In sintered bodies fabricated by HP or HF of various materials (e.g., Al_2O_3 [8,9], TiO_2 [10], Y_2O_3 [11], bismuth layer-structured

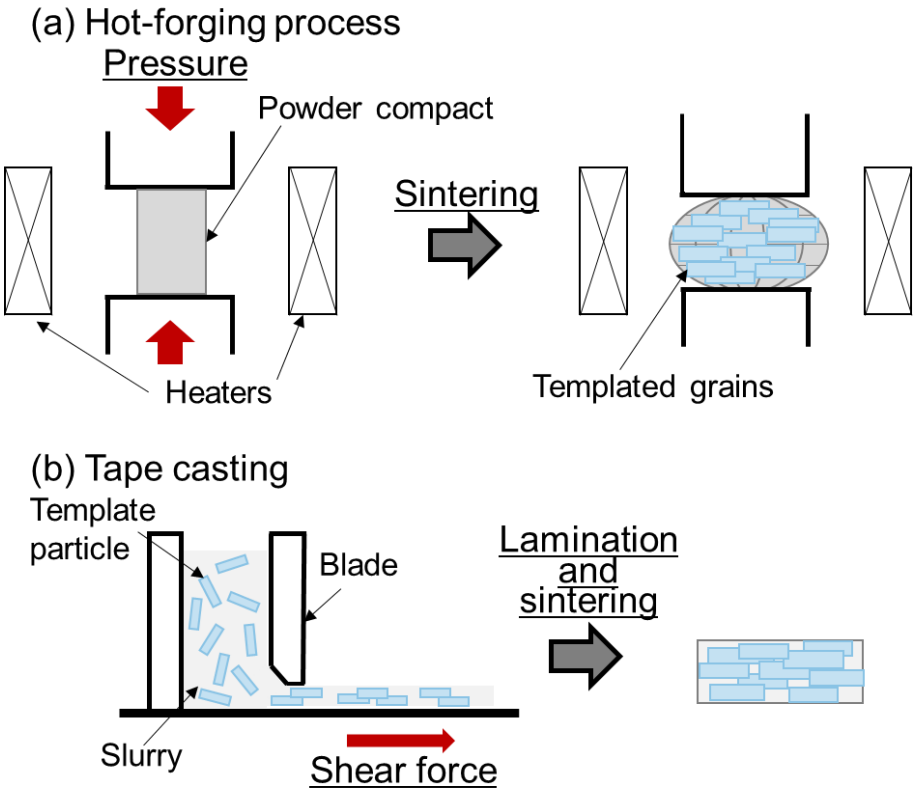

FIGURE 1.4 Schematic diagrams of the fabrication process for textured ceramics by applied mechanical stress. (a) Hot-forging process and (b) tape casting.

type[3,12], tungsten bronze type[13]), the grains grown along the perpendicular to the uniaxial pressing direction were observed. The uniaxial pressing during sintering results in the motion of dislocations in the grains, the plastic deformation, and the slip in the grain boundaries at high temperatures [12]. In these sintering techniques, the densely textured ceramics were fabricated at a temperature lower than the temperature of sintering under normal pressure. However, a severe gradient of shear stresses under the uniaxial pressing resulted in microstructures with nonuniform density, grain sizes and orientation degrees [9,12].

1.2.1.2 Doctor Blade Techniques

The doctor blade technique is the most common approach for tape casting as shown in Fig. 1.4 (b) [2]. The use of this method can be found in the large ceramic electrical industry, e.g., the production of multilayer ceramic capacitor and ceramic IC package. The technique consists of casting a slurry onto a carrier surface and spreading the slurry on a controlled thickness with the edge of a smooth blade. When anisotropically shaped particles were used, the particles were aligned so that the plate face became parallel to the sheet surface by shear force [14]-[17]. After sintering the laminate, the sintered bodies with a high degree of orientation could be easily fabricated. However, the density was low because of the existence of large pores between the aligned large grains.

To hinder the formation of large pores, the template grain growth (TGG) method was proposed [18,19]. The TGG was first applied to structure ceramics [18]-[21], and extended to piezoelectric ceramics with bismuth layer-structured ferroelectrics (BLSFs) and tungsten bronze-structured ferroelectrics (TBSLs) [4],[22,23]. A schematic of microstructure development by TGG is shown in Fig. 1.5 [4]. The feature of the TGG

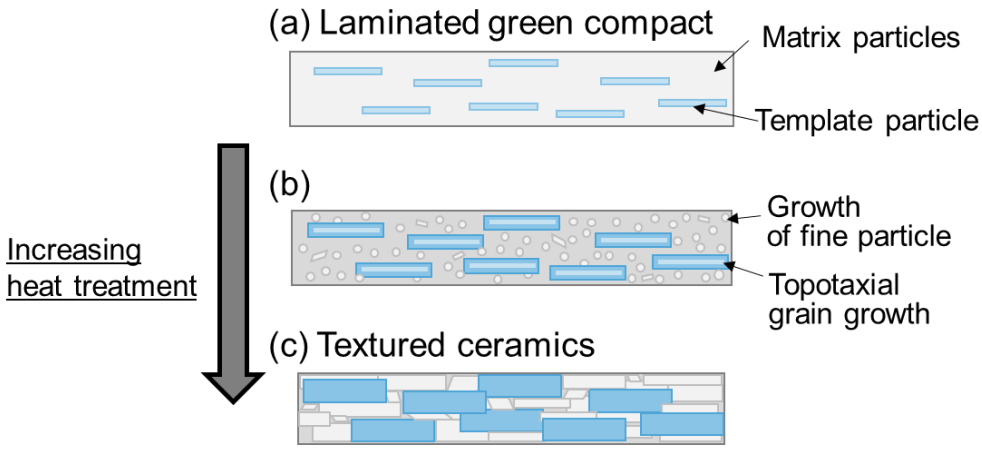

FIGURE 1.5 Schematic diagrams of a grain growth for TGG.

method is that a mixture of equiaxed fine particles and anisometric template particles is used as a starting material. The matrix fine particles between oriented template particles are taken into the template particles and used for their growth. In addition, the grains grow topotaxially along the template grains. In many cases, the addition of the fine particles to anisotropic template particles can prevent the formation of large pores and increase the density of the sintered body. The problem with TGG method is that the appropriate template particles are required. For example, it may often be difficult to synthesize templates for simple perovskite-type compounds with low crystal symmetry or compounds with complex compositions.

For those materials, the reactive template grain growth (RTGG) was proposed by Tani [24]. In the RTGG method, anisotropic particles with crystalline anisotropy are used as the template particles which are used as a precursor of the target compound, and fine particles that are complementary compounds of the target compound are also used [25]-[27]. The textured ceramics of the target compound were made by in situ reaction and subsequent sintering.

1.2.2 Electric Field Alignment Method

The method using an external electric field has been applied to control the alignment of liquid crystal molecules, which can be found in a liquid crystal display [28]. Thereafter, the use of this technique was expanded to align the inorganic fillers dispersed in a polymer matrix. In thermal conductive films containing various materials (e.g., carbon nanotube (CNTs) [29,30], carbon black (CB) [31,32], carbon fiber (CF) [33] and boron nitride (BN) [5,34]) fabricated under DC or AC electric field, the fillers aligned along the electric field and a linear assembly were observed.

Figure 1.6 shows the orientation method applied by an electric field as a driving force. This method employs the interaction between a polarization of materials and an electric field. Each conductive particle experiences the polarization in the electrical field [30]. A torque T induced by the polarization of the particles is expressed by the following equation: [5,34]

$$T = \frac{V}{2}\varepsilon_0 \left\{\frac{(\varepsilon_1-\varepsilon_2)^2}{\varepsilon_1}\right\} \times E^2 \cdot \sin 2\theta \qquad (1.1)$$

where V is the volume of the single particle, ε_0 is the dielectric constants in a vacuum, ε_1 and ε_2 are the relative permittivity of the particle and the solvent, and θ is the angle between the direction of the electric field and an axis of the particle, respectively. According to Eq. (1.1), the magnitude of the field induced torque T depends on the

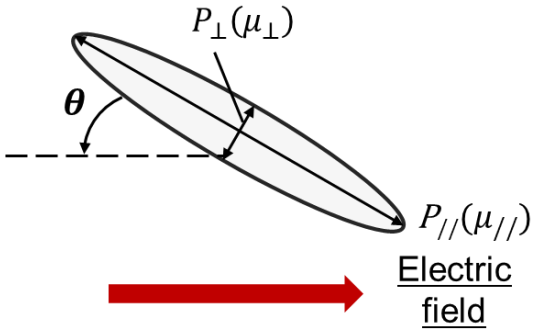

FIGURE 1.6 Schematic illustration of a polarized particle under an electric field.

anisotropy of the permittivity between the particle and the solvent. This means that the kinds of materials and solvents used for this technique are limited.

Recently, the equipment for the generation of nanosecond pulsed electric field was introduced [35] and the high producing power was utilized for the fabrication of linear assemblies of BN, CB and TiO_2 nanotubes (TNTs) in polysiloxane [36]-[38]. For these materials, the linear assembles formed along the electric field. Further, the results showed that the method applied pulsed electric field was more efficient than that used DC or AC electric field for forming the linear assembles. The TNTs composites prepared under the nanosecond pulsed electric field, for example, contributed to the higher optical transmittance under the light in the UV visible range and the lower reflectance compared with these prepared under DC electric field [37].

1.2.3 Magnetic Field Alignment Method

The control of structure and function by using a magnetic field have received attention since the 1950s [39]. The orientation technique by using the magnetic field was first applied to ferromagnetic material such as $BaO{\cdot}6Fe_2O_3$ [39]. Furthermore, the alignment of carbon fibers and the formation of crystal-oriented carbonaceous mesophase spherules were also performed under a magnetic field [40]-[42]. For example, when QS pitch coke was rotated and heat-treated in the magnetic field, large carbonaceous mesophase spherules with the same texture as a single sphere was generated due to a growth by a coalescence of *c*-axis aligned carbonaceous mesophase spherules [42].

After that, a cryogen-free superconducting magnet was developed by Japanese companies in the 1990s due to the discovery of superconducting material such as niobium system alloy and oxide high temperature superconductor materials [43]-[50]. This superconducting magnet made it relatively easy to use the high magnetic fields (10 T or more). The high magnetic field induced by the superconducting magnet can visualize the

magnetic effects on paramagnetic and diamagnetic materials including inorganic [6], [51]-[54], organic and polymeric fibers [6],[55,56]. An outstanding example is the crystal-oriented oxide high temperature superconductor materials fabricated in the high magnetic field [57]. The critical superconducting fields and critical currents of these materials were considerably improved by the particle-orientation because this kind of materials has a large crystal anisotropy. Ferrell et al. confined particle orientation of $YBa_2Cu_3O_{7-\delta}$ (Y123) powder in epoxy resin in a magnetic field of 9.4 T at room temperature [57]. This experiment clarified that the *c*-axis of Y123 particles was oriented parallel to the magnetic field. Ferreira et al. extended this work to examine the particle-orientation of epoxy-embedded powders of $RBa_2Cu_3O_{7-\delta}$ (*R*123), where *R* = rare-earth [58]-[60].

Figure 1.7 shows the particle orientation method applied the magnetic field as a driving force. This method employs the interaction between a feeble magnetic susceptibility material and a high magnetic field. The advantage is independence from

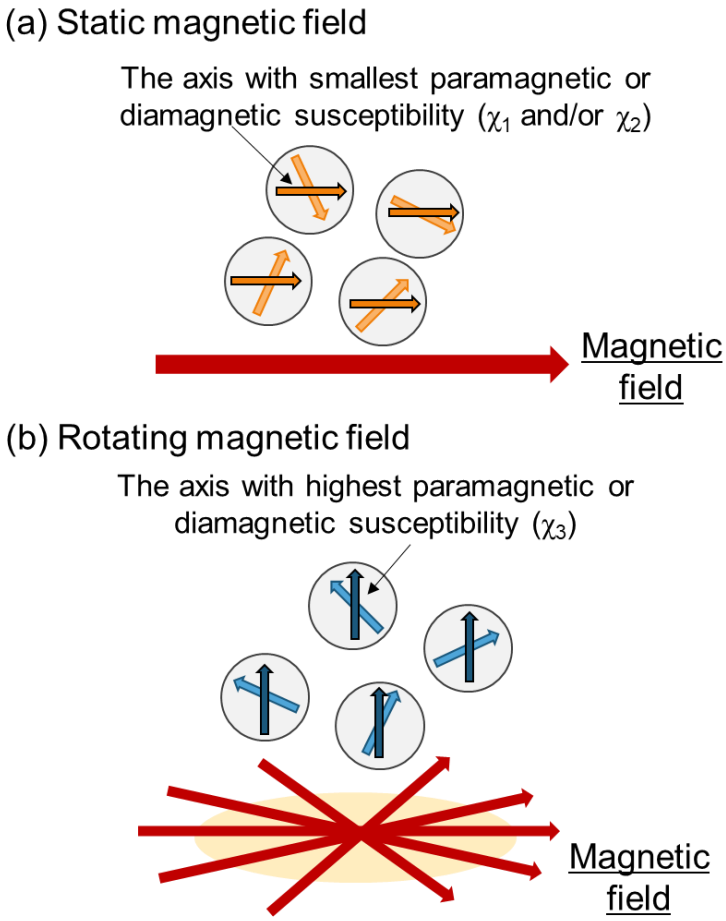

FIGURE 1.7 Responsibility of crystal particles ($\chi_3 < \chi_2 \leq \chi_1 < 0$) in (a) a static or (b) a rotating magnetic field.

particle shape because of contactless forming processing of oriented structure. This means that conventional raw powders can be used. Here, the difference of the magnetic energy, ΔE, resulting from rotation of particles in the magnetic field is expressed by the following equation [6,53],

$$\Delta E = \frac{\Delta\chi V B^2}{2\mu_0} \qquad (1.2)$$

where $\Delta\chi$ is the anisotropy of the diamagnetic susceptibility, V is the volume of each particle, B is the magnetic flux density, and μ_0 is the permeability in a vacuum. The direction of particle orientation can be controllable by the relationship between the anisotropy of the diamagnetic susceptibility and the direction of the applied magnetic field. This means that the orientation of the crystal particles using the magnetic field can selectively align to the direction showing high performance [41,42],[53]-[56].

A high magnetic field has also been used as the new fabrication processing of crystal-oriented ceramics [51]-[54],[57]-[96]. Table 1.2 shows examples of crystal-oriented ceramics prepared by colloidal processing in the magnetic field. So far, several kinds of functional ceramics have been fabricated by colloidal processing under the high magnetic field and subsequent sintering. This fabrication process was first applied to α-alumina by Uematsu et al. [61]. The *c*-axis of alumina particles aligned along the parallel direction to the magnetic field [61]-[63]. This result indicated that the diamagnetic susceptibility of the *c*-axis (χ_c) is smaller than that of a-axis (χ_a). This result agreed well with the anisotropic of diamagnetic susceptibility measured by a SQUID, reported by Uyeda et al. [97,98] A useful method for evaluating the orientation degree of *c*-axis oriented alumina green bodies, which is polarized light micrograph technique, was developed by Makiya et al. [64]. This alignment technique was extended to various functional ceramics such as ZnO, hydroxyapatite (HAp), TiO_2, Si_3N_4, AIN, SiC, piezoelectric ceramics and so on [65]-[93]. The crystal axis direction showing the diamagnetic susceptibility for each material was understood from these experimental results. In addition, Table 1.3 shows examples of crystal-oriented oxide high temperature superconductor materials prepared by using the magnetic field at room temperature [51,52],[57]-[60],[94]-[96]. Horii et al. reported that the tri-axes particle orientation for various oxide high temperature superconductor materials by using time-dependent magnetic fields for [51,52], [94]-[96]. The crystalline electric field strongly influenced the anisotropy of paramagnetic susceptibility, which corresponds to the character of each rare-earth. This means that a key parameter was the sign of the second-order Stevens factor, α_j, of rare-earth.

Recently, two state-of-the-art technologies have been proposed. One is to utilize special sintering techniques such as hot isostatic pressing (HIP) [82], [99,100] and spark

TABLE 1.2 Crystal structure and the axis with smallest diamagnetic susceptibility of functional ceramics.

Material	Crystal structure	Axis with smallest diamagnetic susceptibility	Reference
α-Al2O3	Hexagonal (corundum)	c-axis	[61]-[64]
ZnO	Hexagonal (wurtzite)	a,b-axes	[65]-[68]
Hydroxyapataite (HAp) Fluorapatite (FAp)	Hexagonal	a,b-axes	[69]-[71]
TiO2	Tetragonal (rutile, anatase)	c-axis	[72,73]
α-Si_3N_4, β-Si_3N_4	Hexagonal	a,b-axes	[74,75]
AIN	Hexagonal	a,b-axes	[76,77]
SiC	Hexagonal	c-axis	[78,79]
$Bi_4Ti_3O_{12}$ $MBi_4Ti_4O_{15}$ (M=Ca,Sr,Ba)	Layered perovskite	a,b-axes	[80]-[84]
$Sr_2NaNb_5O_{15}$(SNN) $KSr_2Nb_5O_{15}$(KSN) $Sr_{0.6}Ba_{0.4}Nb_2O_6$ (SBN60) $(Sr,Ca)_2NaNb_5O_{15}$(SCNN)	Tetragonal (tungsten bronze)	a,b-axes	[85]-[93]

TABLE 1.3 Second-order Stevens factor (a_j) and the axis with smallest paramagnetic susceptibility for oxide high temperature superconductor materials.
R$Ba_2Cu_3O_{7-\delta}$(*R*123), *R*$Ba_2Cu_4O_8$ (*R*124), $R_2Ba_4Cu_7O_{15-\delta}$ (*R*247) and *R*-doped $Bi_2Sr_2CaCu_2O$ (*R*-doped Bi2212), *R* = Rare earth.

	R-free	Y	La	Ce	Pr	Nd	Pm	Sm	Eu	Gd	Tb	Dy	Ho	Er	Tm	Yb	Lu	References
αj		0	0	-	-	-	+	+	0	0	-	-	-	+	+	+	0	
*R*123		c	c		c	c		c	ab	weak ab		c	c	ab	ab	ab		[51,52],[57]-[60]
*R*124		c						c	ab	ab		c	c	ab	ab	ab		[52,94]
*R*247		c							ab			c	c	ab				[52,95]
R-doped Bi2212	c	c	c		c	c		c	ab	c		c	c	ab	ab	weak ab	c	[51,96]

TABLE 1.4 Major alignment techniques for ceramic materials and comparison of these productivity, flexibility of materials, selectivity of orient direction and production cost.

Technique	Productivity	Materials versatility	Orient direction selectivity	Production cost	Microstructure control
Hot-working	○	○	×	△	△
Doctor blade	○	○	×	◎	○
Electric field	△	△	△	○	○
Magnetic field	△	◎	◎	△	△

plasma sintering (SPS) [101,102] after the fabrication of crystal oriented green compacts in the magnetic field. They were applied to simultaneously achieve both the high density and orientation. The high transparency was achieved by the decrease in both the small residual pores and the grain orientation. Another is the orientation control under the low magnetic field (> 2 T) for ceramic materials [103]-[106]. the enhancement of the anisotropy of the diamagnetic susceptibility, $\Delta\chi$, using the rare-earth or the multilayered graphene was reported [107,108].

For the alignment techniques for ceramic materials, the comparison of productivity, materials versatility, orient direction selectivity, production cost and microstructure control were summarized in Table 1.4. As seen in Table 1.4, the advantages of the magnetic alignment technique, which focused on this thesis, are to be able to use various material with the magnetic susceptibility and to choose freely the oriented crystal axis of the particles. However, in comparison with other techniques, the drawbacks are productivity, production cost and difficulty of a microstructure control; these drawbacks should be improved in order to apply this method for large-scale manufacturing.

Problems focused on this thesis shows below: (1) long forming time in the magnetic field and (2) difficulties for the control of the particle orientation under the magnetic field and of the microstructure after sintering. On the first issue, forming times in the magnetic field should be shortened because continuous processing is preferable for mass production. The second issue is also important to fabricate the oriented ceramics under the optimized condition for industrial applications. In the process chain, the crystal-oriented structure is constructed by the particle orientation in the magnetic field and following sintering. This means that it is necessary to understand both the particle rotation behavior in the rotating magnetic field and mechanism of the oriented structure development during sintering.

1.3 FABRICATION METHOD USING MAGNETIC FIELD AND SUBSEQUENT SINTERING

The fabrication process using the magnetic field for the crystal-oriented ceramics is illustrated in Fig. 1.8. To fabricate the oriented structure for the functional ceramics, colloidal processing under the magnetic field and subsequent sintering processing have been examined [53,54].

1.3.1 Colloidal Processing in High Magnetic Field

The particle-orientated green compacts of several functional ceramics were prepared by colloidal processing under the magnetic field. A green body or sheet with oriented particles has been typically fabricated by conventional processing (e.g., evaporation of solvents, slip casting or tape casting). Figure 1.9 shows schematic illustrations of the slip casting, which is the most widely used method for the forming process in the magnetic

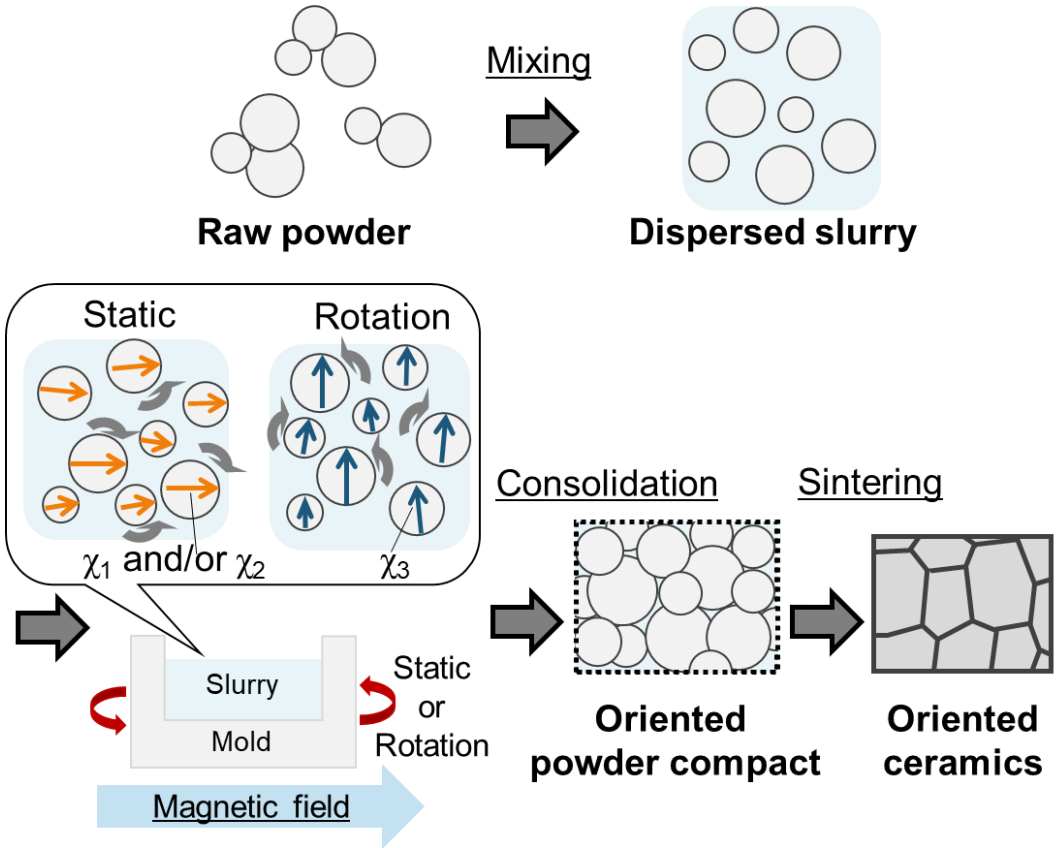

FIGURE 1.8 Schematic of fabrication processing using colloidal processing under the magnetic field and subsequent sintering processing. The diamagnetic susceptibility of particles is $\chi_3 < \chi_2 \leq \chi_1 < 0$.

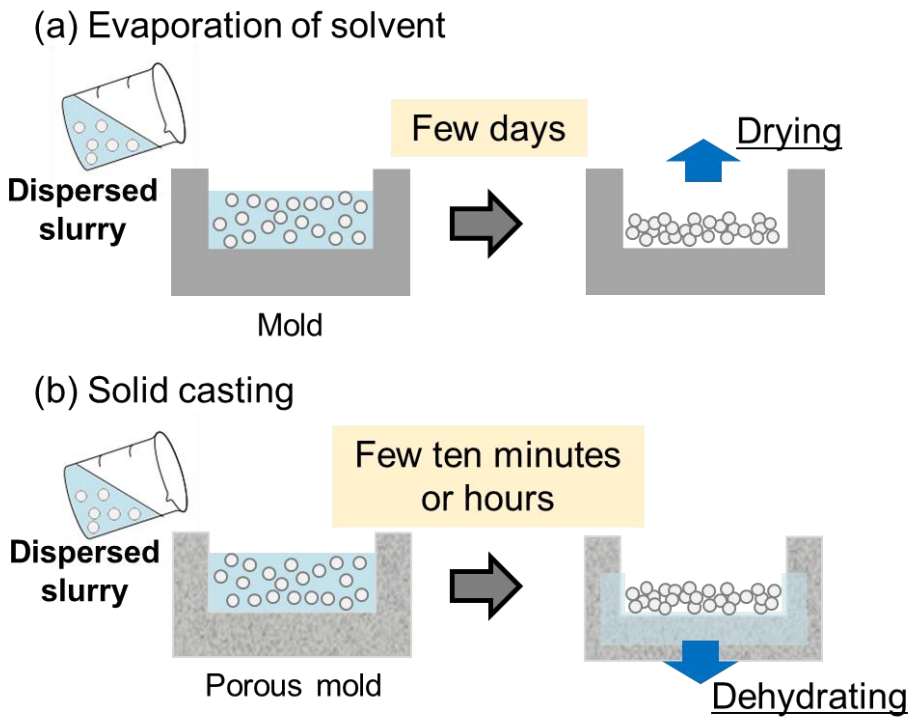

FIGURE 1.9 Schematic illustrating the slip casting. (a) Evaporation of solvent, (b) solid casting.

field [2, 109]. The most significant advantage is its versatility in terms of shape, size, and materials applicability [110]. However, a drawback is that the length of time required for shaping the material is high because such a technique requires long consolidation or drying times. Although the time needed for the particle orientation in the magnetic field is less than a few seconds, the sample must remain within the magnetic field until a period from several tens of minutes to hours. Furthermore, long consolidation time expects to form an aggregation of the particles in the slurry and disturb the orientation of particles because agglomerated particles in a slurry are stable.

Gel-casting is used to shorten the consolidation time in the magnetic field [111]-[115]. Gel-casting was first developed at Oak Ridge National Laboratory (ORNL) [116]. It is a forming method for fabricating the homogeneous structure of the various materials, a near-net-shape shaping method [2, 117]. A schematic of the process is shown in Fig. 1.10 [110]. The ceramics powder is mixed with a liquid and a gelling agent to prepare a fluid slurry. Gelling is caused before the powder in the slurry has time to settle. As a result, the consolidated green body is quite uniform. *C*-axis oriented Al-doped ZnO ceramics were fabricated by using the gel-casting in the rotating high magnetic field and showed a higher electrical conductivity than the randomly oriented specimens [111,112]. The

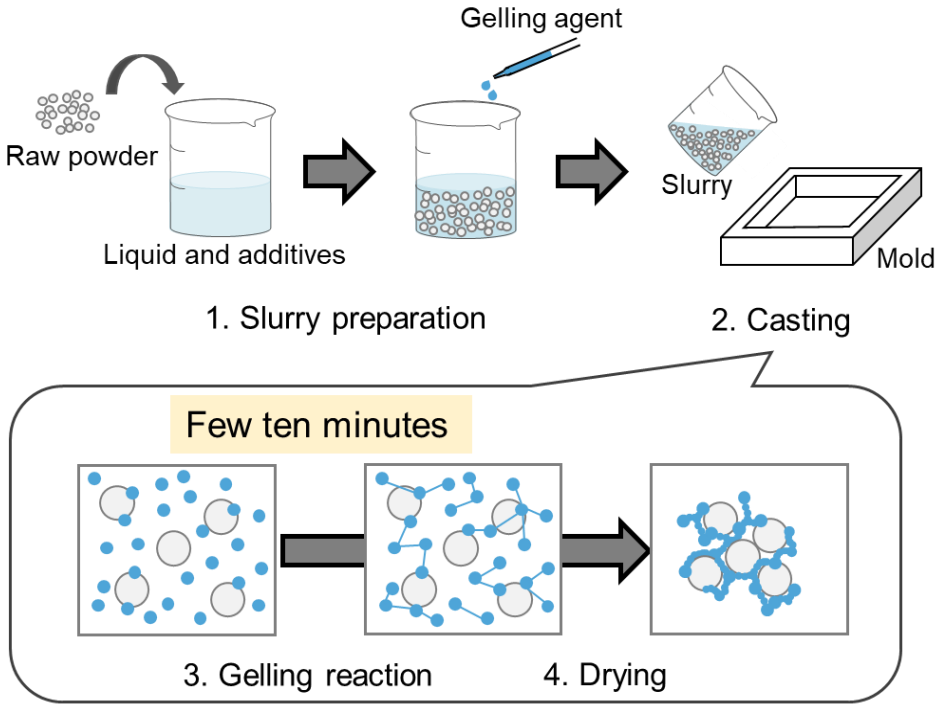

FIGURE 1.10 Schematic illustrating the gel-casting process.

improvement of the degree of particle orientation by a high magnetic field and the reduction in consolidation time were attained *via* gel-casting. In this forming process, however, a drawback is that it is difficult to control the gelation rate and to remove the liquid. Therefore, the utilization of novel colloidal processing is required to even more shorten and control the consolidation time in the high magnetic field.

1.3.2 Theory of Particle Orientation in Magnetic Field

It is necessary to thoroughly understand the behavior of particle orientation in the magnetic field for further development and industrial applications of the magnetic alignment method. Kimura et al. proposed a theoretical description of the behavior of polymer fibers in a static and rotating magnetic field [56], [118,119]. Figure 1.11 shows a schematic diagram of a single spherical particle in a statistic or a rotating magnetic field. The energy of magnetization $\boldsymbol{U}$ of the magnetic field applied to the particle depends on the angle between the crystal axis and the magnetic field. It is calculated from the following expression: [56],[118]

$$\boldsymbol{U} = -\frac{1}{2\mu_0} V\chi_{//}\boldsymbol{B}^2 - \frac{1}{2\mu_0} V\Delta\chi(\boldsymbol{n}\cdot\boldsymbol{B})^2 \qquad (1.3)$$

where $\chi_{//}$ is the largest diamagnetic susceptibility $(\chi_{//} < \chi_{\perp} < 0)$, $\Delta\chi = |\chi_{\perp} - \chi_{//}|$ is

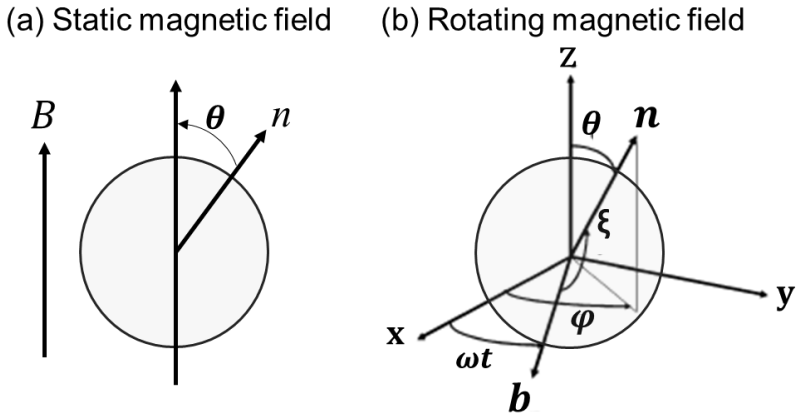

FIGURE 1.11 Schematic view of a spherical particle in (a) a static magnetic field or (b) a rotating magnetic field.

the anisotropic of the diamagnetic susceptibility $\boldsymbol{n}$ is a unit vector parallel to $\chi_{//}$, $\boldsymbol{B}$ is a unit vector for a magnetic field acting on a particle rotating on the x-y plane. Here, θ is the angle between the magnetization vector of a particle and the z-axis, φ is the angle between the projection of the magnetization vector on the x-y plane and the x-axis, and ξ is the angle between $\boldsymbol{n}$ and $\boldsymbol{B}$. The particle should be aligned in the direction of the z-axis as $\boldsymbol{n}$ is influenced by the magnetic field.

A particle subjected to magnetic torque $\boldsymbol{M}$ in a magnetic field can be described by Eq. (1.4) [119].

$$\boldsymbol{M} = \frac{V\Delta\chi}{\mu_0}(\boldsymbol{n}\cdot\boldsymbol{B})(\boldsymbol{n}\times\boldsymbol{B}) = \frac{V\Delta\chi}{\mu_0}B^2\cos\xi\sin\xi\,\boldsymbol{e} \qquad (1.4)$$

where $\boldsymbol{e}$ is a unit vector parallel to $\boldsymbol{n}\times\boldsymbol{B}$. The hydrodynamic torque $\boldsymbol{N}$ is caused by the interaction between a particle and the surrounding liquid acting on the particle, where it is rotating at an angular velocity $\boldsymbol{\Omega}$. Therefore, this torque can be related to the viscosity of the surrounding liquid η and the angular velocity of a particle $\boldsymbol{\Omega}$:[119]

$$\boldsymbol{N} = -\eta\boldsymbol{L}\boldsymbol{\Omega} \qquad (1.5)$$

where $\boldsymbol{L}$ is a tensor that is dependent on the particle shape. For a spherical particle of radius r, $\boldsymbol{L}$ is diagonal, and its components are equivalent to L. The equation describing particle rotation in a liquid in a rotating magnetic field is written as a balance of the magnetic torque and the hydrodynamic torque under a stable state:[119]

$$\boldsymbol{\Omega} = \frac{1}{6\mu_0\eta}\Delta\chi(\boldsymbol{n}\cdot\boldsymbol{B})(\boldsymbol{n}\times\boldsymbol{B}) \qquad (1.6)$$

where $V/L=(4\pi/3)r^3/8\pi r^3 = 1/6$. Using the relation $d\boldsymbol{n}/dt = \boldsymbol{\Omega}\times\boldsymbol{n}$, we deduce

$$\frac{d\boldsymbol{n}}{dt} = 2\tau^{-1}(\boldsymbol{n}\cdot\boldsymbol{b})[\boldsymbol{b} - \boldsymbol{n}(\boldsymbol{n}\cdot\boldsymbol{b})] \qquad (1.7)$$

where $\boldsymbol{b} = \boldsymbol{B}/\mathrm{B}$ and the intrinsic magnetic response rate of a particle, τ^{-1}, exposed to the rotating field is defined as:[56],[118]-[122]

$$\tau^{-1} = \frac{1}{12\mu_0\eta}\Delta\chi B^2 \qquad (1.8)$$

Here, in the static magnetic field, the solution for this equation is given by: [118]

$$\frac{d\theta}{dt} = 2\tau^{-1}\sin 2\theta \qquad (1.9)$$

Thus, the orientation time *t* is obtained as:

$$t = -2\tau \ln\frac{\tan\theta}{\tan\theta_0} \qquad (1.10)$$

On the other hand, in the rotating magnetic field, $\boldsymbol{b}$ is expressed as $(\cos\omega t\,, \sin\omega t\,, 0)$, where ω is the rotational angular velocity of the magnetic field and $\boldsymbol{n}$ is indicated as $(\sin\theta\cos\varphi\,, \sin\theta\sin\varphi\,, \cos\theta)$. [56],[119]-[121]

$$\frac{d\theta}{dt} = \tau^{-1}\sin 2\theta\, cos^2(\varphi - \omega t) \qquad (1.11)$$

$$\frac{d\varphi}{dt} = -\tau^{-1}\sin 2(\varphi - \omega t) \qquad (1.12)$$

According to Eqs. (1.11) and (1.12), the particle rotates synchronously with the applied magnetic field rotation as $\mathrm{d}\varphi/\mathrm{d}t = \omega$ in the case of stable state conditions, where δ is defined as $\delta = \varphi - \omega t$ [56],[119, 120]. From Eq. (1.12), $\sin 2\delta = -\tau\omega$ is obtained by using the relation $d\delta/dt = 0$. Accordingly, this stationary state is possible only if $|\tau\omega| \leq 1$, which describes the conditions for particle alignment under a static magnetic field. However, when the value of $|\tau\omega|$ is > 1, such as when the magnetic field has a rapid angular velocity, the particle cannot follow the rotation of the magnetic field. Because it is assumed that $\varphi = 0$, Eqs. (1.11) and (1.12) can be written as follows:

$$\frac{d\theta}{dt} = \tau^{-1}\sin 2\theta\, cos^2(-\omega t) \qquad (1.13)$$

$$\frac{d\varphi}{dt} = 0 \qquad (1.14)$$

Therefore, the following equation can be deduced:[56],[118]-[120]

$$\ln\frac{\tan\theta}{\tan\theta_0} = -\frac{t}{\tau} - \frac{1}{2\omega\tau}\sin(-2\omega t) \qquad (1.15)$$

When the second term on the right hand side is very small compared with the first term, that is $\left|-\frac{1}{2\omega\tau}\sin(-2\omega t)\right| < 1$, the orientation time *t* is obtained as: [56],[119, 120]

$$t = -\tau \ln \frac{\tan \theta}{\tan \theta_0} \qquad (1.16)$$

According to Eqs. (1.10) and (1.16), the *t* in the rotating magnetic field is twice as long as that in the static magnetic field.

In previous studies, Kimura et al. investigated the dependence of the magnetic flux density *B* and the filer lengths on the intrinsic magnetic response rate of a fiber τ^{-1} in the dilute suspension in a magnetic field of 1.2 T by direct observations [118,119]. As shown in Fig. 1.12, for the fiber rotation in the static and rotating magnetic field, they reported that the intrinsic magnetic response rate of a fiber τ^{-1} is proportional to B^2 and increased with decreasing the fiber lengths. Hirota et al. extended this work to examine an orientation behavior of carbon fibers and needle-like titania fibers in a high magnetic field up to 10 T by using *in site* microscopic observations [123]. Although they investigated the influence of the viscosity of the solvent on the magnetic orientation behavior of the rod-like particles in the high magnetic field, a significant influence was not obtained.

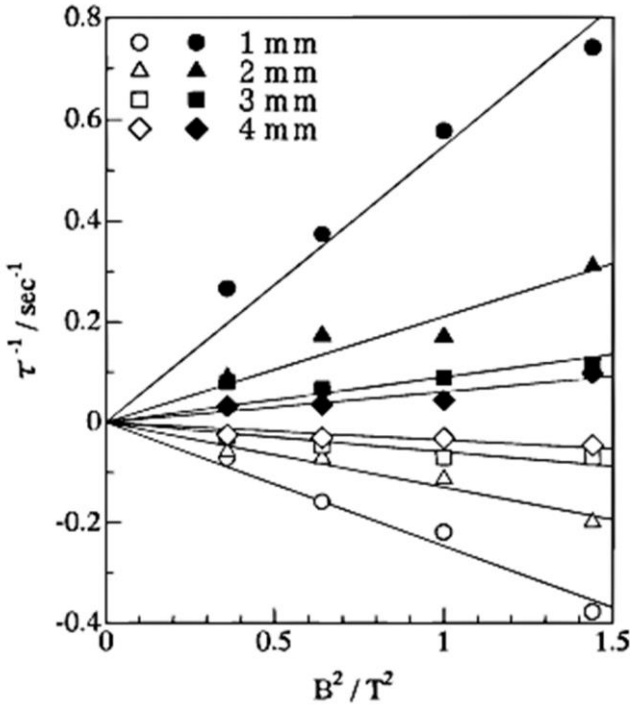

FIGURE 1.12 Relation between τ^{-1} and the square of the magnetic flux density B^2 measured for the polyethylene fiber (open symbols) and carbon fiber (filled symbols) with different fiber lengths [118].

1.3.3 Development of Crystal-Orientated Structure during Sintering

To produce highly oriented ceramics with a well-densified structure, it is necessary to understand the development mechanism of the oriented structures in the compact during sintering. In practical processing, the oriented structures in the green body or sheet are enhanced by grain growth during sintering. Also, the densification and the grain growth proceed anisotropically in crystal-oriented ceramics. Anisotropic sintering of functional ceramics shows more complex phenomena.

In the TGG and RTGG, the sintering processing results in the densification and grain growth in order to yield highly textured ceramics. Messing et al. and Suvaci et al. reported an experimental investigation of the texture development during sintering for the oriented alumina and zinc oxide ceramics prepared by TGG [124]-[126]. They reported the effects of the amount, size, and distribution of the template particles on the development of the oriented structure [124, 125]. There are also some works investigated on the textured piezoelectric ceramics fabricated by RTGG. The microstructure development of materials with the tungsten bronze structure such as $Sr_{0.53}Ba_{0.47}Nb_2O_6$, $KSr_2Nb_5O_{15}$, and $Sr_{1.85}Ca_{0.15}NaNb_5O_{15}$ were investigated [127]-[129]. After the densification and/or the phase formation, the template grains are grown by incorporating the matrix grains, leading to the development of the textured structure.

In the technique of particle orientation using the magnetic field, the only conventional fine particles are used. It means that it is desirable for easy densification of bulk samples. However, it is not simple to estimate and to control the final microstructure as shown in Fig. 1.13. For example, if the c-axis of spherical particles is oriented in an alumina system, it showed significant shrinkage along to the *c*-axis direction during sintering [130]. The

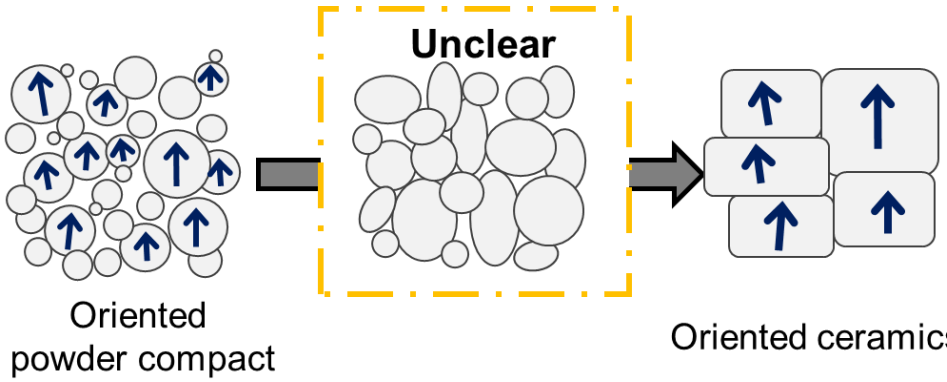

FIGURE 1.13 Schematic illustrations of formation mechanism for crystal-oriented ceramics.

textured microstructure was developed by grain growth along the a-axis direction after densification [65]. In addition, some previous studies were focused on *c*-axis oriented zinc oxide and *c*-axis-oriented $Sr_{0.6}Ba_{0.4}Nb_2O_6$ (SBN60) [71, 131]. *C*-axis oriented zinc oxide green compacts consisting of platelet shape particles isotropically shrank at the initial stage of sintering, and the degree of shrinkage along to the *a*-axis direction became large during the middle stage of sintering. And, the grain growth along the *a*-axis was observed. Whereas for *c*-axis oriented SBN60 powder compacts of slight anisotropic shape particles, it showed extensive shrinkage along the longitudinal direction of the particles in spite of the small amount of necking among particles.

1.4 NOVEL FORMING PROCESSING USING PHOTOPOLYMERIZATION REACTION

The photopolymerization reaction using a tape casting, which is reported by Chartier et al. [132, 133], is focused on in this thesis in order to shorten the forming time in the magnetic field. An illustration of the process with the photopolymerization reaction is shown in Fig. 1.14. The ceramics powder is mixed with a UV curable monomer and photoinitiator to prepare a UV curable slurry. The slurry is exposed to UV rays. Once polymerized, the photopolymerizable solvent constitutes a though matrix around ceramic particles and obtains the bond to the green sheets. This organic phase removes by proper thermal treatment before sintering. The advantages of photopolymerization reactions are fast and controllable, and the processing time to consolidate ceramics particles is a few seconds, which is extremely short compared with conventional processing techniques. The homogeneous powder packing structure in a polymerized compact is obtained due to the forming method without the shrinkage by the evaporation of the solvent.

A critical parameter with a UV curing system containing ceramic powders is the rapid attenuation of the incident light. In photocurable ceramic slurry, a penetration of UV rays is prevented due to both the absorption and the scattering by particles, and then, the addition of particles in the UV curing system largely limits the thickness of the cured slurry. Although a high powder loading is desirable to circumvent deformations and cracks during binder removal and to obtain homogeneous and dense ceramics after sintering, the cured depth of the slurry decreases with increasing the concentration of the particles in the slurry [133]-[136].

The presence of particles absorbing radiation in the wavelength of UV rays influences not only the attenuation of the UV rays also the reduction of the absorption by photoinitiator [134,135]. The decrease in the absorption by photoinitiator restricts to

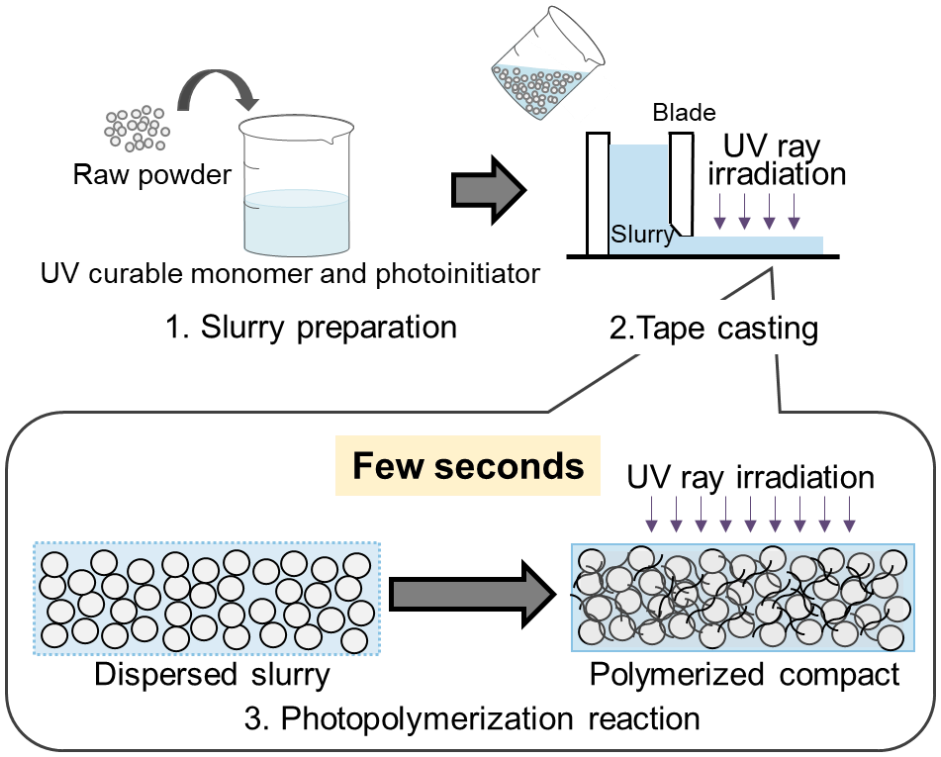

FIGURE 1.14 Schematic diagrams of novel colloidal processing involving photo polymerization reaction.

cause the polymerization reaction. The photoinitiator of a much higher extinction coefficient *e* than that of the powders has to be used to favor the absorption by the photoinitiator. Furthermore, the concentration of the photoinitiator should be optimized [135]. UV radiation absorbed by the photoinitiator increased with the initiator concentration. However, for the high photoinitiator concentration, the high absorption in the upper layer of the sheet causes a decrease in the amount of radiation reaching the bottom layer of the sheet. As a consequence, the thickness of the cured layer is limited. Thus, there is the optimal concentration of the photoinitiator. Furthermore, the degree of scattering of the UV rays depends on the refractive index difference between the solvent and the ceramic powders as well as the concentration of the particles [136].

1.5 OBJECTIVES

The objectives of the present thesis were to fabricate crystal-oriented ceramics using a photopolymerization reaction under the high magnetic field and subsequent sintering. Besides, it is to clarify critical paratemers in the fabrication process using magnetic field for crystal-oriented ceramics. Particurally, the particle orientation behavior in a rotating magnetic field and the development of the oriented microstructure during sintering were

elucidated experimentally.

Two materials were selected in this study. One is (Sr, Ca)$_2$NaNb$_5$O$_{15}$ (hereafter referred to as SCNN), which are ferroelectrics materials of tungsten bronze type. There are multi-functional materials that show great potential as lead-free piezoelectric and optical materials [137]. SCNN requires *c*-axis oriented structure because high piezoelectric performance is achieved only for *c*-axis [129], [137, 138]. Previous studies reported that the *c*-axis oriented SCNN ceramics fabricated by the colloidal processing in the rotating magnetic field and sintering [94, 95]. In previous studies, the piezoelectric property is considerably improved, and the high powder property is better than that of the Pb systems by crystal orientation [95,139].

Another is hydroxyapatite ($Ca_{10}(PO_4)_6(OH)_2$; HAp) material. HAp has excellent compatibility with the human body and has been used for implant materials such as bones and teeth [140, 141]. HAp typically takes on a hexagonal crystal structure, which has two principal crystal planes, *a*,*b*-plane and *c*-plane. Each crystal plane functions differently as an absorbent for bio-related substances such as proteins and amino acids, in ion-exchange, and in providing mechanical properties [142]. For example, in a living bone, the *c*-axis of HAp crystallites are oriented parallel to the direction of the maximum load on bones in order to improve mechanical strength in the load direction [143]. As a result, *a*,*b*-planes are exposed to the bone surface. In contrast, the surface of dental enamel presents *c*-planes to protect teeth from dissolving, as the *c*-plane is inactive to acid and body fluids [144]. Therefore, when using HAp as an implant material, the correct crystal orientation must be adopted to perform the target function(s) optimally; this approach can also be expected to improve affinity to the human body. The *c*-axis oriented HAp ceramics fabricated by the colloidal processing in the rotating magnetic field and sintering was reported [73].

1.6 OUTLINE OF THIS THESIS

This thesis consists of seven chapters. The flow of this thesis is illustrated in Figure 1.15.

Chapter 1 described historically conventional techniques for crystal-oriented ceramics. The characteristic and a problem for the solution of the colloidal processing under the high magnetic field, which was focused on this thesis, were summarized. The photopolymerization reaction was proposed as novel colloidal processing in the magnetic field. Then, the objectives and the reason for this study were described

Chapter 2 focused on the novel colloidal processing using a photopolymerization reaction in the magnetic field. The *c*-axis oriented SCNN green sheets were fabricated with a short time. The preparation of dispersed SCNN slurry with UV curable resin and

the curable behavior of its slurry was investigated.

Chapter 3 described the rotation behavior of fine particles in the concentrated slurry under the magnetic field. The dependence of the slurry viscosity and magnetic flux density on the particle orientation was clarified experimentally. The viscosity of a slurry is varied by the concentration of powder in the slurry and the temperature of the slurry.

Chapter 4 focused on the unique anisotropic sintering for *c*-axis oriented SCNN ceramics. The grain growth with the development of oriented structure was investigated based on microstructure observation.

Chapter 5 extended the fabrication of *c*-axis oriented SCNN bulky ceramics by repeating photopolymerization reaction in the rotating magnetic field and following sintering. The improvement of piezoelectric characters by crystal orientation was mentioned

Chapter 6 described the multiplicity of the novel fabrication process proposed in Chapters 2 - 5. *C*-axis oriented HAp bulky ceramics were fabricated by once photopolymerization in the rotating magnetic field and subsequent sintering.

Chapter 7 is a summary of this thesis.

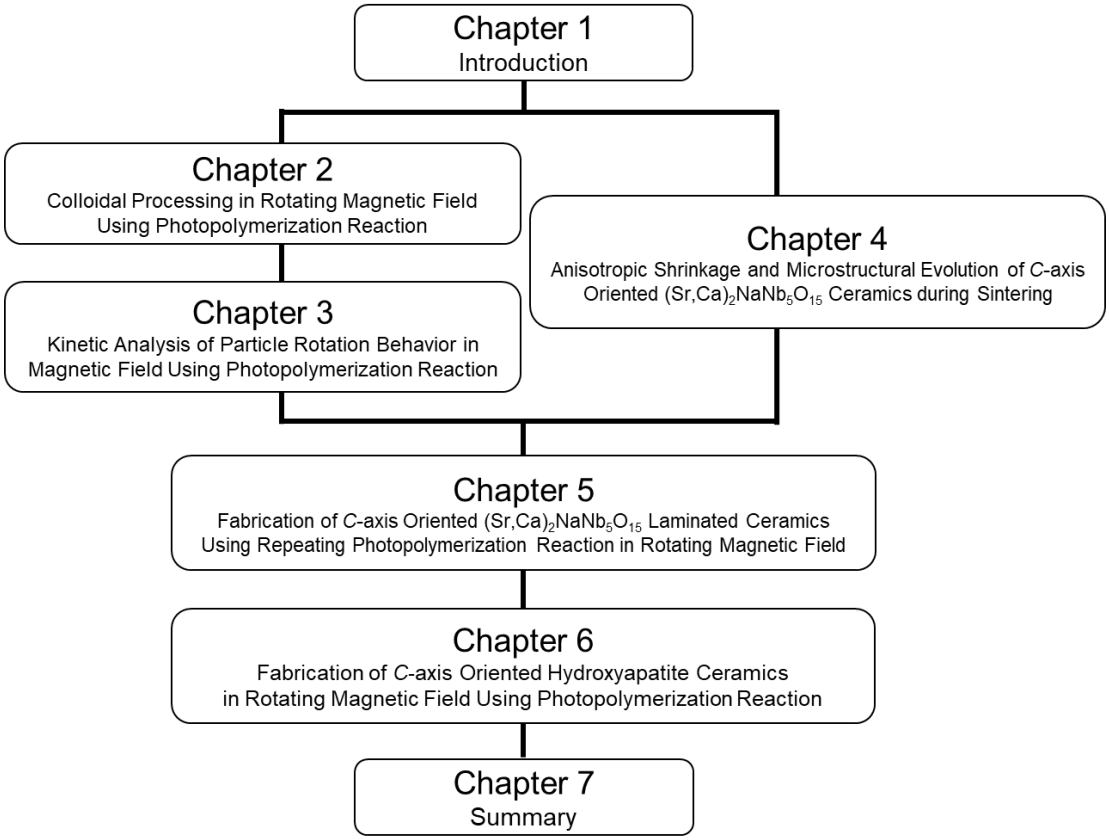

FIGURE 1.15 Flow chart of this thesis.

REFERENCES

[1] M. N. Rahaman, Ceramic processing and sintering, Marcel Dekker, Inc., (2003) pp1-5

[2] D. W. Richerrson, Modern ceramic engineering, Marcel Dekker, Inc., (1992) pp3-70, 461-478

[3] T. Takenaka, J. Ceram. Soc. Japan, 110[4], 215-224 (2002)

[4] G. L. Messing, S. Troller-McKinstry, E. M. Sabolsky, C. Duran, S. Kwon, B. Brahmaroutu, P. Park, H. Yilmaz, P. W. Rehrlg, K. B. Eitel, E. Sucaci, M. Seabaugh and K. S. Oh, Crit. Rev. Solid State Mater. Sci., 29 (2004) 45-96

[5] H. -B. Cho, T. Nakayama, T. Suzuki, S. Tanaka. W. Jiang, H. Suematsu and K. Niihara, Jpn. J. Appl. Phys., 50 (2011) 01BJ05

[6] K. Kitazawa, S. Ozeki, S. Tanimoto and M. Yamaguchi, 磁気科学, IPC (2002) [in Japanese]

[7] K. Okazaki and S. Narushima, J. Ceram. Soc. Japan, 76, 19-25 (1968) [in Japanese]

[8] A. H. Heuer, D. J. Sellers and W. H. Rhodes, J. Am. Ceram. Soc., 52[9] (1969) 468-473

[9] Y. Ma and K. J. Bowman, J. Am. Ceram. Soc., 74[11] (1991) 2941-2944

[10] C. Carry and A. Mocellin, Ceram. Int., 13[2] (1987) 89-98

[11] L. A. Brissette, P. L. Burnett, R. M. Spriggs and T. Vasilos, J. Am. Ceram. Soc., 49[3] (1966) 165-166

[12] T. Kimura, T. Yoshimoto, N. Iida, Y. Fujita, and T. Yamaguchi, J. Am. Ceram. Soc., 72[1] (1989) 85-89

[13] K. Nagata, Y. Yamamoto, H. Igarashi and K. Okazaki, Ferroelectrics, 38 (1981) 853-856

[14] S. Swartz, W. A. Schulze and J. V. Biggers, Ferroelectrics, 38 (1981) 765-768

[15] M. Granahan, M. Holmes, W. A. Schulze and R. E. Newnham, J. Am. Ceram. Soc., 64[4] (1981) C-68-C-69

[16] T. Kimura, M. H. Holmes and R. E. Newnham, J. Am. Ceram. Soc., 65[4] (1982) 223-226

[17] H. Watanabe, T. Kimura and T. Yamaguchi, J. Am. Ceram. Soc., 72[2] (1989) 289-293

[18] M. M. Seabaugh, I. H. Kerscht and G. L. Messing, J. Am. Ceram. Soc., 80[5] (1997) 1181-1188

[19] K. Hirao, M. Ohashi, M. E. Brito and S. Kanzaki, J. Am. Ceram. Soc., 78[6] (1995) 1687-90

[20] S. H. Hong and G. L. Messing, J. Am. Ceram. Soc., 82[4] (1999) 867-872

[21] E. Suvaci and İ. Ö. Özer, J. Eur. Ceram. Soc., 25 (2005) 1663-1673
[22] T. Kimura, J. Ceram. Soc. Japan, 114[1] (2006) 15-25
[23] T. Kimura, J. Ceram. Soc. Japan, 124[4] (2016) 268-282
[24] T. Tani, R & D Review of Toyota CRDL, 33[1] (1998.3)
[25] T. Takeuchi, T. Tani and Y. Saito, Jpn. J. Appl. Phys., 38 (1999) 5553-5556
[26] T. Tani, R & D Review of Toyota CRDL, 36[3] (2001.9) [in Japanese]
[27] T. Tani, J. Ceram. Soc. Japan, 114[5] (2006) 363-370
[28] H.Orihara, 液晶の物理, Published by UCHIDA ROKAKUHO PUBLISHING Co., LTD. (2004) [in Japanese]
[29] C. Park, J. Wilkinson, S. Banda, Z. Ounaies, K. E. Wise, G. Sauti, P. T. Lillehei and J. S. Harrison, J. Poly. Sci.: B: Poly. Phys., DOI 10.1002/polb.20823
[30] C. A. Martin, J. K. W. Sandler, A. H. Windle, M. -K. Schwarz, W. Bauhofer, K. Schulte and M. S. P. Shaffer, Polymer, 46 (2005) 877-886
[31] T. Prasse, L. Flandin, K. Schulte and W. Bauhofer, Appl. Phys. Lett., 72 (1998) 2903-2905
[32] M. -K. Schwarz, W. Bauhofer and K. Schulte, Polymer, 43 (2002) 3079-3082
[33] T. Takahashi, T. Murayama, A. Higuchi, H. Awano and K. Yonetake, Carbon, 44 (2006) 1180-1188
[34] H. -B. Cho, T. Nakayama, T. Suzuki, S. Tanaka, W. Jiang, H. Suematsu and K. Niihara, J. Nanomter., 2011 (2011) 693454
[35] T. Yokoo, T. Imafuku, N. Oshima, W. Jiang and K. Yasui, Papers of Technical Meeting on Pulsed Power Technology, IEE Japan ED, PPT-04-10 (2004) 11-14 [in Japanese]
[36] H. -B. Cho, M. Shoji, T. Fujiwara, T. Nakayama, H. Suematsu, T. Suzuki and K. Hiihara, J. Ceram. Soc. Jpn., 118[1] (2010) 66-69
[37] J. -W. Lee, H. -B. Cho, T. Nakayama, T. Suzuki H. Suematsu and K. Niiraha, J. Asian Ceram. Soc., 2[2] (2014) 97-101
[38] M. T. T. Huynh, H. -B. Cho, T. Suzuki, H. Suematsu, S. T. Nguyen, K. Niihara and T. Nakayama, Comps. Sci. Technol., 154 (2018) 165-174
[39] G. W. Rathenau, J. Smit and A. L. Stuyts, Zeitschrift für Physik, Bd. 133 (1952) 250-260
[40] V. Timbrell, J. Appl. Phys., 43[11] (1972) 4839-4840
[41] T. Imamura, H. Honda and H. Kakiyama, Carbon, 76 (1974) 17-19 [in Japanese]
[42] T. Imamura, H. Honda and H. Kakiyama, Carbon, 76 (1974) 20-22 [in Japanese]
[43] G. B. Yntema, Phys. Rev., 98 (1955) 1197
[44] J. E. Kunzler, Rev. Mod. Phys., 33 (1961) 501-509

[45] J. E. Kunzler, E. Buehler, F. S. L. Hsu and J. H. Wernick, Phys. Rev. Letters, 6[3] (1961) 89-91
[46] J. K. Hulm, J. E. Kunzler and B. T. Matthias, Physics Today, 34[1] (1981) 34-43
[47] J. E. Kunzler, IEEE Trans. Magn., 23[2] (1987) 396-401
[48] J. G. Bednorz and K. A. Müller, Z. Phys. B – Condensed matter, 64 (1986) 189-193
[49] T. R. Dinger, T. K. Worthington, W. J. Gallagher and R. L. Sandstrom, Phys. Rev. Letters, 58 (1987) 2687-2691
[50] H. Maeda, Y. Tanaka, M. Fukutomi and T. Asano, Jpn. J. Appl. Phys., 27[2] (1988) 209-210
[51] S. Horii, A. Ishihara, T. Fukushima, T. Uchikoshi, H. Ogino, T. S. Suzuki, Y. Sakka, J. Shimoyama and K. Kishio, Sci. Technol. Adv. Mater., 10 (2009) 014604
[52] S. Horii, M. Tamaki, J. Shimoyama and T. Doi, J. Cryo. Super. Soc. Jpn., 49[1] (2014) 3-10
[53] Y. Sakka and T. S. Suzuki, J. Ceram. Soc. Japan, 113[1] (2005) 26-36
[54] Y. Sakka, KONA powder and particle Journal, 36 (2019) 114-128
[55] T. Kimura, Polymer J., 35[11] (2003) 823-843
[56] T. Kimura, F. Kimura and M. Yoshino, Langmuir, 22 (2006) 3464-3466
[57] D. E. Ferrell, B. S. Chandrasekhar, M. R. DeGuire, M. M. Fang, V. G. Kogan, J. R. Clem and D. K. Finnemore, Phys. Rev. B, 36 (1987) 4025-4027
[58] J. M. Ferreira, M. B. Maple, H. Zhou, R. R. Hake, B. W. Lee, C. L. Seaman, M. V. Kuric and R. P. Guertin, Appl. Phys., A47 (1988) 105-110
[59] B. W. Lee, J. M. Ferreira, Y. Dalichaouch, M. S. Torikachvili, K. N. Yang and M. B. Maple, Phys. Rev. B, 37 (1988) 2368-2371
[60] J. M. Ferreira, B. W. Lee, Y. Dalichaouch, M. S. Torikachvili, K. N. Yang and M. B. Maple, Phys. Rev. B, 37 (1988) 1580-1586
[61] K. Uematsu, T. Ishikawa, D. Shouji, T. Kimura and K. Kitazawa, Japan Pat. No. 3556886, 特開 2002-053367 (2002)
[62] T. S. Suzuki, H. Ohtsuka, Y. Sakka, K. Hiraga and K. Kitazawa, J. Jpn. Soc. Powder Powder Metall., 47[9] (2000.9) 1010-1014 [in Japanese]
[63] T. S. Suzuki, Y. Sakka and K. Kitazawa, Adv. Eng. Mater., 3[7] (2001) 490-492
[64] A. Makiya, D. Shouji, S. Tanaka, N. Uchida, T. Kimura and K. Uematsu, Key Eng. Mater., 206-213 (2002) 445-448
[65] T. S. Suzuki and Y. Sakka, Chem. Lett. (Jpn.), 31 (2002) 1204-1205
[66] S. Tanaka, A. Makiya, Z. Kato, N. Uchida, T. Kimura and K. Uematsu, J. Mater. Res., 21[3], 703-707 (2006)
[67] S. Tanaka, A. Makiya, Z. Kato and K. Uematsu, J. Eur. Ceram. Soc., 29 (2009) 955-

959

[68] S. Tanaka, Y. Nagashima, R. Furushima and K. Uematsu, IOP Conf. Ser.: Mater. Sci. Eng., 21 (2011) 012008

[69] K. Inoue, K. Sassa, Y. Yokogawa, Y. Sakka, M. Okido and S. Asai, Mater. Trans., 44[6] (2003) 1133-1137

[70] J. Akiyama, M. Hashimoto, H. Takadama, F. Magata, Y. Yokogawa, K. Sassa, K. Iwai and S. Asai, Mater. Trans., 46[11] (2005) 2514-2517

[71] Y. Sakka, K. Takahashi, T. S. Suzuki, S. Ito and N. Matsuda, Mater. Sci. Eng. A, 475 (2008) 27-33

[72] T. S. Suzuki and Y. Sakka, Jpn. J. Appl. Phys., 41 (2002) 1272-1274

[73] A. Makiya, Y. Kusumi, S. Tanaka, Z. Kato, N. Uchida, K. Uematsu, T. Kimura and K. Kitazawa, J. Eur. Ceram. Soc., 27 (2007) 797-799

[74] X. W. Zhu, T. S. Suzuki, T. Uchikoshi, T. Nishimura and Y. Sakka, J. Ceram. Soc. Jpn., 114[11] (2006) 979-987

[75] X. W. Zhu, Y. Sakka, T. S. Suzuki, T. Uchikoshi and S. Kikkawa, Acta Mater., 58 (2010) 146-161

[76] T. S. Suzuki and Y. Sakka, Scripta Mater., 52 (2005) 583-586

[77] T. S. Suzuki, T. Uchikoshi and Y. Sakka, J. Eur. Ceram. Soc., 29 (2009) 2627-2633

[78] T. S. Suzuki, T. Uchikoshi and Y. Sakka, Mater. Trans., 48[11] (2007) 2883-2887

[79] T. S. Suzuki, T. Ushikoshi and Y. Sakka, J. Eur. Ceram. Soc., 30 (2010) 2813-2817

[80] A. Makiya, D. Kusuno, S. Tanaka, N. Uchida, K. Uematsu, T. Kimura, K. Kitazawa and Y. Doshida, J. Ceram. Soc. Jpn., 111 [9] (2003) 702-704

[81] Y. Doshida, K. Tsuzuku, H. Kishi, A. Makiya, S. Tanaka, K. Uematsu and T. Kimura, J. Ceram. Soc. Jpn., 43 [9B] (2004) 6645-6648

[82] T. S. Suzuki, M. Kimura, K. Shiratsuyu, A. Ando, Y. Sakka and Y. Sakabe, App. Phys. Lett., 89 (2006) 132902

[83] K. Tabara, A. Makiya, S. Tanaka, K. Uematsu and Y. Doshida, J. Ceram. Soc. Jpn., 115[3] (2007) 237-240 [in Japanese]

[84] S. Tanaka, Y. Tomita, R. Furushima, H. Shimizu, Y. Doshida and K. Uematsu, Sci. Technol. Adv. Mater., 10 (2009) 014602

[85] Y. Doshida, H. Kishi, A. Makiya, S. Tanaka, K. Uematsu and T. Kimura, Jpn. J. Appl. Phys., 45[9B] (2006) 7460-7464

[86] S. Tanaka, Y. Doshida, H. Shimizu, R. Furushima and K. Uematsu, IOP Conf. Ser.: Mater. Sci. Eng., 20 (2011) 012002

[87] S. Tanaka, A. Makiya, T. Okada, T. Kawase, Z. Kato and K. Uematsu, J. Am. Ceram. Soc., 90[11] (2007) 3503-3506

[88] S. Tanaka, T. Takahashi, R. Furushima, A. Makiya and K. Uematsu, J. Ceram. Soc. Jpn., 118[8] (2010) 722-725

[89] T. Kubota, N. Tanaka, K. Kageyama, H. Takagi, Y. Sakabe, T. S. Suzuki and Y. Sakka, Jpn. J. App. Phys., 48 (2009) 031405

[90] T. Takahashi, S. Tanaka, R. Furushima, Z. Kato and K. Uematsu, IOP Conf. Ser.: Mater. Sci. Eng., 18 (2011) 062013

[91] H. Shimizu, Y. Doshida, S. Tanaka and K. Uematsu, Jpn. J. Appl. Phys., 47 (2008) 7693-7697

[92] H. Shimizu, Y. Doshida, S. Tanaka and K. Uematsu, Key Eng. Mater., 421-422 (2010) 21-25

[93] S. Tanaka, T. Takahashi and K. Uematsu, J. Eur. Ceram. Soc., 34[15] (2014) 3723-3728

[94] M. Yamaki, S. Horil, M. Haruta and J. Shimoyama, Jpn. J. Appl. Phys., 51 (2012) 010107

[95] S. Horii, S. Okuhira, M. Tamaki, K. Kishio, J. Shimoyama and T. Doi, J. Appl. Phys., 115 (2014) 113908

[96] S. Stassen, A. Vanderschueren, R. Cloots, A. Rulmont and M. Ausloos, J. Cryst. Growth, 166 (1996) 281-285

[97] C. Uyeda, Jpn. J. Appl. Phys., 32 (1993) 268-270

[98] C. Uyeda, K. Tanaka, R. Takashima and M. Sakakibara, J. Jpn. Appl. Phys., 43[3] (2004) 980-984

[99] P. Liu, H. Yi, G. Zhou, J. Zhang and S. Wang, Opt. Mater. Express, 5 (2015) 441-446

[100] A. Pringuet, T. Takahashi, S. Baba, Y. Kamo, Z. Kato, K. Uematsu and S. Tanaka, J. Am. Ceram. Soc., (2016) 1-3

[101] T. Ashikaga, B. -N. Kim, H. Kiyono and T. S. Suzuki, J. Eur. Ceram. Soc., 38 (2018) 2735-2741

[102] K. Morita, H. Toshida and B. -N. Kim, J. Jpn. Soc. Pow. Pow. Metal., 66[4] (2019) 158-167 [in Japanese]

[103] J. Akiyama, Y. Sato and T. Taira, Opt. Lett., 35[21] (2010) 3598-3600

[104] Y. Sato, J. Akiyama and T. Taira, Phys. Status Solidi C, 10[6] (2013) 896-902

[105] Y. Sato, M. Arzakantsyan, J. Akiyama and T. Taira, Opt. Mater. Express, 4[10] (2014) 2006-2015

[106] T. Takahashi, M. Sado, N. Sugimoto, J. Tatami, M. Iijima, S. Inagaki, Y. Kubota, I. Yamamoto and S. Tanaka, Adv. Pow. Tech., 27 (2016) 2005-2011

[107] J. Sievers, 45 (1982) 289-296

[108] C. Uyeda and K. Hisayoshi, Space Utiliz. Res., 28 (2012) 18-22
[109] R. Furushima, S. Tanaka, Z. Kato and K. Uematsu, IOP Conf. Ser.: Mater. Sci. Eng., 18 (2011) 062008
[110] R. W. Rice, Ceramic fabrication technology, Marcel dekker, Inc. (2003) pp.121-135
[111] H. Kaga, Y. Hinemuchi, S. Tanaka, A. Makiya, Z. Kato, K. Uematsu and K. Watari, J. Ceram. Soc. Jpn., 114[11] (2006) 1085-1088
[112] H. Kaga, Y. Kinemuchi, H. Yilmaz, K. Watari, H. Nakano, H. Nakano, S. Tanaka, A. Makiya, Z. Kato, K. Uematsu, Acta Mater., 55 (2007) 4753-4757
[113] W. Chen, Y. Kinemuchi, K. Watari, T. Tamura and K. Miwa, J. Am. Ceram. Soc., 89[9] (2006) 2645-2648
[114] Z. Yang, J. Yu, K. Deng, L. Lan, H. Wang, Z. Ren, Q. Wang, Y. Dai and H. Wang, Mater. Lett., 135 (2014) 218-221
[115] A. Szudarska, Y. Sakka, T. S. Suzuki, T. Mizerski and M. Szafran, Ceram. Int., 42 (2016) 294-301
[116] O.O. Omatete, M. A. Janney and S. D. Nunn, J. Eur. Ceram. Soc., 17 (1997) 407-413
[117] L. Montanaro, B. Coppola, P. Palmero and J. -M. Tulliani, Ceram. Int., 45 (2019) 9653-9673
[118] T. Kimura, M. Yamato, W. Koshimizu, M. Koike and T. Kawai, Langmuir, 16 (2000) 858-861
[119] T. Kimura, M. Yoshino, T. Yamane, M. Yamato and M. Tobita, Langmuir, 20 (2004) 5669-5672
[120] T. Kimura, Jpn. J. Appl. Phys., 48 (2009) 020217
[121] K. Iwai, Jpn. J. Appl. Phys., 49 (2010) 125602
[122] T. Kimura and M. Yoshino, Langmuir, 21 (2005) 4805-4808
[123] N. Hirota, T. Ando, T. Shimada, H. Wada and Y. Sakka, Sci. Technol. Adv. Mater., 9 (2008) 024211
[124] E. Suvaci and G. L. Messing, J. Am. Ceram. Soc., 83[8] (2000) 2041-2048
[125] M. W. Seabaugh, G. L. Messing and M. D. Vaudin, J. Am. Ceram. Soc., 83[12] (2000) 3109-3116
[126] E. Suvaci and I. O. Ozer, J. Eur. Ceram. Soc., 25 (2005) 1663-1673
[127] C. Duran, S. Trolier-McKinstry and G. L. Messing, J. Mater. Res., 17[9] (2002) 228-238
[128] S. Alkoy, C. Duran and D. A. Hall, J. Am. Ceram. Soc., 91[5] (2008) 1597-1602
[129] L. Wei, X. Chao, X. Han and Z. Yang, Mater. Res. Bull., 52 (2014) 65-69
[130] A. Shui, Doctor thesis, Nagaoka University of Technology (2002)

[131] T. Takuma, S. Tanaka, Z. Kato and K. Uematsu, J. Ceram. Soc. Jpn., 121[5] (2013) 411-415

[132] T. Chartier, R. Penerroya, C. Pagnoux and J. F. Baumard, J. Eur. Ceram. Soc., 17 (1997) 765-771

[133] T. Chartier, C. Hinczewski and S. Corbel, J. Eur. Ceram. Soc., 19 (1999) 67-74

[134] T. Chartier, A. Badev, Y. Abouliatim, P. Lebaudy and L. Lecamp, J. Eur. Ceram. Soc., 32 (2012) 1625-1634

[135] S. P. Gentry and J. W. Halloran, J. Eur. Ceram. Soc., 35 (2015) 1895-1904

[136] M. L. Griffith and J. W. Halloran, J. Am. Ceram. Soc., 79[10] (1996) 2601-2608

[137] R. R. Neurgaonkar, J. R. Oliver and W. K. Cory, Ferroelectrics, 160 (1994) 265-276

[138] R. -J. Xie, Y. Akimune, R. -P. Wang and N. Hirosaki, J. Am. Ceram. Soc., 85[11] (2002) 2731-2737

[139] H. Shimizu, Y. Doshida, Y. Mizuno, S. Tanaka, K. Uematsu and H. Tamura, Jpn. J. Appl. Phy., 51 (2012) 09LD02

[140] H. Aoki, Surf. Sci., 10 (1989) 96-101 [in Japanese]

[141] M. Aizawa, T. Matsuura and Z. Zhuang, Biol. Pharm. Bull., 36[11] (2013) 1654-1661

[142] T. Kawasaki, J. Chromatogr. A, 544 (1991) 147-184

[143] T. Nakano, K. Kaibara, Y. Tabata, N. Nagata, S. Enomoto, E. Marukawa and Y. Umakoshi, Bone, 31(4) (2002) 479-487

[144] M. Iijima, H. Tohda and Y. Moriwaki, J. Cryst. Growth, 116 (1992) 319-326

Chapter 2

Colloidal Processing in Rotating Magnetic Field Using Photopolymerization Reaction

2.1 INTRODUCTION

Particle-orientation is expected to improve the functional properties of polycrystalline ceramics [1]-[3]. Colloidal processing in a high magnetic field has attracted the researcher's interests as a promising method for preparing crystal-oriented ceramics [4]-[13]. This method involves tape casting, slip casting, or gel casting in a magnetic field. The cast slurry is solidified by some method after orienting the particles in a magnetic field to form a compact. The compact is then sintered in a standard electric furnace. The advantages of this technique include to use any shape particles and to be able to select the orient direction of particles. This means that conventional fine raw powders can be used in this method. This is effective for densification by sintering. Furthermore, even when elongated particles are used, the long axis direction with excellent property can be aligned perpendicular to the green sheet. On the other hand, a drawback of this method is that the length of time required for shaping the material is high [4]-[11]. This is because tape casting, slip casting, or gel casting in a magnetic field takes tens of minutes or more to consolidation by evaporation, dehydration, or gelation. This drawback should be solved in order to apply this method for mass production. Furthermore, continuous processing is preferable for large-scale production. The development of a novel consolidation method is required in order to shorten the shaping time under the magnetic field.

The objectives of this chapter were to develop a novel method to shorten the solidification time in the magnetic field and to fabricate highly particle-oriented structures. Here, it is required that the particles do not solidify until they are aligned but can be solidified immediately after alignment. I focused on the photopolymerization reaction using tape casting processing. Chartier et al. reported a solvent-free tape casting process in which they studied the dispersion of particles in UV curable binder and the photopolymerization reaction [14,15]. In this chapter, $(Sr,Ca)_2NaNb_5O_{15}$ (hereafter, referred to as SCNN) powder was used as a raw material [16]-[19]. The preparation of dispersed SCNN slurry with UV curable resin was examined. The effects of the concentration of the photoinitiator, ceramics powder in the slurry and the exposure energy of UV rays on the cured depth were also investigated. *C*-axis oriented SCNN green sheet within a short time under a high magnetic field was fabricated.

2.2 EXPERIMENTAL PROCEDURE

2.2.1 Materials

$(Sr,Ca)_2NaNb_5O_{15}$ powder synthesized by a conventional solid-state reaction was used in this study [19]. Reagent-grade $SrCO_3$, $CaCO_3$, Na_2CO_3, and Nb_2O_5 powder were weighed according to the following composition; $Sr_{1.9}Ca_{0.1}NaNb_5O_{15}$. The weighed powders were mixed by ball milling in ethanol. After drying, the mixtures were heat-treated at 1230 °C in air. This powder was deagglomerated by ball milling in an azeotropic mixture solvent consisting of methyl ethyl ketone (MEK) and ethanol (EtOH) (60/40 vol.) [20]-[22]. A zirconia ball having a diameter of 2.0 mm was used. The solvent was evaporated in a dryer at 45 °C for 3h. The morphology of the powder was observed by the scanning electron microscopy SEM (JSM-5310LVB, JEOL Tokyo, Japan). The true density of SCNN powder was measured by the pycnometer method using Geryusac type pycnometer.

The UV curable resin used in this study contains a polyester acrylate monomer diluted into hydroxyethyl methacrylate (Ebecryl 770, DAICEL-ALLNEX LTD. Japan) and a 2-hydroxy-2-methyl-1-phenyl-propan-1 (Darocur 1173, Ciba-Japan, Japan) as a photoinitiator. An extinction coefficient *e* of this photoinitiator in the UV ray range is that *e* = 2,710 at 260 nm and *e* = 9 at 360 nm. A phosphate ester (DISPERBYK-110, BYK-Chemie Japan) was used as a dispersant that acts by both electrostatic and steric repulsion in low dielectric constant media.[20]

2.2.2 Preparation of Slurry

The dispersant and the photoinitiator were firstly completely dissolved in the UV curable acrylate binder, and then the deagglomerated SCNN powder was added into the binder. The amount of dispersant was varied from 0.3 to 1.5wt% (dispersant concentration relative to the powder mass). The amount of photoinitiator was also varied from 0.5 to 6.0 wt% (photoinitiator concentration relative to the total mass of the slurry). The slurry was first treated with an ultrasonic bath for 5 min and was stirred using the planetary centrifugal mixer (Awatorirentaro. Are310, Thinky, Tokyo) with the defoaming mode at 2000 rpm for 30 s. Then, the slurry was stirred twice using the thin-film spin system high-speed mixer (FILMIX Model30-L, PRIMIX Co. Japan) for 5 min at 500 rpm and 10 min at 2000 rpm. Mixing steps were performed at a temperature of 40 °C. Finally, the slurry was de-aired by the planetary centrifugal mixer in the defoaming mode at 2000 rpm for 30 s.

Rheological measurements of the slurry were performed with a rheometer (Physica MCR301, Anton Paar, Austria) by using a cone-plate apparatus (Anton Paar, CP25-2, diameter: 24.966 mm, angle: 2.003°, truncation: 52μm) in the stress-controlled mode. The shear rate was varied from 0.001 s^{-1} to 100 s^{-1}. The measurement temperature was set to 20 °C.

2.2.3 UV Curing of Slurry

The UV curing process, which is a photopolymerization reaction, was performed by applying UV rays emitted from a lamp (MUV-250U-L, MORITEX Co. Japan) to the slurry. Prior to shaping, the UV power was measured using a UV radiometer (UIT-250, USHIO INC. Japan). The wavelength output spectra of the lamp ranging from 200 to 450 nm with peak intensity at 365 nm. The average UV power I applied to the slurry was about 360 mW/cm^2. The UV incident energy E (i.e., the exposure amount) is expressed as the product of the average power of UV light I and the time t when the slurry is placed under the lamp, $E = It$. The UV radiation was absorbed by the photoinitiator and the polymerization was initiated by free radicals generated. The photopolymerizable solution

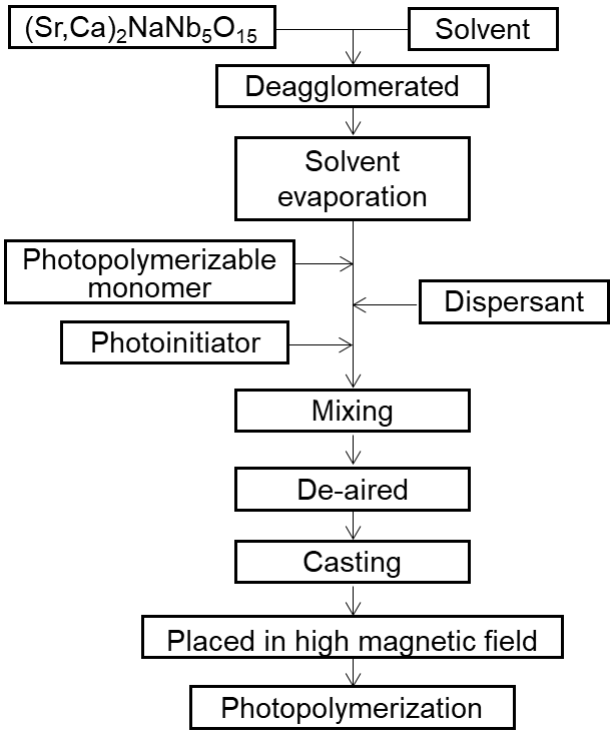

FIGURE 2.1 Flow chart of preparation of *c*-axis oriented green sheets by colloidal processing under the high magnetic field and UV curing.

instantly cured when exposed to UV rays and becomes a high-strength green sheet by enclosing ceramics particles in it. After irradiating the slurry with UV rays, the cured green sheet was picked up and the remaining non-polymerized liquid was removed by ethanol. The thickness of the polymerization sheet was measured with a micrometer as the cure depth of the slurry.

2.2.4 Fabrication of Green Sheets in Rotating Magnetic Field

Figure 2.1 shows a flow chart of the preparation of *c*-axis oriented green sheets by colloidal processing with the high magnetic field and UV curing. The slurry was cast on a poly (ethylene terephthalate) (PET) film, and then placed in a magnetic field of 10 T induced by a superconducting magnet (TM-10VH10, TOSHIBA Co. Japan) for 1 - 300 s. It was irradiated with UV rays for 30 s (E=10.8 J/cm^2). A static magnetic field of 10 T was applied in the direction parallel to the sheet surface, and the sheet was rotated horizontally at a rotation speed of 30 rpm. This method is expected to align the *c*-axis of the particles in the vertical direction of the sheet. (Figures 2.2 and 2.3). For comparison, a randomly oriented green sheet was formed by a UV photopolymerization reaction without a magnetic field.

The crystal-oriented structures of the surface of the green sheets were evaluated by X-ray diffraction (XRD, Ultima-IV, RIGAKU Japan) with Cu-Kα_1 radiation for a 2θ range of 20 - 70 °. The degree of *c*-axis orientation was evaluated in terms of the Lotgering factor LF of [00l] orientation, $LF = (p - p_0)/(1 - p_0)$, where $p = \sum I(00l) / \sum I(hkl)$, $p_0 = p$ for randomly oriented ceramic samples, and $\sum I(hkl)$ is the summation of the XRD peak intensities [23].

2.2.5 Binder Removal and Sintering

The program of de-binding of the green sheets was determined from thermogravimetric analysis (DTG-60H, SHIMADZU, Japan) of the cured green tape. The thermogravimetric analysis was performed at a heating rate of 5 °C/min up to a temperature of 800 °C in air. The de-binding of both the *c*-axis oriented and randomly oriented green sheets was performed at a heating rate of 1 °C/min up to the temperature of 100 °C and 0.2 °C/min up to the temperature of 500 °C.

Then, the sheets were sintered at a temperature of 1250 °C for 6 h. A heating rate was 5 °C/min. The relative density of the ceramic sheet was measured using the Archimedes method.

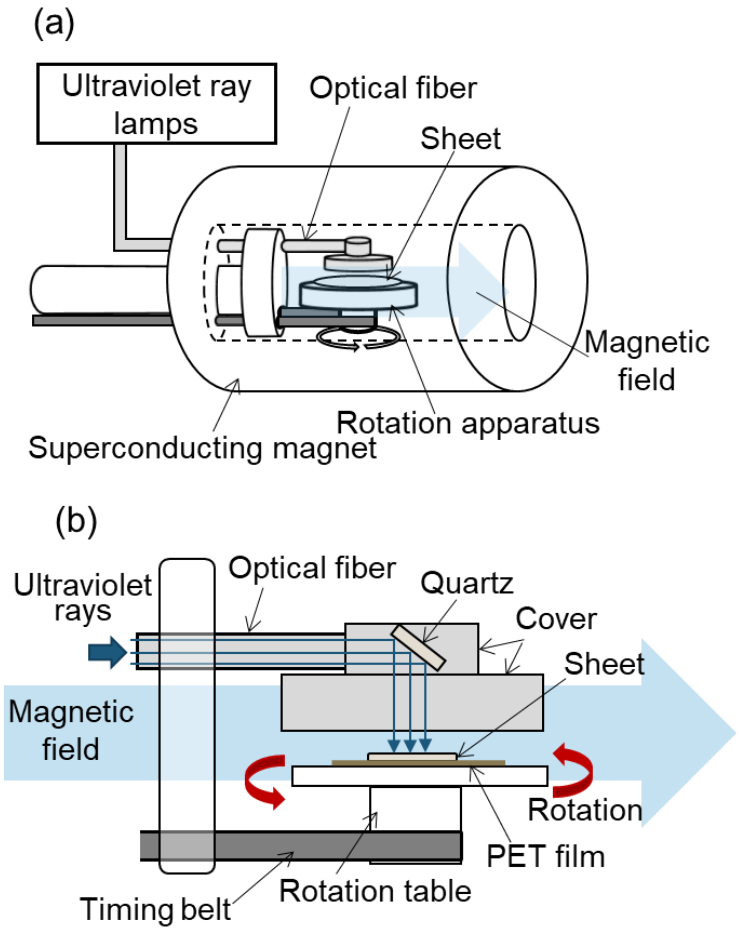

FIGURE 2.2 Schematic illustrations of experimental setting. (a) Rotation apparatus and optical fiber in the unidirectional high magnetic field induced by a superconducting magnet, and (b) an expanded view of the sheet casted on a PET film and exposure to UV light in a magnetic field.

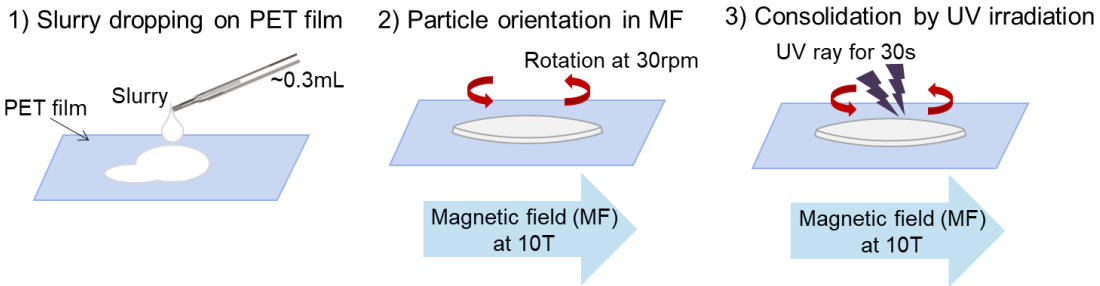

FIGURE 2.3 The illustration of the forming process with photopolymerization reactions in the magnetic field.

The crystal-oriented structures of the surface of the ceramic sheets were evaluated by the Lotgering's methods using XRD. The microstructures of both the surface and the cross-section of the sintered sheets were observed by using the scanning electron microscope (SEM). All sintered bodies were coated with gold for SEM observation.

2.3 RESULTS AND DISCUSSION

2.3.1 SCNN Powder

Figure 2.4 shows SEM images of the synthesized raw and deagglomerated SCNN powder. A majority of synthesized powder has isotropic shapes or plate-like shapes. After ball milling, the particles deagglomerated and the particle size was reduced. The median particle size D_{50} of deagglomerated powder was 1.0 μm. The true density of SCNN powders was 4.96 g/cm^2.

2.3.2 Viscosity and Cured Depth of Slurry

The concentration of the dispersant was optimized in the slurry system, which consisted of the powder of 30 vol% in the UV curable resin with the phosphate ester dispersant. Figure 2.5 shows the viscosity of the SCNN slurry at a shear of 100 s^{-1} plotted against dispersant concentration. The amounts of dispersant varied from 0.3 to 1.5 wt% (dispersant to SCNN ratio). A lower viscosity, which indicates a well-dispersed state, was attained for the addition of 1.2 wt% of dispersant.

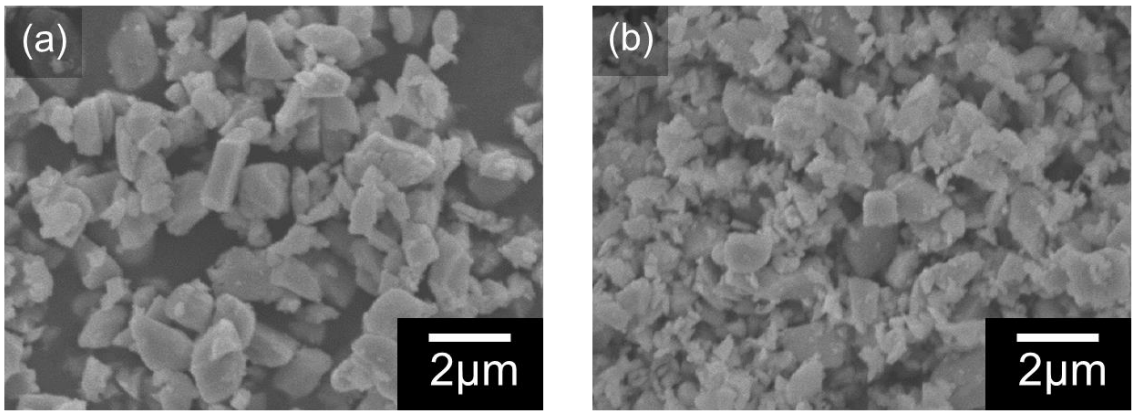

FIGURE 2.4 SEM images of (a) raw powder and (b) deagglomerated powder.

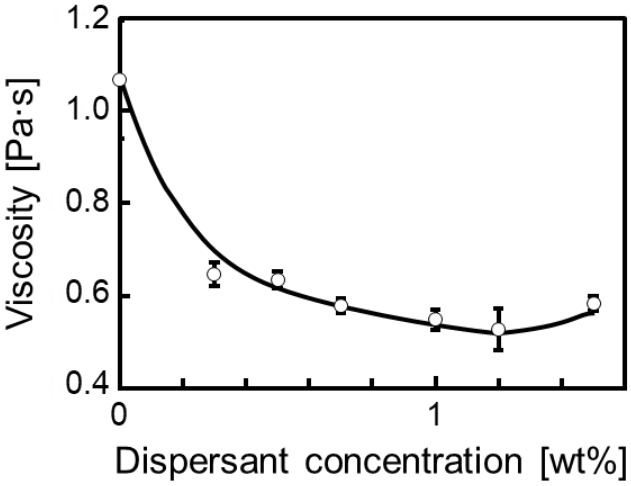

FIGURE 2.5 Viscosity (at a shear rate of 100 s^{-1}) of slurry containing 30 vol% SCNN powder in UV curable resin for various amounts of phosphate ester.

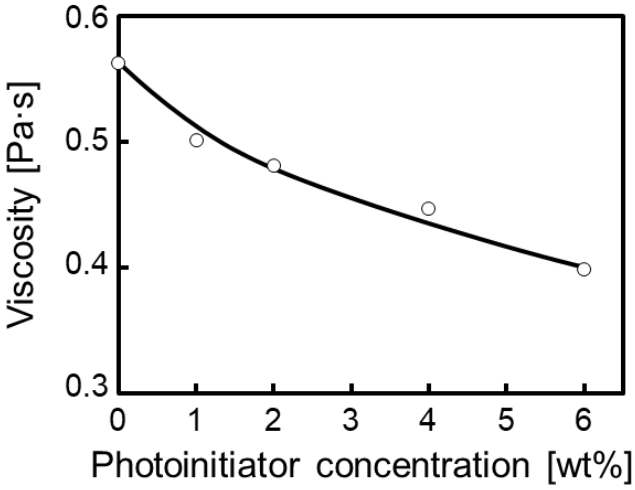

FIGURE 2.6 Viscosity (at a shear rate of 100 s^{-1}) of slurry containing 30 vol% SCNN powder in UV curable resin and dispersant for various amounts of photoinitiator.

The best photoinitiator concentration was decided after careful thought of the cured depth of the slurry as well as the slurry viscosity.The photoinitiator concentration was also optimized in the slurry with 30 vol% SCNN powder and 1.2 wt% phosphate ester. The amount of the photoinitiator was varied from 1.0 to 6.0 wt% to the SCNN powder and solvent. The viscosity of the slurry at a shear rate of 100 s^{-1} is plotted in Fig. 2.6. The addition of the photoinitiator let to a drastic decrease in the viscosity of the slurry.

Figure 2.7 shows the influence of the amount of photoinitiator on the cured depth of the slurry. The SCNN slurry was exposed to UV radiation at two conditions, E = 10.8 and 21.8 J/cm^2 (i.e., UV rays was exposed for 30 s or 60 s on the top of the slurry). The maximum of the cured depth increases with increasing the UV irradiation energy. The

cured depth presents a maximum value for the addition of 1.0 wt% photoinitiator. In the first part of the curved, the cured depth of the slurry increased with increasing the amount of the photoinitiator. This result indicates that the increase of the concentration of the photoinitiator induces the formation of more radicals. At higher concentrations of photoinitiator, however, the cured depth was saturated. This suggests that the upper layers of the slurry rapidly cause the polymerization reaction due to the generation of a significant number of radicals. Then, the incident UV rays cannot penetrate deeply to the bottom layers in the slurry. The tendency is the same as the results of references [14, 15].

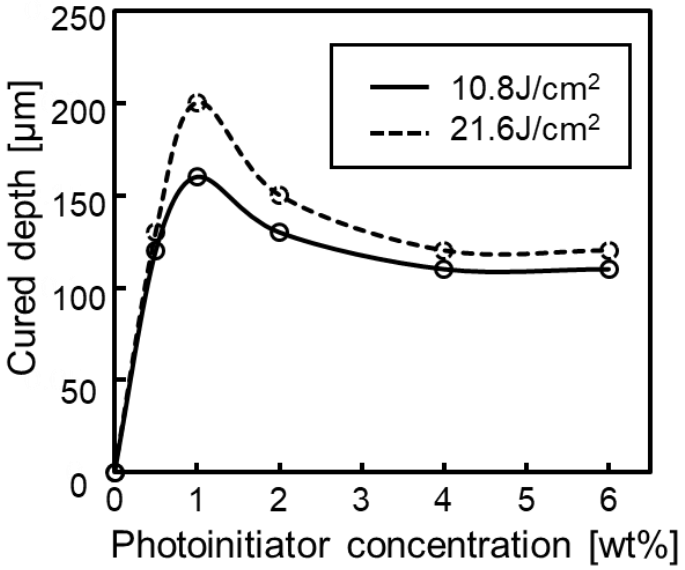

FIGURE 2.7 Cured depth of slurry containing 30 vol% SCNN powder in UV curable resin and 1.2 wt% dispersant for various amounts of photoinitiator. The conditions of UV incident energy E were 10.8 J/cm^2 and 21.6 J/cm^2.

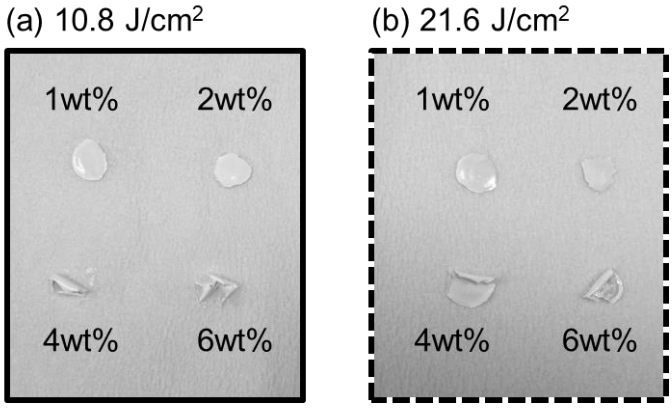

FIGURE 2.8 Appearance of green sheets fabricated from slurry containing 30 vol% SCNN powder in UV curable resin and 1.2 wt% dispersant for various amounts of photoinitiator. The conditions of UV incident energy E were (a) 10.8 J/cm^2 and (b) 21.6 J/cm^2.

Figure 2.8 shows the appearance of polymerized green sheets prepared from 30vol% SCNN slurry containing the various amount of photoinitiators. The energy of the exposed UV rays was 10.8 and 21.6 J/cm^2. The shape of polymerized green sheets was maintained for the additions of photoinitiator smaller than 2 wt%. The amount of the photoinitiator decided on 2 wt% from the results of both the slurry viscosity and the shape of the fabricated green sheets.

Figure 2.9 shows viscosity curves obtained from the slurry with solid concentration of 30 to 55 vol%. The viscosity increased extremely with increasing solid content. The viscosity of the slurry with solid contents over 45 vol% decreased sharply with increasing shear rate. A slurry with a high solid concentration of 55 vol% could be prepared under the optimized conditions. This suggests that the particles are dispersed in the slurry prepared by using UV curable resin.

Figure 2.10 shows the cured depth of the slurry versus the solid content in SCNN slurry. The UV incident energy E was 10.8 J/cm^2. The cured depth of the slurry decreases with the increase of the solid contents due to the increase in the absorption and the scattering phenomenon by particles. Figure 2.11 shows the various cured depth versus UV exposure time for the slurry containing SCNN powder of 55 vol%. As expected, the cured depth increases with increasing the UV irradiation time, i.e., the UV incident energy E. And, the cured depth of the slurry was saturated at 30 s (E = 10.8 J/cm^2). Figure 2.12 shows the appearance of the polymerized sheet by irradiation of UV light at just 30 s. The obtained sample thickness was ~100 μm, and the diameter was ~15 mm.

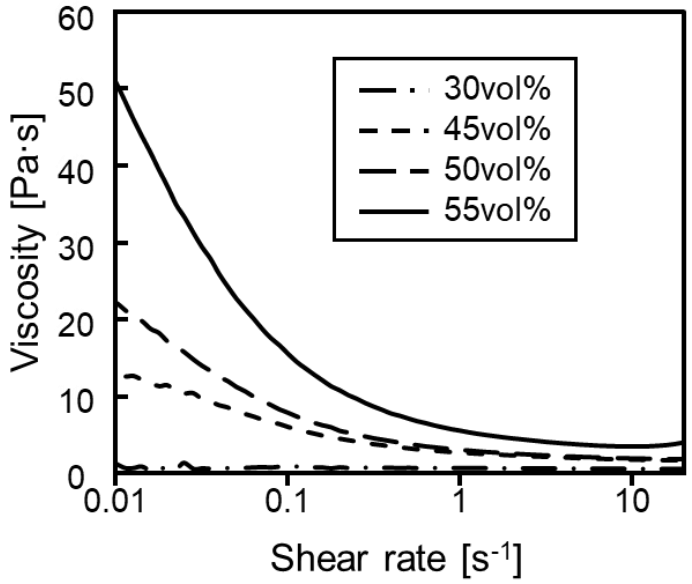

FIGURE 2.9 Shear viscosity of slurry containing 30 - 55 vol% SCNN powder, UV curable resin, 1.2 wt% dispersant and 2.0 wt% photoinitiator.

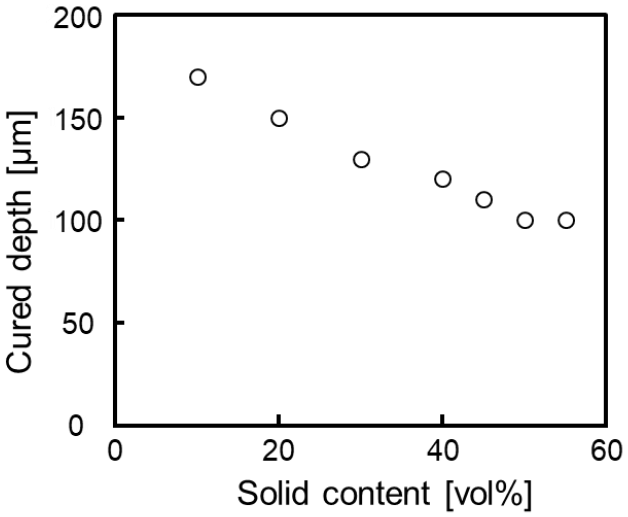

FIGURE 2.10 Cured depth versus the solid contents for SCNN slurry consisting of UV curable resin, 1.2 wt% dispersant and 2.0 wt% photoinitiator. UV incident energy *E* was 10.8 J/cm^2.

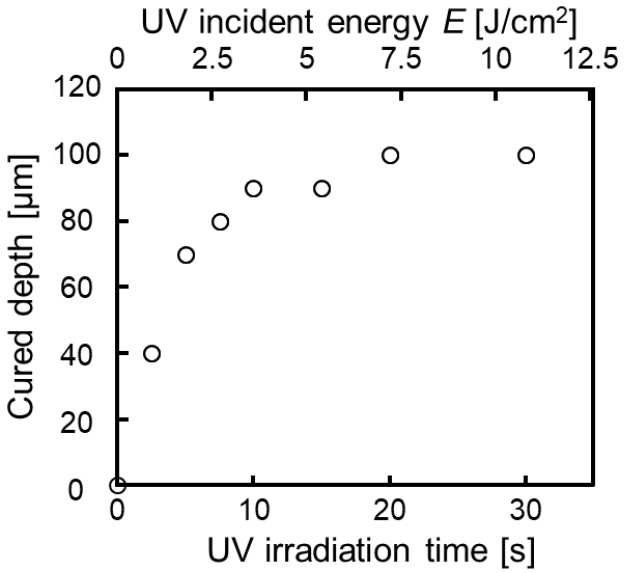

FIGURE 2.11 Cured depth versus UV irradiation time and UV incident energy *E* for 55 vol% SCNN polymerized green sheets.

FIGURE 2.12 Photograph of green sheet.

2.3.3 Structure of Green and Sintered Sheets

Figure 2.13 shows XRD patterns of the polymerized green sheets prepared for a duration time of 10 s and 300 s with and without rotating magnetic fields. At the duration time in the magnetic field was increased, the intensities of the peaks from *c*-planes of the crystal, such as the 001 and 002 planes, became gradually high. In contrast, the diffraction peaks of the green sheet prepared without the magnetic field were equivalent to those of the International Centre for Diffraction Data (ICDD) card No. 00-034-0429 for $Sr_2NaNb_5O_{15}$. The degree of orientation was evaluated as the Lotgering factor *LF*, which is calculated from the equation $LF = (p - p_0)/(1 - p_0)$, where $p_0 = \sum I_0(00l) / \sum I_0(hkl)$ and $p = \sum I(00l) / \sum I(hkl)$. I_0 and I are the intensities of the XRD patterns of random and oriented samples obtained from the experiments, respectively. The *LF* was 0.81 for the sample prepared in the rotating magnetic field with a holding time of 300 s. The result shows that a particle-oriented green sheet could be fabricated by the photopolymerized reaction in the magnetic field. The *LF* of the sample is considerably high compared to that of the sample prepared by the conventional process. This suggests that the dispersed state of particles is well attained in the slurry. Moreover, the consolidation of using a photopolymerization reaction is that it is also useful for maintaining the particle-oriented microstructure, because the reaction completes quickly before the sedimentation or flocculation of particles in the slurry. This tendency is the same as a result in the case of using gel-casting processing [13].

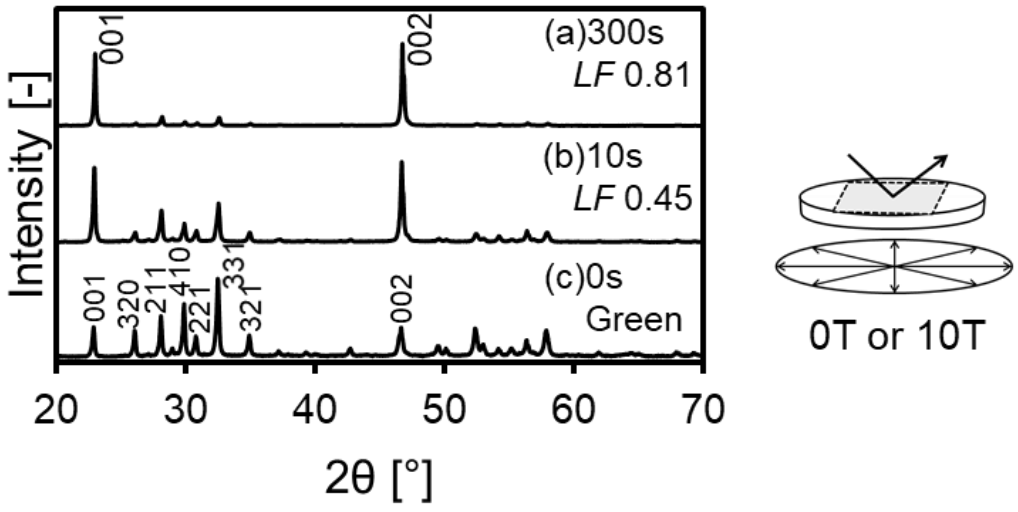

FIGURE 2.13 X-ray diffraction patterns obtained from green sheets for various duration times of (a) 300 s and (b) 10 s (a and b) with and (c) without a 10 T rotating magnetic field.

Figure 2.14 shows the thermogravimetric reduction curve of the polymerized green sheets. The weight of the sample became constant over the temperature at 500 °C. Thus, the organic species were completely removed at a temperature of 500 °C.

Figure 2.15 shows XRD patterns of the top surface of the sintered sheets obtained by the sintering of the green sheets. The duration times of the green sheets in the magnetic field were 10 s and 300 s, respectively. The *LF* was 0.94 for the sample formed at a duration time of 300 s in the rotating magnetic field and was improved during sintering. The results showed that *c*-axis oriented SCNN sheets were produced by the sintering of the particle-oriented green sheets.

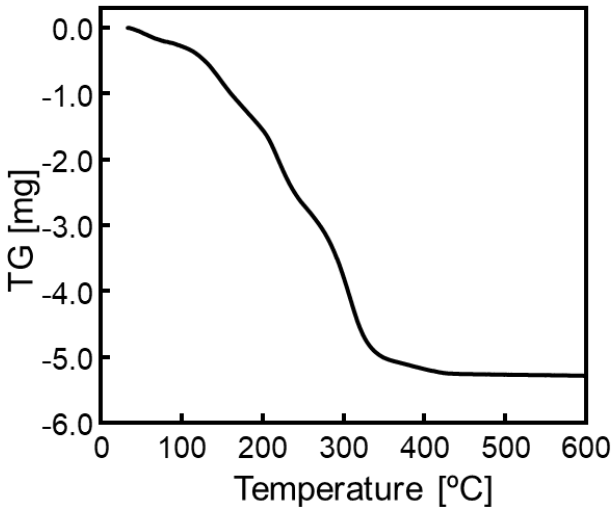

FIGURE 2.14 Thermogravimetric analysis of the cured green tapes prepared from the 30 vol% slurry.

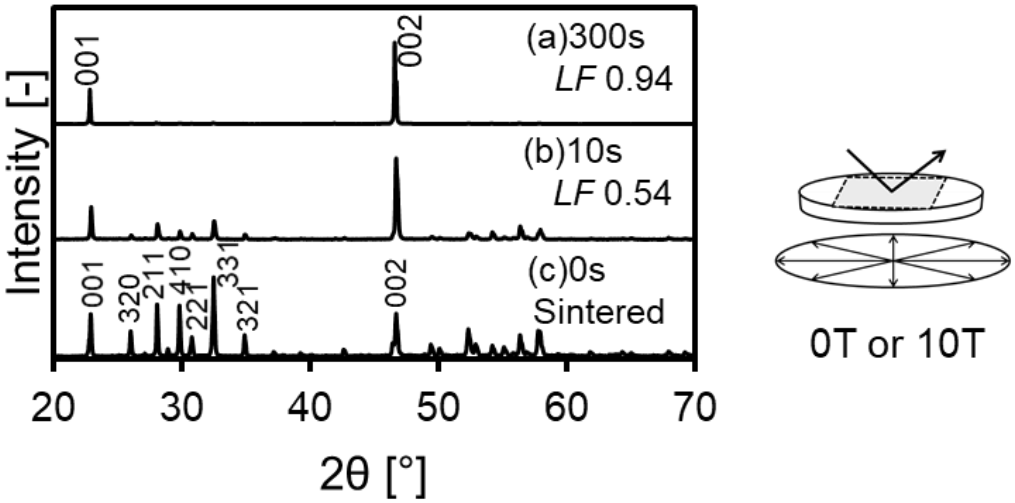

FIGURE 2.15 X-ray diffraction patterns obtained from sintered sheets for various duration times of (a) 300 s and (b) 10 s (a and b) with and (c) without a 10 T rotating magnetic field.

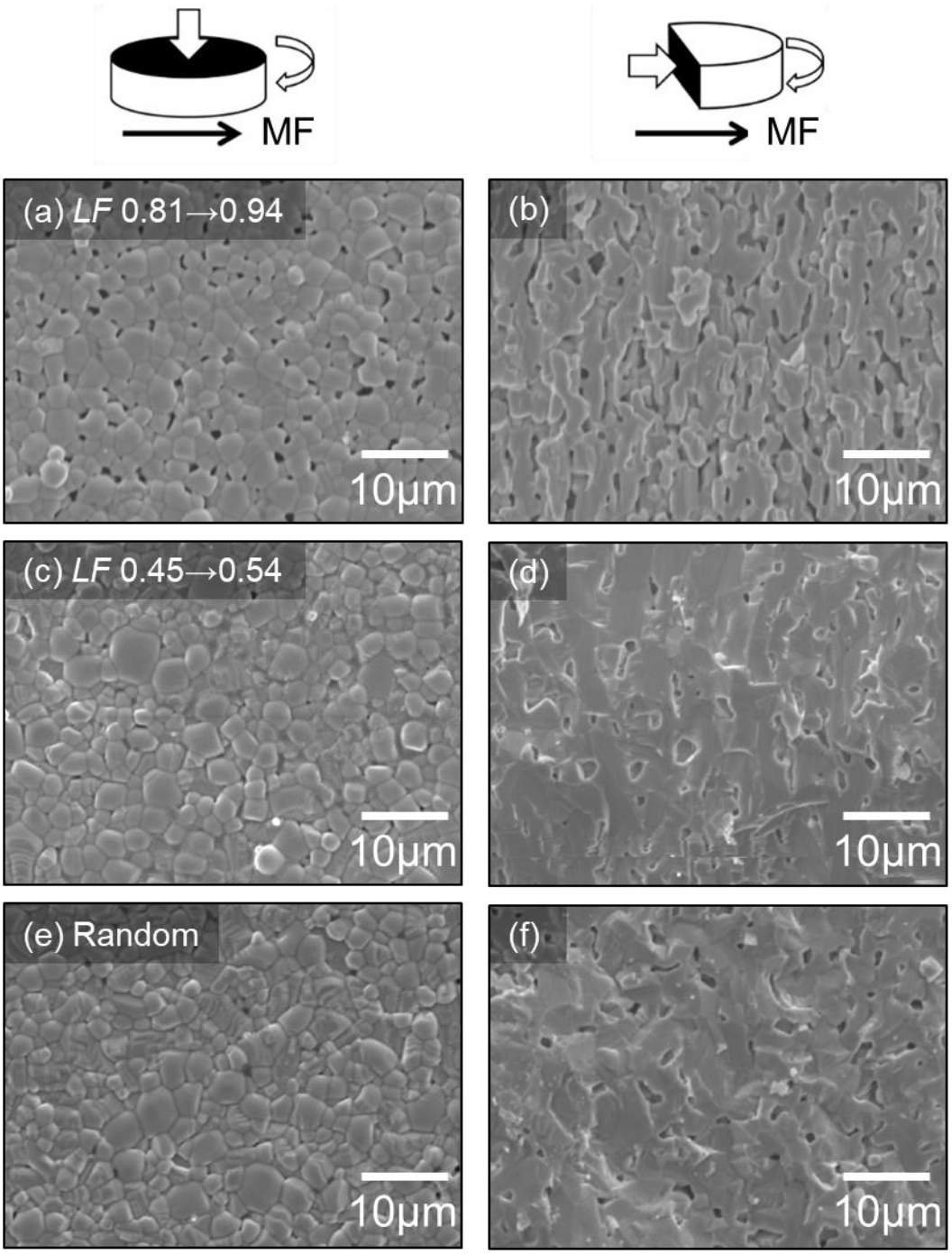

FIGURE 2.16 Microstructure of sintered SCNN ceramics at 1250 ºC observed from the (a, c and e) perpendicular and (b, d and f) parallel directions. (a and b) holding time of 300 s and (c and d) holding time of 10 s with a 10 T rotating magnetic field, and (e and f) without a 10 T rotating magnetic field.

Figures 2.16 (a-d) shows SEM micrographs of the microstructure of the sintered sheets observed from the parallel and perpendicular directions to the rotating magnetic field. The duration time in the magnetic field was 10 s and 300 s. The microstructure of the sintered sheets prepared without the magnetic field is also shown in Figs. 2.16 (e, f). A significant difference was noted in the structures observed from the two directions of the sheets fabricated under the magnetic field. The grains were oriented parallel to the rotating axis of the magnetic field and the elongated pores were present in the sintered sheets prepared with the magnetic field. In particular, it was clearly observed in the highly oriented sheets. This microstructure suggests that the oriented particles grow in the *c*-axis direction during sintering, and the grain-growth of the oriented particles contributed to the enhancement of the oriented structure [17]. The anisotropic grain growth is detailed in Chapter 4 in order to elucidate a mechanism of microstructure development during sintering for *c*-axis oriented SCNN material.

Figure 2.17 shows the correlation of *LF* of green sheets as a function of that of sintered sheets and the relative density. The value of *LF* constantly increased after sintering, whereas the relative density gradually decreased with increasing the value of *LF*. This tendency is the same as the previous results [24]. These results indicate that a high degree of orientation is not necessary for green bodies or sheets, and the *LF* of green bodies and sheets was suitable in the range of 0.3 - 0.6.

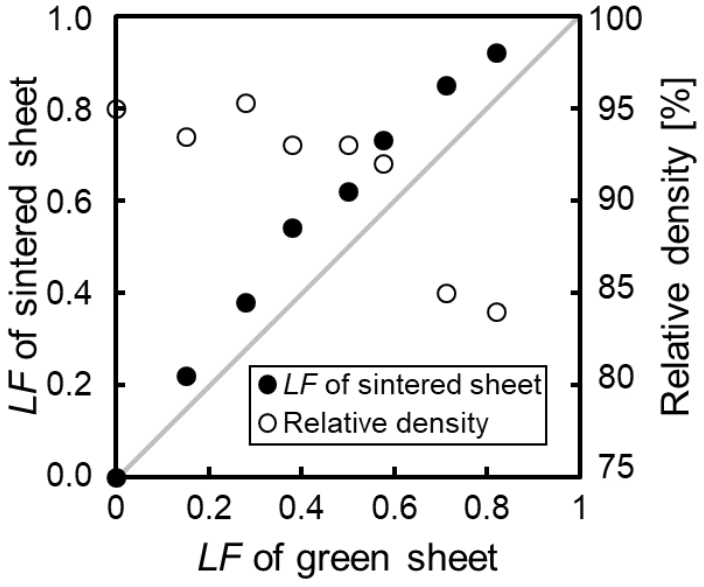

FIGURE 2.17 The correlation between *LF* of green sheets calculated from the X-ray diffraction patterns and that of sintered sheets, and relative density of sintered ceramics at 1250 ^{o}C.

2.4 CONCLUSIONS

Novel colloidal processing using UV curable resin was studied. This technique can shorten the drying time in a magnetic field by using a fast photopolymerization reaction. The use of a phosphate ester dispersant and a photoinitiator were necessary to achieve well-dispersed slurry with a high concentration of the particles. The amount of dispersant and photoinitiator was optimized for both the viscosity of the slurry and the polymerization reaction. *C*-axis oriented SCNN green sheets with a thickness of ~100 μm were fabricated by UV light irradiation for just 30 s after a duration of 10 - 300 s in the field of a superconducting magnet. The oriented particles in the slurry were maintained in the polymerized green bodies. The Lotgering factor *LF* was 0.81 in the green compact and increased up to 0.94 after sintering. The microstructural homogeneity could be observed in the sintered bodies after sintering the green sheets prepared by the UV curable system. Thus, the consolidation time under the magnetic field was shortened by using a fast photopolymerization reaction, and a highly particle-oriented structure was fabricated by subsequent sintering.

REFERENCES

[1] G. L. Messing, S. Trolier-McKinstry, E. M. Sabolsky, C. Duran, S. Kwon, B. Brahmaroutu, P. Park, H. Yilmaz, P. W. Rehrig, K. B. Eitel, E. Suvaci, M. Seabaugh and K. S. Oh, Solid State Mater. Sci., 29 (2004) 45-96

[2] T. Kimura, J. Ceram. Soc. Jpn., 114 (2006) 15-25

[3] T. Tani, J. Ceram. Soc. Jpn., 114 (2006) 363-370

[4] T. S. Suzuki, Y. Sakka, and K. Kitazawa, Adv. Eng. Mater., 3 (2001) 490-492

[5] A. Makiya, D. Shouji, S. Tanaka, N. Uchida, T. Kimura, and K. Uematsu, Key Eng. Mater., 206-213 (2001) 445-448

[6] W. Chen, Y. Kinemuchi, K. Watari, T. Tamura, and K. Miwa, J. Am. Ceram. Soc., 89 (2006) 2645-2648

[7] K. Tabara, A. Makiya, S. Tanaka, K. Uematsu, and Y. Doshida, J. Ceram. Soc. Jpn., 115 (2007) 237-240

[8] L. Zhang, J. Vleugels and O. V. Biest, J. Am. Ceram. Soc., 93[10] (2010) 3148-3152

[9] C. Matsunaga, T. Uchikoshi, T. S. Suzuki, Y. Sakka and M. Matsuda, Mocropor. Mesopor. Mater., 151 (2012) 188-194

[10] S. Horii, S. Okuhira, M. Yamaki, K. Kishio, J. Shimoyama and T. Doi, J. Appl. Phys., 115 (2014) 113908

[11] R. Brennan, C. Moorehead, V. Blair and K. Limmer, Mater. Manuf. Process., 33[1] (2018) 93-98

[12] T. Uchikoshi, T. S. Suzuki, H. Okuyama and Y. Sakka, J. Mater. Sci., 39 (2004) 861-865

[13] H. Kaga, Y. Kinemuchi, S. Tanaka, A. Makiya, Z. Kato, K. Uematsu, and K. Watari, J. Ceram. Soc. Jpn., 114 (2006) 10851088

[14] T. Chartier, C. Hinczewski, and S. Corbel, J. Eur. Ceram. Soc., 19 (1999) 67-74

[15] T. Chartier, R. Penarroya, C. Pagnoux, and J. F. Baumard, J. Eur. Ceram. Soc., 17,(1997) 765-771

[16] R. J. Xie, Y. Akimune, R.P. Wang, and N. Hiroaki, J. Am. Ceram. Soc., 85 (2002) 2731-2737

[17] H. Shimizu, Y. Doshida, S. Tanaka, and K. Uematsu, Jpn. J. Appl. Phys., 47 (2008) 7693-7697

[18] H. Shimizu, Y. Doshida, Y. Mizuno, S. Tanaka, K. Uematsu, and H. Tamura, Jpn. J. Appl. Phys., 51 (2012) 09LD02

[19] Y. Doshida, H. Shimizu, Y. Mizuno, K. Iron, S. Hirose, and H. Tamura, Jpn. J. Appl. Phys., 50 (2011) 09ND06

[20] T. Chartier, E. Streicher, and P. Boch, Am. Ceram. Soc. Bull., 66 (1987) 1653-1655

[21] T. Chartier, E. Jorge and P. Boch, J. Eur. Ceram. Soc., 11, (1993) 387-393
[22] K. Mikesha, and W. R. Cannon, pp. 164-83 in Forming of Ceramics, Advances in Ceramics, Vol. 9. Edited by John A. Mangels and Gary L. Messing. American Ceramics Society, Inc., Columbus, OH, 1964
[23] F. K. Lotgering, J. Inorg. Nucl. Chem., 9 (1959) 113-123
[24] T. Takahashi, Doctor thesis, Nagaoka university of technology (2013)

Chapter 3

Kinetic Analysis of Particle Rotation Behavior in Magnetic Field Using Photopolymerization Reaction

3.1 INTRODUCTION

The preparation of a concentrated slurry using a UV curable binder and the fabrication of a particle-oriented green sheet by UV irradiation in a magnetic field were described. The oriented microstructures in a green body or sheet are enhanced by sintering, as shown in Fig. 2.17. This means that a high degree of orientation is not immediately necessary in a green body or sheet, because particle orientation progresses during a sintering process. It is thus important that the degree of orientation in a green body or sheet was controlled under optimized conditions.

The theoretical dependence of the parameters was estimated for single-crystal in a magnetic field (as described in Section 1.3.2). However, the dependence of the experimental parameters on the orientation behavior of fine particles in a concentrated slurry has not yet been investigated [1]-[4]. In previous experimental studies, for sub-millimeter rod-like particles in a dilute suspension, the dependence of the magnetic flux density, particle size and viscosity of the surrounding liquid on the orientation behavior were investigated by the direct observation [5]-[10]. While such a model was suitable for validating the theory from an experimental perspective, in order to fabricate an actual oriented green body, it is necessary to propose a theory applicable to colloidal processing in a magnetic field using a high-concentrated slurry and to experimentally confirm the validity of the theory. The objective of this chapter was to elucidate the particle orientation behavior of fine particles in a concentrated slurry under a rotating magnetic field.

3.2 THEORY

The theory of the orientation behavior of the particles in the highly concentrated slurry can be extended from the theory of the orientation of a single particle. As mentioned in Chapter 1, in the single-particle orientation theory, the intrinsic magnetic response rate τ^{-1} was derived using the magnetic torque $\boldsymbol{M}$ and hydrodynamic torque $\boldsymbol{N}$ applied to the particles.

$$\tau^{-1} = \frac{1}{12\mu_0\eta}\Delta\chi B^2 \qquad (3.1)$$

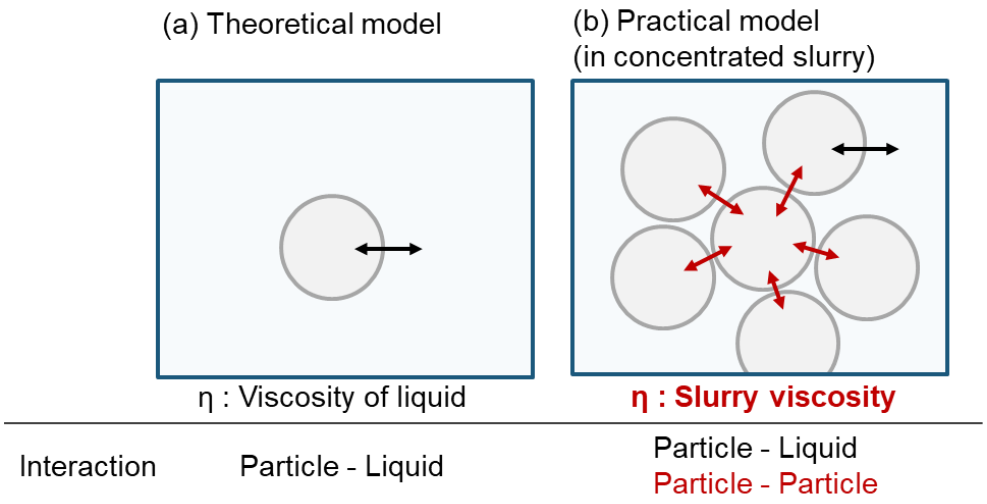

FIGURE 3.1 Schematic view of (a) theoretical model (a spherical particle floating in a liquid) and (b) practical model (spherical particles in the concentrated slurry).

Here, it is considered the interaction between the particles in a high concentrated slurry as shown in Fig. 3.1. A particle in the slurry is surrounded by other particles. Therefore, it is assumed that the viscosity is not the viscosity of the surrounding liquid in the equation but the zero shear viscosity of the slurry (i.e., shear viscosity when the shear stress is almost zero). The time for orientation is the same as Eq. (1.16), as follows,

$$t = -\tau \ln \frac{\tan \theta}{\tan \theta_0} \qquad (3.2)$$

The intrinsic magnetic response rate of a particle τ^{-1} and the orientation time t depend on the inverse of the viscosity of the surrounding liquid and on the square of the magnetic flux density ηB^{-2}.

Figure 3.2 shows τ^{-1} and t calculated by Eqs. (3.1) and (3.2) with the anisotropy of the diamagnetic susceptibility $\Delta\chi$ (1.0×10^{-6}, 5.0×10^{-7}, 1.0×10^{-7}). For the boundary conditions, the particle direction θ_0 is assumed to be 45° as the average value at $t = 0$ and the oriented direction of the particle θ is 5° at $t = t$. As shown in Fig. 3.1, it is expected that the intrinsic magnetic response rate of a particle τ^{-1} is inversely proportional to ηB^{-2}, and the orientation time t is proportional to ηB^{-2}.

In this study, the influences of the magnetic flux density, viscosity of the slurry and processing time in the rotating magnetic field on the degree of orientation in the green sheets were examined. In principle, the viscosity described in the model equations is that of the liquid around a given particle. However, a particle in the slurry is surrounded by several particles in a concentrated slurry as shown in Fig. 3.1. The motion of the particle is influenced by both surrounding liquid and particles. Therefore, the zero shear viscosity

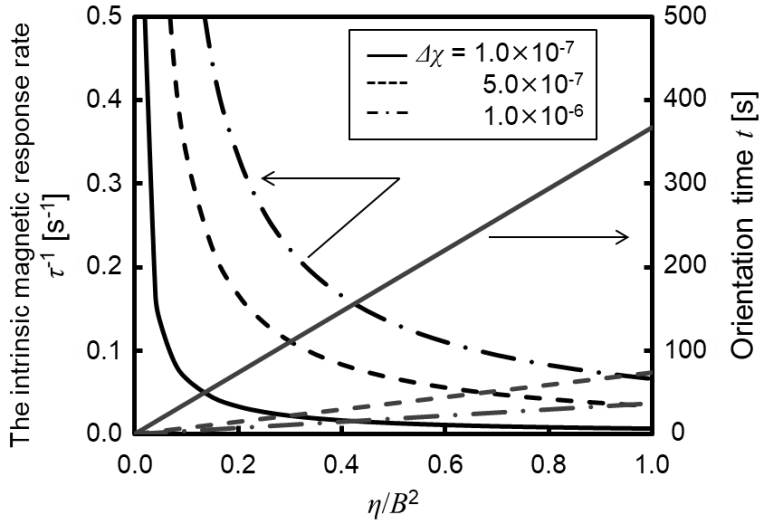

FIGURE 3.2 The intrinsic magnetic response rate τ^{-1} and the orientation time t of a particle calculated by Eqs. (3.1) and (3.2) plotted against the viscosity divided by the square magnetic flux density.

of the slurry was used. The viscosity of a slurry decreases with increasing temperature; hence, the orientation behavior can be investigated by changing the temperature of the slurry. Furthermore, the effect of the concentration of the solid contents in the slurry on the orientation behavior was also investigated.

3.3 EXPERIMENTAL PROCEDURE

3.3.1 Slurry Preparation and Characterization

Raw powders used in this chapter were synthesized and deagglomerated by the same method described in Section 2.2.1. The morphology of the deagglomerated powders was examined by scanning electron microscopy (SEM, JSM-5310LVB, JEOL, Tokyo, Japan). The particle size distribution was determined by the sedimentation method (Sedigraph 5100, Micrometrics, USA). The powder was dispersed in deionized water with sodium hexametaphosphate as the dispersing agent.

The slurry for forming the green sheets was prepared similarly to the one described in Section 2.2.2. A UV-curable resin was used as the dispersion medium and contained polyether acrylate monomer diluted in hydroxyethyl methacrylate with 2 wt% of the photoinitiator 2-hydroxy-2-methyl-1-phenylpropan-1-one. A phosphate ester with 1.2 wt% was used as the dispersant. The solid concentration of the SCNN powder in the slurry was varied in the range from 20 to 45 vol%.

The viscosities of the binder mixture and the slurry were measured by a rheometer (Physica MCR301, Anton Paar, Austria) using a cone and plate apparatus (CP25-2) in the stress-controlled mode. The shear rate was varied from 0.001 s^{-1} to 100 s^{-1}. The measurement temperature was set to 20-50 °C. The viscosity behavior was characterized by fitting with the Cross model as following: [11]

$$\eta = \eta_\infty + \left(\frac{\eta_0 - \eta_\infty}{1+\alpha D^n}\right) \qquad (3.3)$$

where D is the shear rate, η_0 is the viscosity at zero shear rate, η_∞ is the viscosity at an infinite shear rate, and α and n are fitting parameters. The values of η_0, α, and n were estimated by fitting the viscosity curves with Eq. (3.3) using the nonlinear least-squares method.

3.3.2 Fabrication and Characterization of Green Sheets

The green sheets were fabricated in an almost similar method as described in Section 2.2.4. The temperature of slurry was kept in a thermostatic bath at 20 - 50 °C for 1 h before it was cast on a PET sheet. The cast slurry was placed on a rotation stage within a horizontal magnetic field of 0 - 10 T induced by a superconducting magnet (TM-10VH10, TOSHIBA Co. Japan). The stage was set at a temperature between 20 and 50 °C and rotated horizontally in the magnetic field. The rotation speed was 30 rpm. The exposure time was varied from 1 to 300 s. Then, the green sheet was fabricated by applying UV rays emitted from a lamp set above the cast sheet for 30 s, i.e., E = 10.8 J/cm^2, as shown in Fig. 3.3. For comparison with a randomly oriented green sheet, samples were also fabricated by irradiating UV rays outside of the magnetic field. The sheet thickness after polymerization was measured to be approximately 0.10 mm. After exposure, the liquid non-polymerized areas were removed using ethanol.

The crystal orientations of the surfaces of the green sheets were evaluated using X-ray diffraction (XRD, Ultima IV, RIGAKU Japan) with Cu Kα_1 radiation for a 2θ range of 20 - 70 °. The degree of c-axis orientation was readily evaluated in terms of the Lotgering factor, LF, of the [00l] orientation, as described in Subsection 2.2.4.

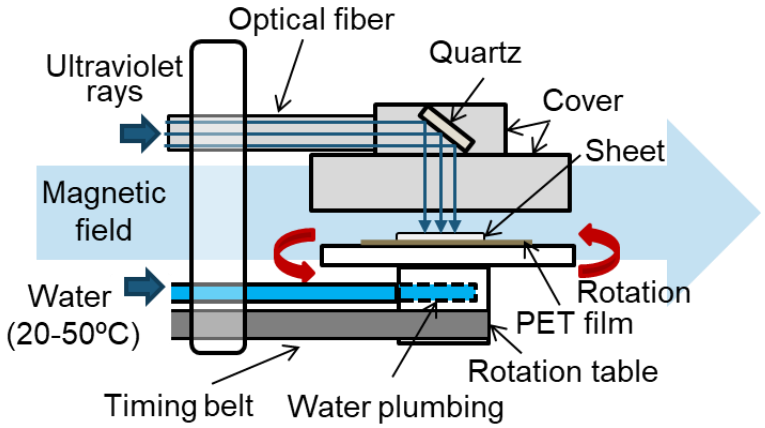

FIGURE 3.3 Schematic illustrations of experimental setting. Rotation apparatus and quartz fiber in the unidirectional strong magnetic field of a superconducting magnet.

Rocking curves of the 002 reflections for some samples were also measured in order to confirm the orientation distribution and to relate the *LF* value with the degree of orientation. The measurement conditions of the rocking curves include a step angle of 0.02 ° at a step speed of 1 ° min^{-1}. The multiple of a random distribution (MRD) was calculated by a measured rocking curve of the oriented sample divided by that of the random sample at the same angle θ. The MRD was characterized by fitting with the March–Dollase function containing a texture volume fraction *f* as follows: [12,13]

$$P_{(f,r,\theta)} = f\{r^2 cos^2\theta + r^{-1} sin^2\theta\}^{-3/2} + (1 - f) \qquad (3.4)$$

where *r* is a parameter that quantifies the alignment quality. Small *r* indicates a narrow distribution of particle orientations; *r* is 1 for a random structure and tends to 0 for a perfectly oriented structure [12]. Fitting the MRD with Eq. (3.4), the parameters *f* and *r* were calculated using the nonlinear least-squares method.

3.4 RESULTS AND DISCUSSION

3.4.1 SCNN Powder and Slurry

Figure 3.4 shows an SEM image of the deagglomerated SCNN particles. As seen, the particles have irregular shapes; in particular, large particles have tabular shapes. Figure 3.5 shows the particle size distribution of the deagglomerated powder measured by the sedimentation method, where the particle size is shown to vary from 0.1 to 2.5 μm. The median particle size, D_{50}, was 0.85 μm. The results show that the particles used in this investigation are typical to those used in industrial ceramics.

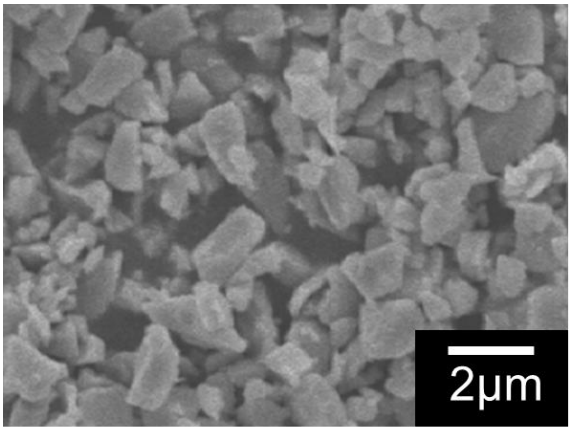

FIGURE 3.4 Particle morphology of deagglomerated powders (D_{50} = 0.85 μm).

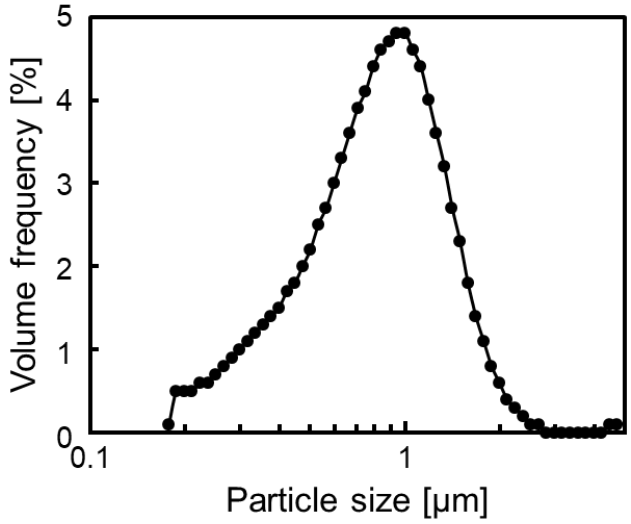

FIGURE 3.5 Particle size distribution of deagglomerated SCNN particles.

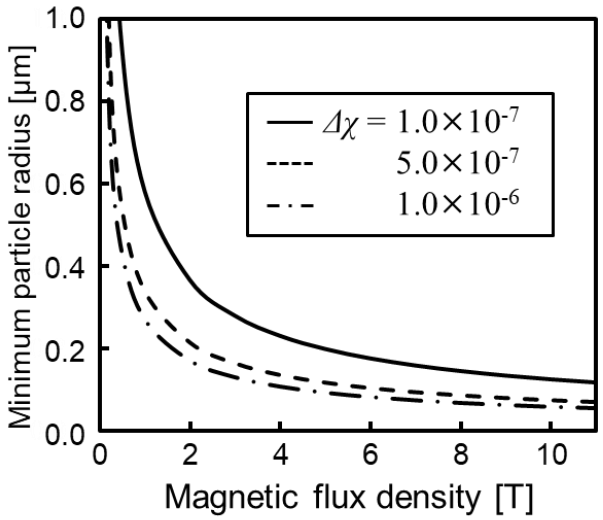

FIGURE 3.6 Minimum particle sizes required for the orientation of particles plotted against the magnetic flux density.

Here, it is estimated the particle size limit for orientation in a magnetic field in terms of balancing the particle magnetic energy and the thermal energy k_BT [14]. The estimated minimum particle size d_{min} can be expressed as follows:

$$d_{min} = (12\mu_0 k_B T/\Delta\chi\pi B^2)^{1/3} \quad (3.5)$$

where k_B is Boltzmann's constant and T is the absolute temperature. Figure 3.6 shows the minimum particle sizes for the orientation of particles at a temperature of 293 K in terms of the anisotropy of the diamagnetic susceptibility $\Delta\chi$ (1.0×10^{-6}, 5.0×10^{-7}, 1.0×10^{-7}) and the magnetic flux density B (0 - 10 T). It is found that d_{min} = 0.09 μm at T = 293 K, $\Delta\chi = 5.0 \times 10^{-7}$, and B = 10 T, and that a magnetic field of 4 T is enough to orient almost all particles if $\Delta\chi = 5.0 \times 10^{-7}$.

Figure 3.7 shows a viscosity of liquid medium consisting of UV curable resin, dispersant, and photoinitiator at each temperature in the range of 20 - 50 °C. The binder viscosity decreased dramatically with the increase in temperature. Figure 3.8 shows the viscosity curves of slurries with a solid content of 45 vol% at each temperature between 20 and 50 °C. The slurry viscosity decreased considerably with increasing temperature, consistent with the behavior of the solvent. The viscosity decreased abruptly with increasing shear rate. The solid lines are the curves fitted with the Cross model represented in Eq. (3.3). The values of η_0, α, and n at each temperature determined by fitting with the Cross model are shown in Table 3.1. The parameter n is in the range of 0.77 - 0.80 for all slurries and indicates the shear-thinning behavior of the slurry. For the highly concentrated slurry, high shear viscosity at a low shear rate is caused by interactions among the particles and weakening of such interactions as a result of the applied shear caused the shear-thinning behavior.

Figure 3.9 shows the viscosity curves of the slurries with solid concentrations of 20 - 45 vol% at the temperature of 20 °C. The viscosity of the slurries increased with increasing solid contents. Newtonian behavior was observed for the slurry with solid contents smaller than 40 vol%. The fitted curves using Eq. (3.3) are also shown as solid lines in Fig. 3.9. Table 3.2 shows the values of η_0, α, and n for the slurry with varied powder concentration. The values of η_0 was dramatically raised between 40 vol% and 45 vol% solid contents in the slurry. Those results obviously indicate that the viscosity depends on the solid contents in the slurry as well as the viscosity of the liquid medium.

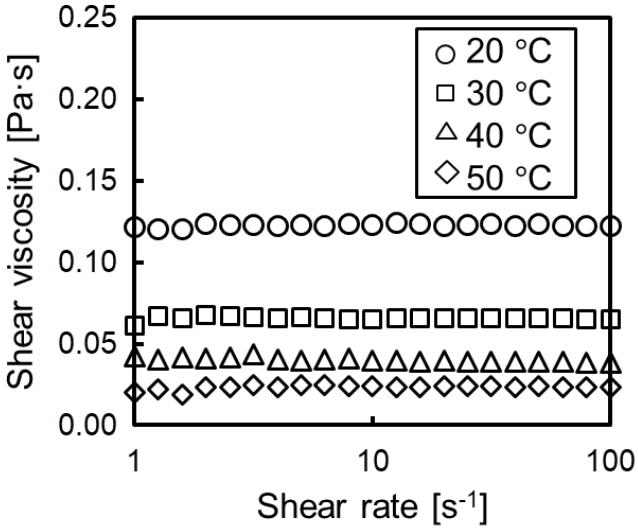

FIGURE 3.7 Shear viscosity of liquid medium consisting of UV curable resin, dispersant, and photoinitiator at each temperature.

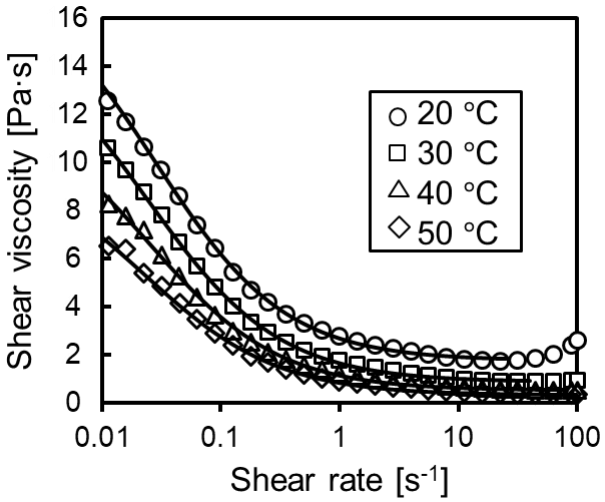

FIGURE 3.8 Shear viscosity of a slurry consisting of 45vol% SCNN powder, UV curable resin, dispersant, and photoinitiator at each temperature. The solid lines are the fitted curves with Cross model Eq. (3.3).

TABLE 3.1 Parameters for the Cross model of a slurry consisting of 45 vol% powder.

Temperature of slurry [°C]	η_∞ [Pa・s]	η_0 [Pa・s]	α	n
20	1.77	18.3	17.0	0.791
30	0.903	16.0	18.5	0.783
40	0.537	12.7	18.7	0.795
50	0.356	10.4	18.6	0.770

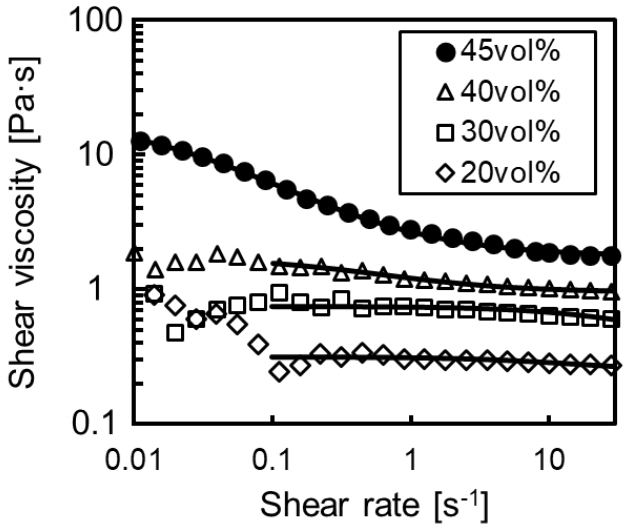

FIGURE 3.9 Shear viscosity of a slurry SCNN powder, UV curable resin, dispersant, and photoinitiator at 20 ºC. The solid contents are varied between 20 and 45 vol%. The solid lines are the fitted curves with Cross model Eq. (3.3).

TABLE 3.2 Parameters for the Cross model of slurries at 20 ºC.

Solid volume fraction [vol%]	η_∞ [Pa・s]	η_0 [Pa・s]	α	n
20	0.245	0.316	0.0697	1.00
30	0.395	0.756	0.0252	1.00
40	0.960	1.72	2.01	0.858
45	1.77	18.3	17.1	0.787

Here, the inter-particle surface distance was calculated as a function of solid concentration in the slurry by Woodcock's equation [15],

$$H = D\left\{\left(\frac{1}{3\pi F}+\frac{5}{6}\right)^{0.5}-1\right\} \qquad (3.6)$$

where H is the inter-particle surface distance, D is the particle diameters and F is the solid volume fraction in the slurry. Figure 3.10 shows that the mean inter-particle surface distance decreased with an increase in the concentration of solid. Please note the logarithm scale in the vertical axis. The thicker the concentration of slurry is the shorter the inter-particle distance becomes. In particular, the inter-particle distance decreases in the slurry with solid contents of > 45 vol%. This strongly affects the packing structure of the particles in the slurry.

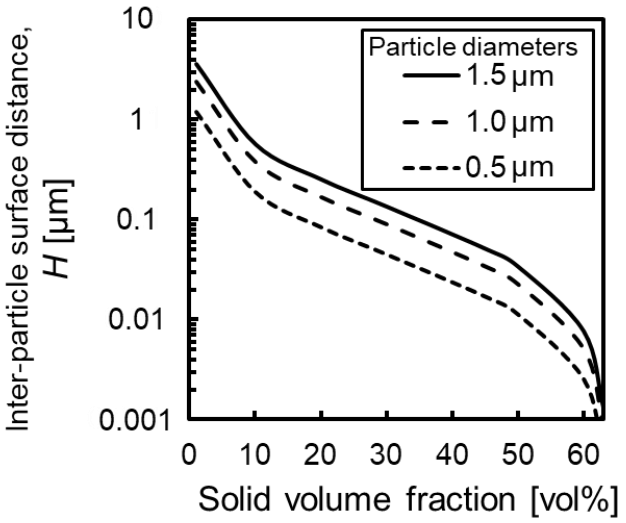

FIGURE 3.10 Change of mean inter-particle surface distance as a function of volume fraction of solid contents and particle diameters in a slurry.

3.4.2 Orientation of Consolidated Green Sheets

Figure 3.11 shows XRD patterns of the polymerized green sheets with 45 vol% solids prepared with processing times of 1 s and 10 s with and without the application of a magnetic field. For all samples fabricated with a magnetic field, the intensity of the *c*-planes (i.e., 001 and 002) was enhanced relative to that of the samples fabricated without the magnetic field. The longer the sample was exposed to the magnetic field before consolidation with UV irradiation, the higher the intensities of the *c*-plane peaks. The *LF* of the oriented samples increased gradually with increasing processing time under the magnetic field.

The rocking curves MRD of the 002 peak for these samples are shown as points in Fig. 3.12. The solid curves fitted by Eq. (3.4) are also shown. The peak intensity increased with increasing processing time and its full-width at half-maximum (FWHM) was less than 10 °, indicating that the oriented distribution was narrow. Table 3.3 shows the *LF*, FWHM, the *r* parameter, and the textured fraction *f* for these samples. The *r* parameter decreased, and the textured fraction *f* increased as the processing time increased. This relationship between *r* and *f* shows that particle orientation varies with the textured fraction.

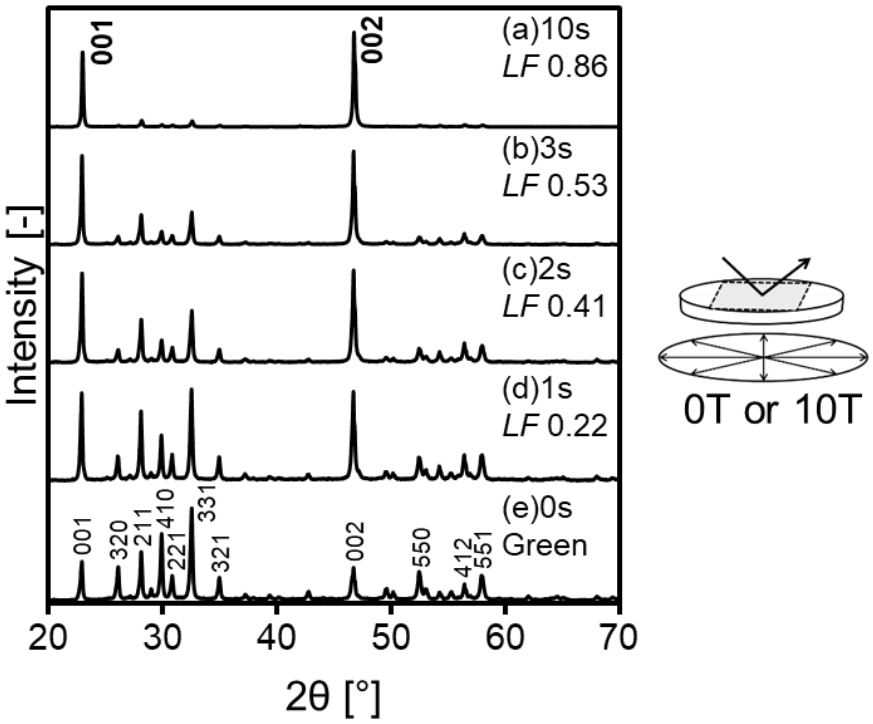

FIGURE 3.11 X-ray diffraction patterns obtained from green sheets with a solid concentration of 45vol% for various durations of (a) 10 s, (b) 3 s, (c) 2 s and (d) 1 s (a, b, c and d) with and (e) without a 10 T rotating magnetic field at 20 °C.

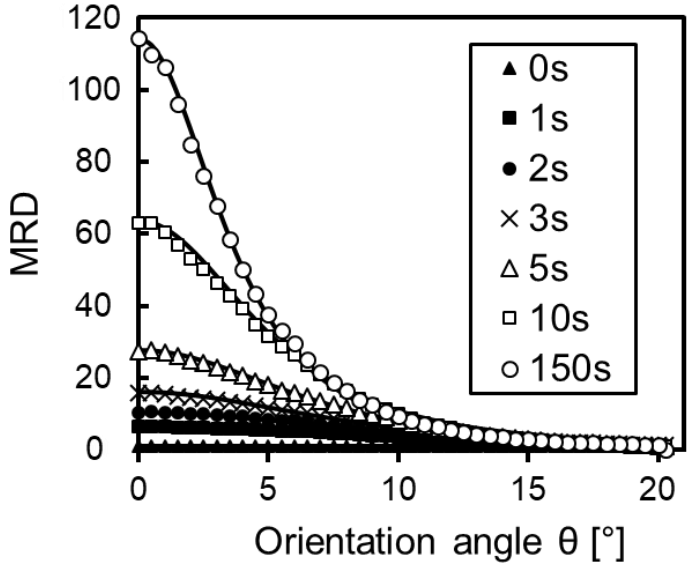

FIGURE 3.12 Rocking curves, MRD of particle oriented SCNN samples with a solid concentration of 45 vol% for various durations with a 10 T rotating magnetic field at 20 °C. The solid lines are fitted curves with March-Dollase function Eq. (3.4).

TABLE 3.3 Full-width at half-maximum (FWHM), Lotgering factor (*LF*), orientation parameter *r* and textured fraction *f* for each processing time

Processing time[s]	*LF*	FWHM[°]	Orientation parameter (*r*)	Textured fraction (*f*)
1	0.22	15.4	0.349	0.248
2	0.41	14.8	0.350	0.423
3	0.53	13.1	0.312	0.474
5	0.65	110	0.282	0.614
10	0.86	9.00	0.236	0.836
150	0.95	6.92	0.201	0.931

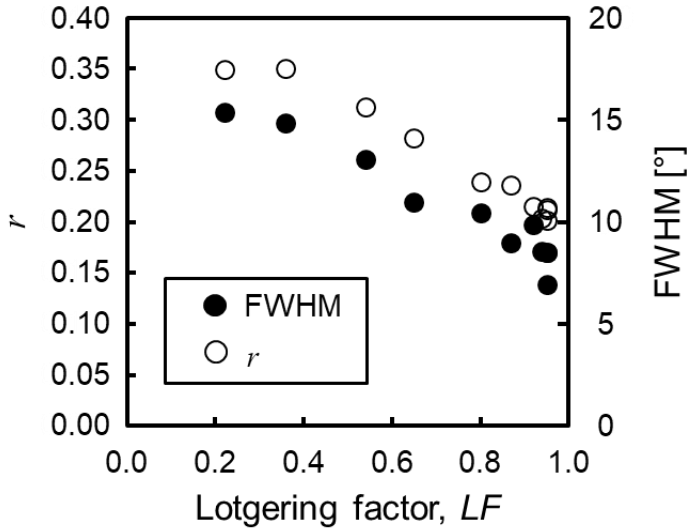

FIGURE 3.13 The correlation between *LF* calculated from the X-ray diffraction (XRD) pattern and parameters *r* determined by fitting March-Dollase function to the MRD, and the full width at half maximum (FWHM) of the rocking curves in particle-oriented SCNN sheets with a solid concentration of 45 vol%.

Figure 3.13 shows the correlation of *LF* versus the FWHM of the rocking curves and the *r* parameters. It is observed that *LF* is distributed throughout the range of 0.2 to 0.9, whereas the FWHM and *r* are distributed in a narrow range. Therefore, FWHM and *r* are sensitive to higher orientation. An important aspect of these data is the linear correlation between the *LF* range of 0.2 - 0.9 and the FWHM and parameter *r*. Although *LF* is a physically ambiguous parameter, this correlation indicates that it is nevertheless suitable to quantitatively evaluate the degree of SCNN orientation [16]. Furthermore, bearing in mind the development of the orientation structure in a green body or sheet during sintering, as shown in Fig. 2.17, the degree of orientation in the green bodes or sheets is suitable in the *LF* range of 0.3 - 0.6.

3.4.3 Time Dependence of Particle Orientation in Rotating Magnetic Field

3.4.3.1 Effect of Magnetic Flux Density and Slurry Viscosity

Figure 3.14 (a) shows the relationship between the exposure time of the samples in the magnetic field and the degree of orientation, *LF*, of the green sheets prepared under various magnetic flux densities (0 - 10 T). Solid concentration in the slurry was 45 vol%. It is clear that the degree of orientation depends on the duration of exposure to the magnetic field. The saturation values increased with increasing magnetic flux density. The degree of orientation of slurries exposed to 8 and 10 T showed saturation, even after a short exposure time, while the degree of orientation was extremely high (~0.95). Meanwhile, for the green sheets made from slurries exposed to magnetic flux densities of 2 - 6 T, the degree of orientation gradually increased with exposure time. Thus, the time required for saturation of the degree of orientation decreased with increasing the magnetic flux density. In other words, the time required for orienting the particles in a concentrated slurry decreases with increasing magnetic flux density.

Figure 3.14 (b) shows the relationship between the exposure time of the sample in the magnetic field of 6 T and the degree of orientation of the green sheets prepared from the slurry with a solid concentration of 45 vol% at various temperatures. As seen, the degree of orientation depended on the exposure time to the magnetic field, and the degree of orientation of the green sheets was affected by the viscosity of the slurries. The saturation values decreased with decreased temperature (i.e., increased viscosity). The degree of orientation of the slurries at 40 and 50 °C showed saturation, even after a short exposure time, and the degree of orientation was high (~0.85). By comparison, for the green sheets made from slurries at 20 °C or 30 °C, the orientation time was two to three times that at 50 °C. The time required to orient the particles in a concentrated slurry at 40 and 50 °C became short. This shows that the time required for orienting the particle in a concentrated slurry decreased with decreasing slurry viscosity.

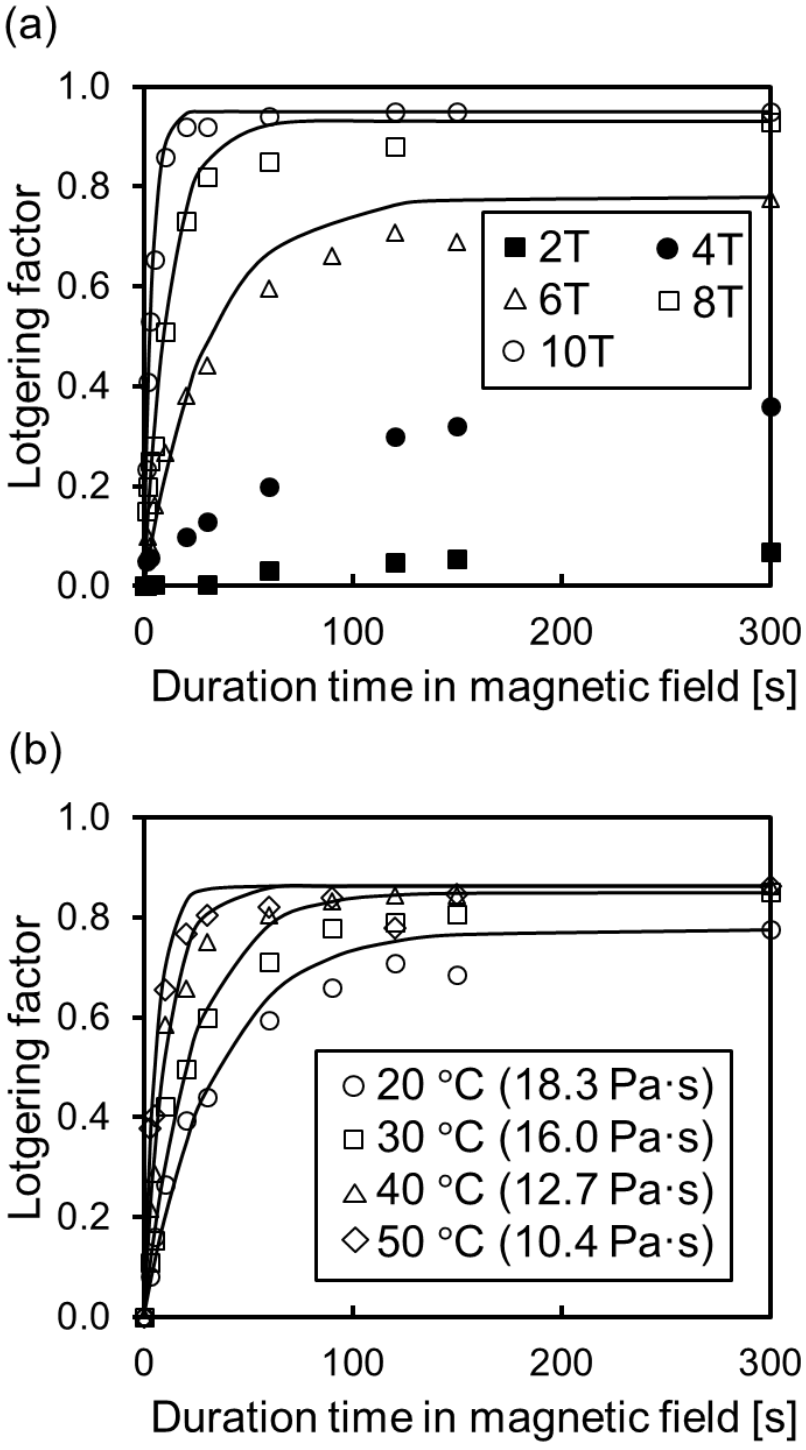

FIGURE 3.14 The orientation degree of prepared by various duration times in rotating magnetic field (a) of each magnetic flux density at 20 ℃ and (b) of 6 T at each temperature, solid lines are fitted curves by using Eq. (3.7). The solid concentration in the slurry is 45 vol%.

Let consider the effect of the magnetic flux density and slurry viscosity on the intrinsic magnetic response rate τ^{-1} and the orientation time t, which, according to Eqs. (3.1) and (3.2), may depend on ηB^{-2} as shown in Fig. 3.2. Regarding Fig. 3.14 and Eq. (3.1), the intrinsic magnetic response rate τ^{-1} can be calculated by fitting the data in Fig. 3.14 with the following function:

$$LF_{(t)} = LF_{max}\left\{1 - exp\left(-\frac{t}{\tau}\right)\right\} \qquad (3.7)$$

where LF_{max} is assumed to be the maximum LF value for each condition. If the particle size satisfies Eq. (3.5), LF_{max} is 1. However, in practice, experimental values of LF cannot achieve 1 due to agglomeration, even in a strong magnetic field of 10 T. The intrinsic magnetic response rate τ^{-1} for each condition was calculated using the nonlinear least-squares method. The fitted curves using Eq. (3.7) are shown as solid lines in Fig. 3.14. Here, regarding the condition of magnetic flux density 2 and 4 T, these results are not contained in the calculation due to lower orientation.

Figure 3.15 shows the intrinsic magnetic response rate τ^{-1} plotted against the slurry viscosity divided by the square of the magnetic flux density. Here, the viscosity at zero shear rate η_0 estimated from the experimental data shown in Table 3.1 was used as the viscosity value η in the horizontal axis. The fitted curve with Eq. (3.1) is shown in Fig. 3.15. Thus, the result shows that the experimental values of τ^{-1} depend on both the viscosity and the inverse of the magnetic flux density squared. Furthermore, the anisotropy of the diamagnetic susceptibility of SCNN, $\Delta\chi$ can be estimated to be 5.5×10^{-7}.

Figure 3.16 shows the orientation time t plotted against the slurry viscosity divided by the magnetic flux density squared ηB^{-2}. The orientation time t was obtained by Eq. (3.2) using experimental values of τ^{-1}. The solid line is the line calculated by Eq. (3.2) with $\Delta\chi$ of 5.5×10^{-7}. As shown in Fig. 3.16, the orientation time t is proportional to ηB^{-2}. Thus, it is demonstrated that the intrinsic magnetic response rate and orientation time can be estimated accurately from slurry viscosity and magnetic flux density. However, when the ηB^{-2} value is larger than 0.4, that is, at low magnetic flux density and high slurry viscosity, the experimental data of τ^{-1} and t differ slightly from those calculated using Eqs. (3.1) and (3.2).

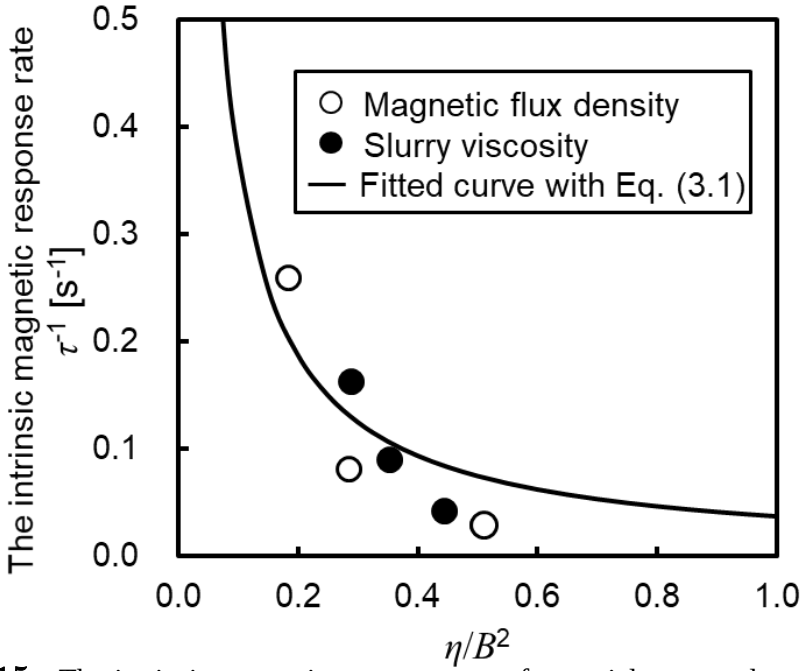

FIGURE 3.15 The intrinsic magnetic response rate of a particle exposed to the rotating field plotted to the viscosity of slurry divided by the square magnetic flux density. The solid contents in the slurry is only 45 vol%. The solid line is a fitted curve using Eq. (3.1).

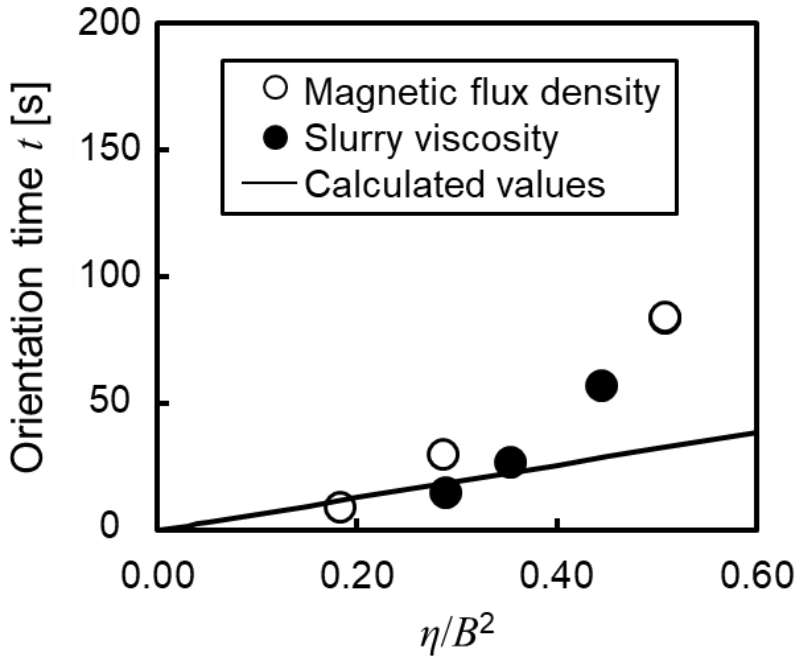

FIGURE 3.16 Time required for particle orientation calculated with Eq. (3.2) plotted against the viscosity of slurry divided by the square magnetic flux density. The solid contents in the slurry is only 45 vol%. Solid line is a calculated line by using Eqs. (3.1) and (3.2).

3.4.3.2 Effect of Solid Concentration in Slurry

Figure 3.17 shows the dependence of the concentrations of slurry and the exposure time in the magnetic field on the degree of orientation of the green sheets for each magnetic flux density (0 - 10 T). The temperature of slurries was at 20 °C. Here, it is necessary to note that a range of the horizontal axis differs for each magnetic field. The orientation degree of the green sheets was clearly influenced by the solid concentration in the slurry. As similar to Fig. 3.14, the degree of orientation of slurries exposed to the magnetic field of 6, 8 and 10 T showed saturation, as shown in Figs. 3.17 (a), (b), and (c). Particularly, in 10 T, the time for saturation was 2 s for the sample prepared from 20 vol% slurry.

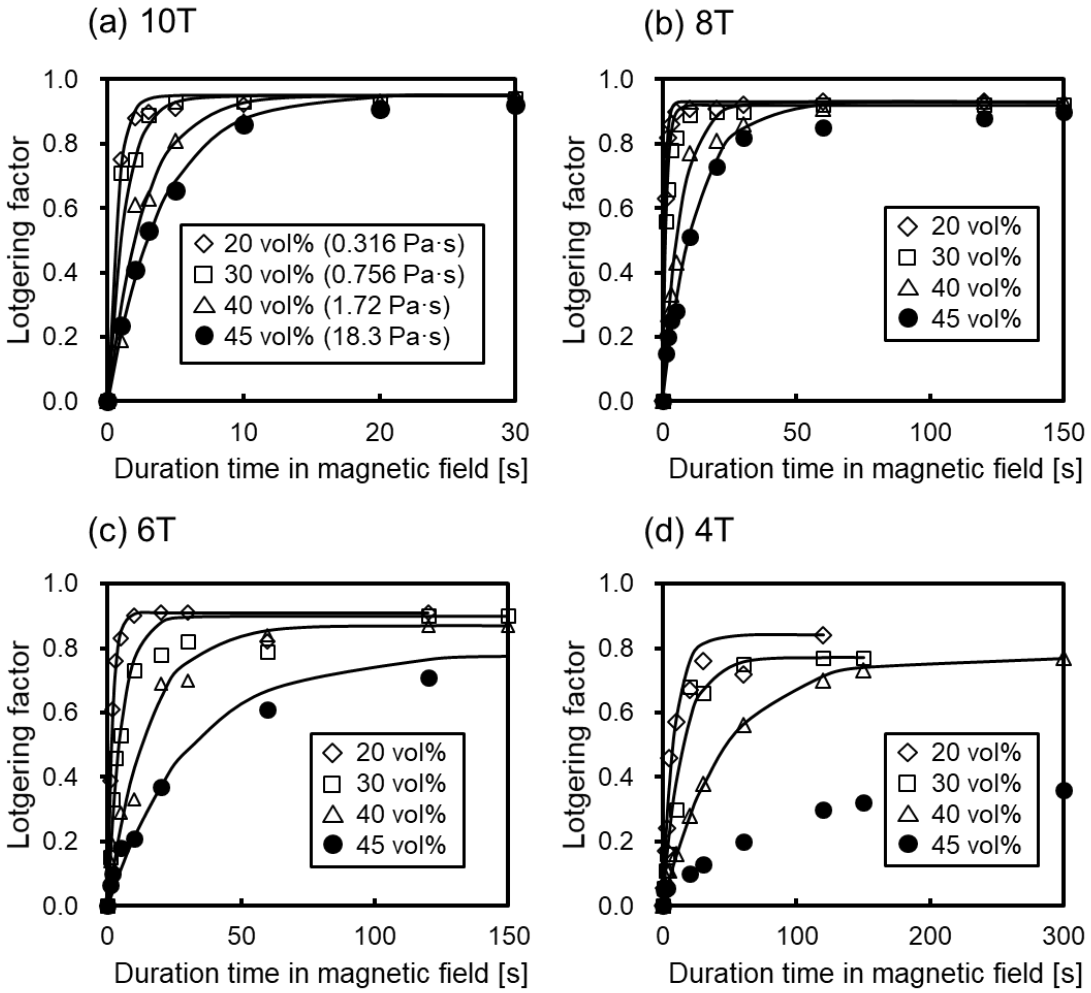

FIGURE 3.17 The orientation degree of green sheets with each solid concentration for various duration times in rotating magnetic field at 20 °C, solid lines are fitted curves by using Eq. (3.7). The applied magnetic flux density is (a) 10 T, (b) 8 T, (c) 6 T and (d) 4 T, respectively.

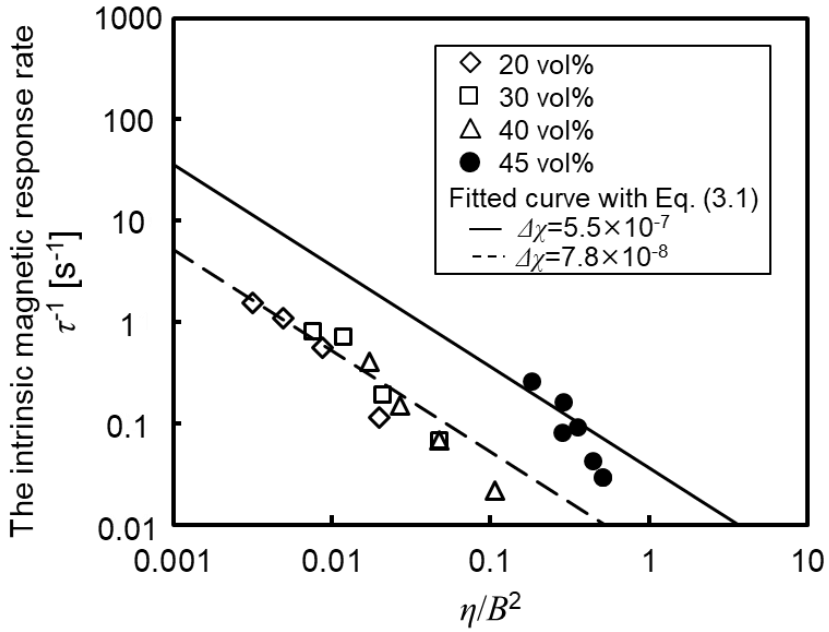

FIGURE 3.18 The intrinsic magnetic response rate of a particle exposed to the rotating field plotted to the viscosity of slurry divided by the square magnetic flux density. Lines are fitted curves using Eq. (3.1).

Meanwhile, for the green sheets prepared from slurries exposed to magnetic flux densities of 4 T (Figure 3.17 (d)), the saturation values decreased down to *LF* of 0.7 with increasing the solid concentration in the slurry. The time for particle orientation depends on the solid concentration in the slurry and will increase as the solid content in the slurry increases. In particular, when the magnetic flux density is low, the orientation time becomes significantly longer when the solid content in the slurry increases.

Let consider the influence of the solid concentration in the slurry on the intrinsic magnetic response rate τ^{-1} and the orientation time *t*. Similar to Section 3.2.3.1, the intrinsic magnetic response rate τ^{-1} can be calculated by fitting the data in Fig. 3.17 with Eq. (3.7). The τ^{-1} for each condition was calculated using the nonlinear least-squares method. The fitted curves using Eq. (3.7) are shown as solid lines in Fig. 3.17. Here, the condition of the slurry of the solid content of 45 vol% exposed under the magnetic flux density of 4 T is not included in the calculation. This is due to the low degree of saturated orientation.

Figure 3.18 shows the intrinsic magnetic response rate τ^{-1} plotted against the slurry viscosity divided by the square of the magnetic flux density. Note that both axes are on a log scale. The viscosity at zero shear rate η_0 estimated from the experimental data as shown in Table 3.2 was used as the viscosity η. The results indicate that the experimental values of τ^{-1} depend on both the viscosity and the inverse of the magnetic flux density

squared, even if the solid concentration in the slurry is reduced. However, it also shows that the particle rotation behavior in each slurry with a solid concentration of 20 to 40 vol% is different from that of 45 vol%. The cause might be related to the distribution of particles in the slurry.

The difference in the distribution of particles is observed as the shape of the viscosity curve of the slurry. The viscosity curve of each slurry with a solid concentration of 20 to 40 vol% showed Newtonian behavior, whereas that of a 45vol% slurry showed shear-thinning behavior (in Figure 3.9).

As shown in Fig. 3.15, approximated curves of the experimental values of τ^{-1} are calculated by Eq. (3.1) using the nonlinear least-squares method. The fitted curves are shown in Fig. 3.18. Here, the experimental data were divided into two groups. The solid line is the fitted line for the experimental τ^{-1} values of the particles in the 45 vol% slurry, and the dotted line is the fitted line for the τ^{-1} of the particles in the 20 - 40 vol% slurries. Interestingly, the apparent diamagnetic susceptibility anisotropy of SCNN particles in slurries at each solid concentration of 20 to 40 vol% is estimated to be 7.8×10^{-8}, which is about one-seventh of that of 45 vol% slurry. However, the anisotropy of the diamagnetic susceptibility is naturally the value of specific to the material and dese not decrease. This is probably due to another factor that has the same effect as reducing the diamagnetic susceptibility anisotropy.

Here, I consider the reason why the apparent susceptibility anisotropy was underestimated. As shown in Fig. 3.9, the slurry with low solid concentration showed Newtonian behavior. As shown in Fig. 3.10, the mean inter-particle surface distance in the slurry, which calculated with the Woodcock model, increases with decreasing the solid concentration. These indicate that each particle can move freely in the slurry. Therefore, it is assumed that the effective volume of one particle in the slurry acts twice as large as the actual particle size due to the Brownian motion of particles, as shown Fig. 3.19. However, since the actual particle portion remains the same, the magnetic torque $\boldsymbol{M}'$ subjected to particles becomes to be one-eighth as small as the $\boldsymbol{M}$ derived from the theoretical model.

$$\boldsymbol{M}' = \frac{1}{8} \times \frac{V\Delta\chi}{\mu_0} (\boldsymbol{n} \cdot \boldsymbol{B})(\boldsymbol{n} \times \boldsymbol{B}) \qquad (3.8)$$

Namely, the revised intrinsic magnetic response rate $(\tau^{1})'$ is given by:

$$(\tau^{-1})' = \frac{1}{8} \times \frac{1}{12\mu_0\eta} \Delta\chi B^2 \qquad (3.9)$$

The orientation time t was obtained by Eq. (3.2) by using experimental values of τ^{-1}. The solid and dotted lines are the lines calculated by Eqs. (3.1), (3.2) and (3.9) with $\Delta\chi$ of

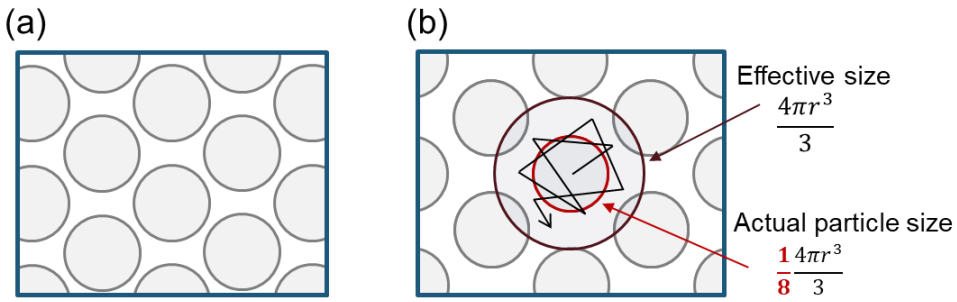

FIGURE 3.19 Schematic view of the spherical particles (a) in the high concentrated slurry and (b) in the low concentrated slurry.

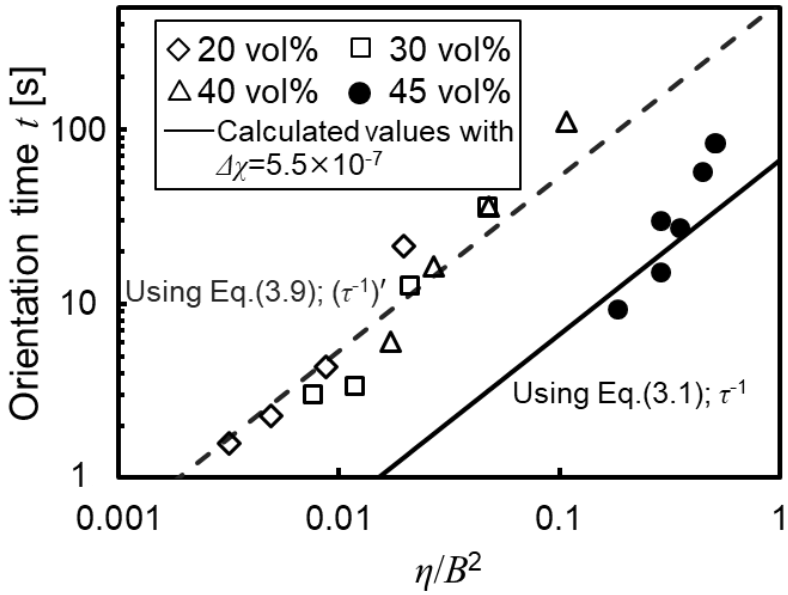

FIGURE 3.20 Time required for particle orientation calculated with Eq. (3.2) plotted against the viscosity of slurry divided by the square magnetic flux density. Lines are calculated lines by using Eqs. (3.1), (3.2) and (3.9).

5.5×10^{-7}. As shown in Fig. 3.19, the orientation time is proportional to ηB^{-2}. Thus, the intrinsic magnetic response rate and the orientation time depend not only on slurry viscosity and magnetic flux density but on solid contents in the slurry.

The experimental results also showed that the value of ηB^{-2} deviated from the straight line at a high value. At high ηB^{-2}, i.e., high viscosity at low magnetic fields, it takes a considerable amount of time to complete particle orientation. These include factors that are not considered in theory, such as gravity, particle interactions, and convection in the slurry. Furthermore, in the low magnetic field as low as 4 T, the value of the diamagnetic susceptibility of the material used in this study is very small, and it is difficult to align small particles in one direction.

3.5 CONCLUSIONS

The particle orientation behavior during colloidal processing in a magnetic field was examined experimentally. An increase in the magnetic flux density and a decrease in the viscosity of the slurry led to a significant decrease in orientation time. The intrinsic magnetic response rate of a particle τ^{-1} was inversely proportional to ηB^{-2}, and the orientation time t was proportional to ηB^{-2}. For the rotation of particles in the 45 vol% slurry in the magnetic field, the orientation time calculated using the model equations was the same order as the experimental data. This indicates that the orientation behavior was explained by the applied theory. A particle in a slurry with a high solid content is affected by both the surrounding liquid and the neighboring particles. While the particle rotation behavior in each slurry with a solid concentration of 20 to 40 vol% is different from that of 45 vol%. When the solid concentration of the slurry is 20 - 40 vol%, the orientation time estimated from the experimental data took a long time as compared with that calculated using the applied theoretical equations. The result suggests that the distribution of particles in the slurry also influences particle rotation in the magnetic field.

REFERENCES

[1] T. Kimura and M. Yoshino, Langmuir, 21 (2005) 4805-4808
[2] T. Kimura, M. Yamato, W. Koshimizu, M. Koike and T. Kawai, Langmuir, 16 (2000) 858-861
[3] T. Kimura, M. Yoshino, T. Yamane, M. Yamato, M. Tobita, Langmuir, 20 (2004) 5669-5672
[4] T. Kimura, Jpn. J. Appl. Phys., 48 (2009) 020217
[5] J. Akiyama, H. Asano, K. Iwai and S. Asai, J. Japan Inst. Metals, 71[1] (2007) 108-112 [in Japanese]
[6] N. Hirota, T. Ando, T. Shimada, H. Wada and Y. Sakka, Sci. Technol. Adv. Mater., 9 (2008) 024211
[7] K. Iwai, M. Niimi and T. Kohama, Jpn. J. Appl. Phys., 48 (2009) 106503
[8] K. Iwai, Jpn. J. Appl. Phys., 49 (2010) 125602
[9] S. Tsukui and T. Kimura, Jpn. J. Appl. Phys., 51 (2012) 057301
[10] H. Song, M. Tan, T. W. Walker, A. Jander and P. Dhagat, IEEE Trans. Magn., 51[11] 2015 2802105
[11] M. M. Cross, J. Colloid Sci., 20 (1965) 417-437
[12] W. A. Dollase, J. Appl. Cryst., 19 (1986) 267-272
[13] M. M. Seabaugh, M. D. Vaudin, J. P. Cline and G. L. Messing, J. Am. Ceram. Soc., 83[8] (2000) 2049-2054
[14] P. De Rango, M. Lees, P. Lejay, A. Sulpice, R. Tournier, M. Ingold, P. Germi and M. Pernet, Nature, 349 (1991) 770-772
[15] L.V. Woodcock, Proceeding of a workshop held at Zentrum fur interdisziplinare Forschung University Bielefield, Nov. 11-13, 1985 Edited by Th. Dorfmuller and G. Williams
[16] R. Furushima, S. Tanaka, Z. Kato and M. Uematsu, J. Ceram. Soc. Jpn., 118 [10] (2010) 921-926

Chapter 4

Anisotropic Shrinkage and Microstructural Evolution of *C*-axis Oriented $(Sr,Ca)_2NaNb_5O_{15}$ Ceramics during Sintering

4.1 INTRODUCTION

In the fabrication processing of crystal-oriented ceramics, some researchers have expressed concerns about anisotropic sintering because it is more complex and difficult to estimate. The crystal-oriented ceramics have been fabricated not only by forming processing under a magnetic field but also by subsequent sintering. Anisotropic microstructures prepared by the colloidal processing in the high magnetic field are developed during sintering. However, as shown in Figs. 2.16 and 2.17, if anisotropic grain growth occurs before complete densification the sample may not achieve a full dense state. In particular, it was clearly observed in highly oriented powder compacts.

The development of an anisotropic microstructure depends on fabrication parameters, such as the size of oriented template or large particles, their concentration, and the degree of orientation, as well as on material characteristics such as anisotropic mass transfer and grain boundary energy due to crystal anisotropy [1]-[12]. Mass mobility also depends on temperature and atmospheric pressure [1]-[4]. Solid state sintering usually involves densification and grain growth processes. Shrinkage generally occurs because of necking and its growth in the initial and middle stages of sintering, and the grain growth with the densification occurs in the middle and final stages [13,14]. In contrast, anisotropic sintering shrinkage and grain growth occur either sequentially or simultaneously, depending on the material [6,7],[11,12]. Furthermore, the crystallographic effects preferentially control neck formation and grain growth [11]. Simulation models have been reported by some researchers [15,16]. However, it is difficult to predict and control the final microstructure. The fabrication of highly oriented ceramics with a well-densified structure requires an understanding of the densification mechanisms leading to the development of microstructures.

The objective of this chapter was to examine the anisotropic sintering behavior of *c*-axis oriented $(Sr,Ca)_2NaNb_5O_{15}$ (SCNN) ceramics from initial to final sintering stages, and the associated development of an anisotropic microstructure at various sintering temperatures. Shrinkage behavior of the *c*-axis oriented and random SCNN green body during sintering was measured by using the shadow view technique. The development of

anisotropic microstructure during sintering was investigated not only from microstructure observation but also from crystal-oriented structure.

4.2 EXPERIMENTAL PROCEDURE

4.2.1 Raw Powder

Raw powders used in this chapter were synthesized by the same method described in Section 2.2.1. The morphology of the powder was observed through scanning electron microscopy (SEM, JSM-5310LVB, JEOL, Tokyo, Japan). The particle size distribution was determined by the sedimentation method (Sedigraph 5100, Micrometrics, USA). The powder was dispersed in deionized water with 0.025wt% sodium hexametaphosphate as the dispersing agent.

4.2.2 Forming and Sintering

The powder was dispersed in deionized water with ammonium polyacrylate as a solvent, and then a slurry with a solid content of 20 vol% was prepared by ball milling for 5 h. A zirconia ball of a diameter of 2.0 mm was used. The slurry was poured into a cylindrical plastic mole and then placed in a magnetic field of 10 T induced by a superconducting magnet (TM-10VH10, TOSHIBA Co. Japan) until the slurry dried (Figure 4.1). A static magnetic field of 10 T was applied in the direction parallel to the slurry surface, and the mold was rotated horizontally at a rotation speed of 30 rpm. For comparison, a sample was prepared without a magnetic field. After drying, the powder compact was removed from the mold and was heated at 5 °C/min to a temperature ranging between 1210 °C and 1300 °C for 30 min under air.

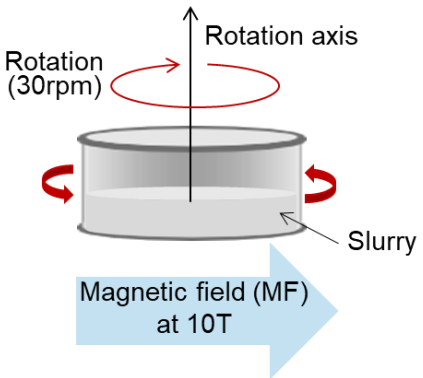

FIGURE 4.1 Sample setting in rotation magnetic field.

4.2.3 Measurement of Sintering Behavior

The sintering shrinkage was measured by the shadow view technique, as shown in Fig. 4.2 (a). The sample thickness and width were about 2 mm and 20 mm, respectively. The applied heating rate was 5 °C/min. The shadow views were taken every 5 min and were analyzed by a routine created using the Labview software (National Instruments, USA), as seen in Fig. 4.2 (b). The relative density, *RD*, was measured using the Archimedes method.

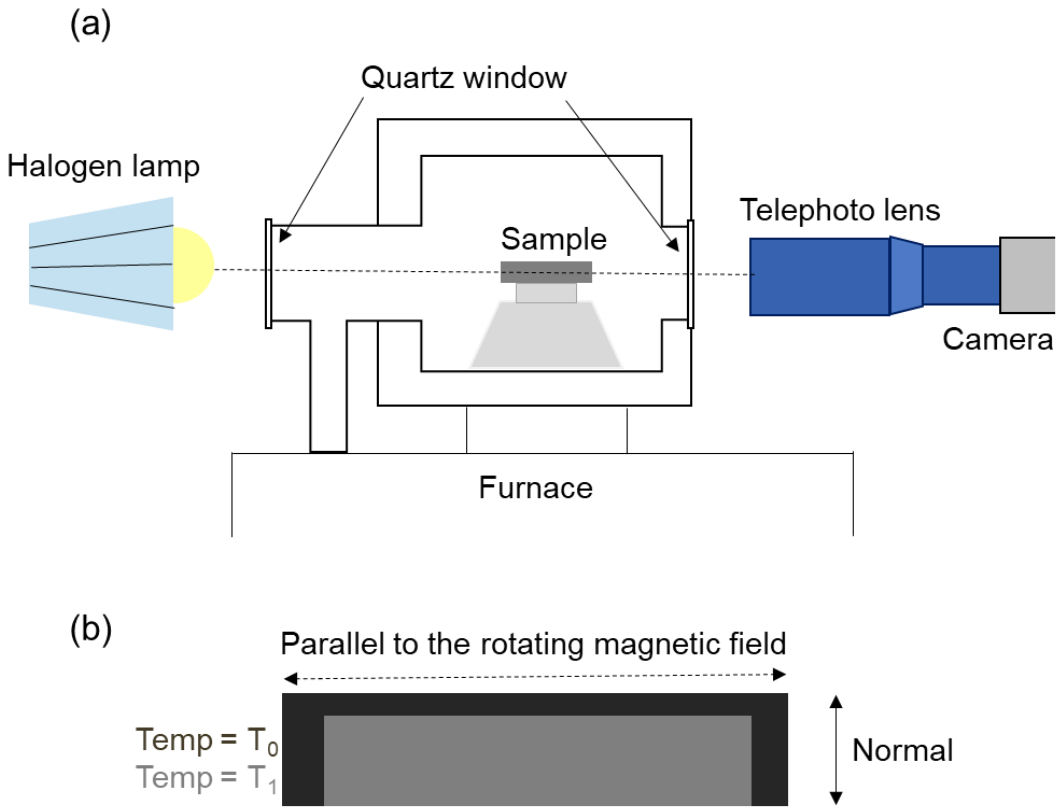

FIGURE 4.2 Schematic illustrations of experimental setting. (a) The sample was placed in the controlled furnace (b) The length was determined from image in each directions. The figure shows the sample at the initial temperature, T_0 (black) and the sample at the sintering temperature, T_1 (grey).

4.2.4 Characterization

The morphologies of the microstructures of both the surface and the cross-section of the powder compacts and sintering bodies were observed by SEM. All polished sintered bodies were thermally etched at 100 °C below the sintering temperature and coated with gold for SEM observation.

The evaluations of crystal orientations and the degree of *c*-axis orientation, *LF*, within the powder compacts and sintered ceramics are similar to those described in Section 2.2.4. Rocking curves of the 002 reflections for each sintered body were also measured. The multiple of a random distribution (MRD) was calculated and characterized by fitting with the March-Dollase function containing a texture volume fraction *f* as follows Eq. (3.4). The detail was described in Section 3.3.2.

As electron backscattering diffraction (EBSD) study was performed through field-emission scanning electron microscopy (FE-SEM, SU8230, Hitachi High-Technologies Corporation) and a silicon drift detector (X-Max^N, Oxford Instruments, UK). This technique allows the confirmation of the orientation of each grain during sintering. The obtained Kikuchi diffraction patterns were solved automatically by AztecHKL (Oxford Instruments, UK) software. The sintered samples were first polished by an ion milling method (Cross Section Polisher, IB-09020CP, JEOL Ltd., Japan) for 7 - 10 hours. The accelerate voltage was 3.0 kV. The surface without thermal etching was coated with amorphous osmium (Neoc-AN, Meiwafosis) to prevent charging during the EBSD analysis.

4.3 RESULTS AND DISCUSSION

4.3.1 Powder and Powder Compacts

Figure 4.3 shows a typical SEM image of the SCNN raw powder. The particles have irregular shapes; in particular, large particles have tabular shapes. Figure 4.4 shows the particle size distribution of the synthesized raw powder measured by the sedimentation method. The particle size was distributed in the range from 0.2 to 3.0 μm. The median particle size, D_{50}, was 1.1μm.

Figure 4.5 shows XRD patterns of the powder compacts prepared with and without a rotating magnetic field. The intensity of the peaks from the *c*-plane in the sample prepared with the rotating magnetic field, such as 001 and 002 planes, was significantly enhanced. In contrast, the XRD patterns of the sample produced without the rotating magnetic field were coincident with the International Centre for Diffraction Data (ICDD)

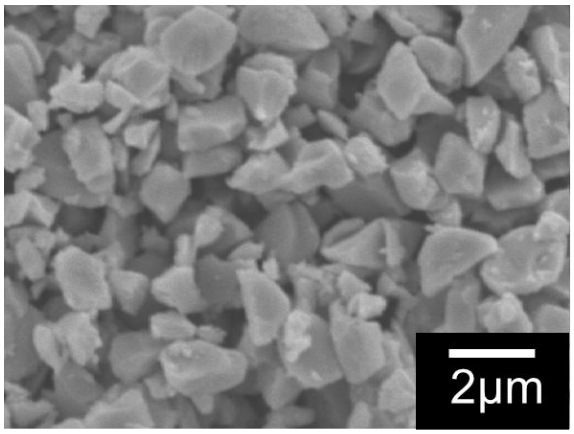

FIGURE 4.3 Particle morphology of SCNN. (D_{50} = 1.1 μm)

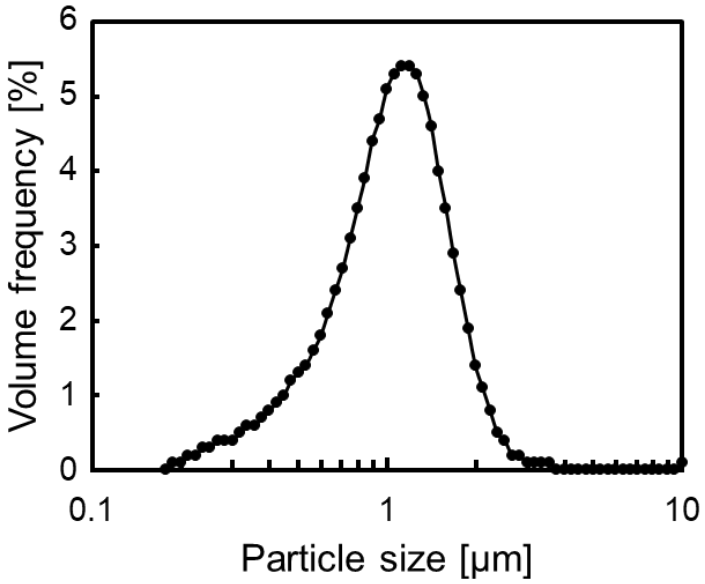

FIGURE 4.4 Particle size distribution of the raw SCNN particles.

card No. 00-034-0429 for $Sr_2NaNb_5O_{15}$. The Lotgering factor *LF* of the powder compact prepared in a magnetic field was 0.33. As shown in Fig. 2.17, when the *LF* was above 0.6, the relative density of highly oriented samples could not reach 90% because of the remarkable anisotropic grain growth.

Figure 4.6 shows SEM images of the cross-section in the powder compacts prepared (a) with and (b) without the rotating magnetic field. No significant difference was observed in the microstructures.

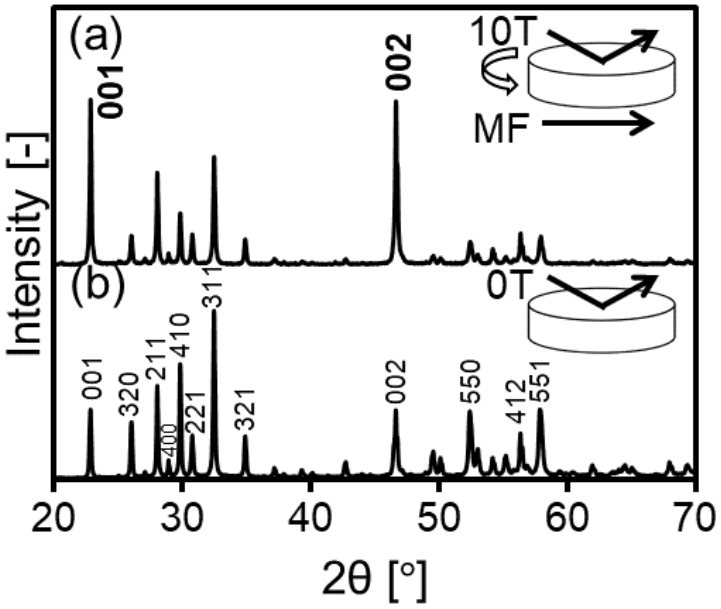

FIGURE 4.5 XRD patterns obtained from powder compacts prepared (a)with and (b)without a rotating magnetic field.

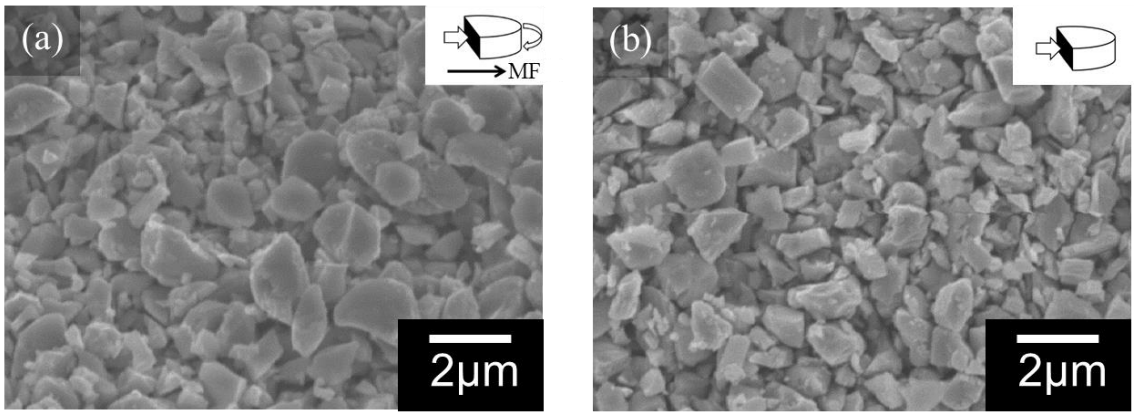

FIGURE 4.6 Cross section microstructures of powder compacts prepared (a) with and (b) without the magnetic field at 10 T.

4.3.2 Anisotropic Sintering Shrinkage and Microstructure

Figure 4.7 (a) shows the shrinkage curves measured from the shadow views of the *c*-axis oriented powder compact. The sample shrunk in the vertical direction at the lower temperature and in the horizontal direction at the higher temperature. The difference in the shrinkage magnitude between both directions was enhanced with an increase in the sintering temperature above 1150 °C. Figure 4.7 (b) shows the shrinkage rate for each direction calculated from the relative displacement. In the vertical direction, in which the *c*-axis of particles was considerably oriented, the maximum shrinkage rate was at 1210 °C. Meanwhile, in the horizontal direction, the shrinkage rate was fast as 1210 °C and 1260 °C, with a clear extremum at 1260 °C. The result indicates that sintering starts preferentially along the *c*-axis direction at low temperatures, followed by densification along the *a*-axis direction at high temperatures.

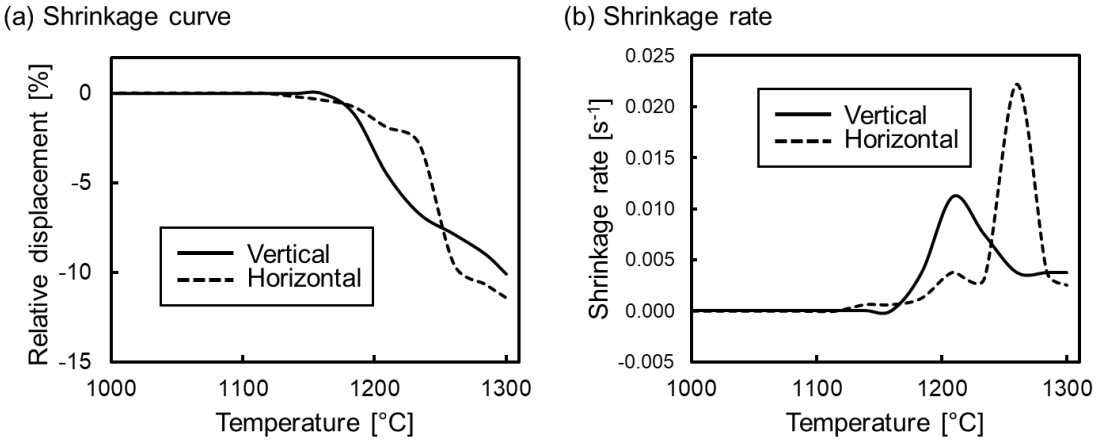

FIGURE 4.7 The shrinkage curve and shrinkage rate of oriented sample for vertical and horizontal direction to the rotating magnetic field during sintering.

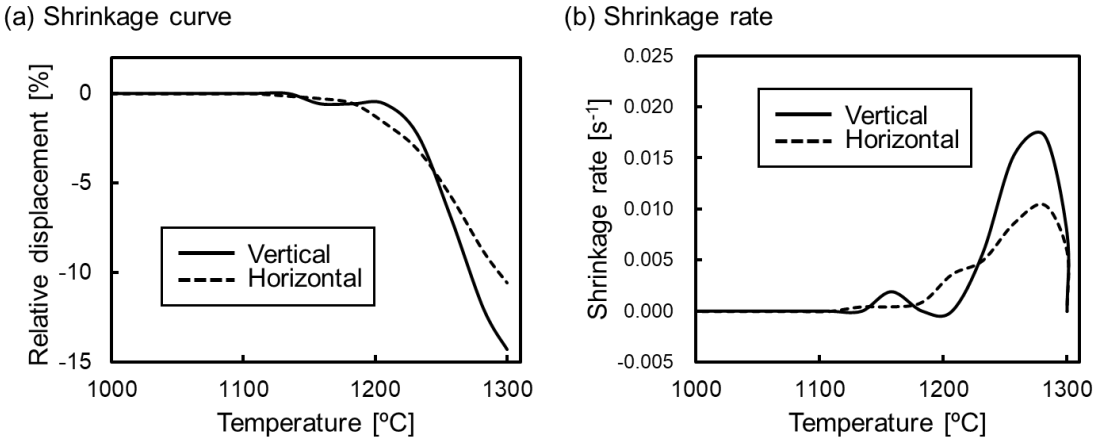

FIGURE 4.8 The shrinkage curve and shrinkage rate of random sample for vertical and horizontal direction to the drying surface.

For comparison, Figure 4.8 (a) shows the shrinkage curves of the randomly oriented powder compact measured from the shadow views. Although difference in the shrinkage magnitude was observed, the shrinkage of the sample in each direction occurred simultaneously at the sintering temperature above 1200 °C. At higher temperature, the magnitude of the relative displacement along the vertical direction is larger than that along the horizontal direction. The results indicate that the difference in relative displacement along each direction is ascribed to the differential packing microstructure in the green compact developed in the forming process [8,9]. Figure 4.8 (b) shows the shrinkage rate in each direction calculated from the relative displacement of the randomly oriented powder compact. The sintering shrinkage occurs almost isotropically. Shrinkage rates peaked at 1280 °C in both horizontal and vertical directions.

Figures 4.9 and 4.10 show the microstructures of the samples prepared with and without a rotating magnetic field heated at the temperature between 1210 and 1300 °C. The microstructures were observed in sections perpendicular and parallel to the rotating magnetic field. As shown in Figs. 4.9 (a, b) and 4.10 (a, b), neck formation among particles was observed at the initial stage of sintering. No noticeable difference was still seen in the microstructures regardless of shrinkage difference. Figures 4.9 (c, d) show the development of anisotropic microstructures in which longitudinal grains and columnar pores are oriented along the vertical direction, which corresponds to the *c*-axis of the particles. In addition, the longitudinal grains were connected in the vertical direction. It suggests that *c*-axis oriented grains formed the neck and grew by including particles along the vertical direction, resulting in an anisotropic microstructure with the preferential shrinkage in the vertical direction. This is similar to the findings observed in a previous study for SBN60 [11]. SBN60 showed large shrinkage along the longitudinal direction of particles in spite of the small amount of necking among particles. In contrast, as shown in Figs. 4.9 (e, f), it is observed that a neck (grain boundary) formed and grain growth started to occur along the horizontal direction, which corresponds to the *a*-axis direction. The grain growth along the vertical direction continuously occurred at 1260 °C. The microstructural changes corresponded to the shrinkage related to the horizontal direction, as shown in Fig. 4.7. Figures 4.9 (g, h) show that densification with grain growth was almost finished in the sintered sample at 1300 °C. On the other hand, isotropic development of microstructure was observed in the sintered bodies prepared without a rotating magnetic field, as shown in Fig. 4.10. The SEM images almost showed the same microstructures in both planes at each temperature. Thus, the anisotropic development of a microstructure is obviously associated with the crystal orientation of the green compact.

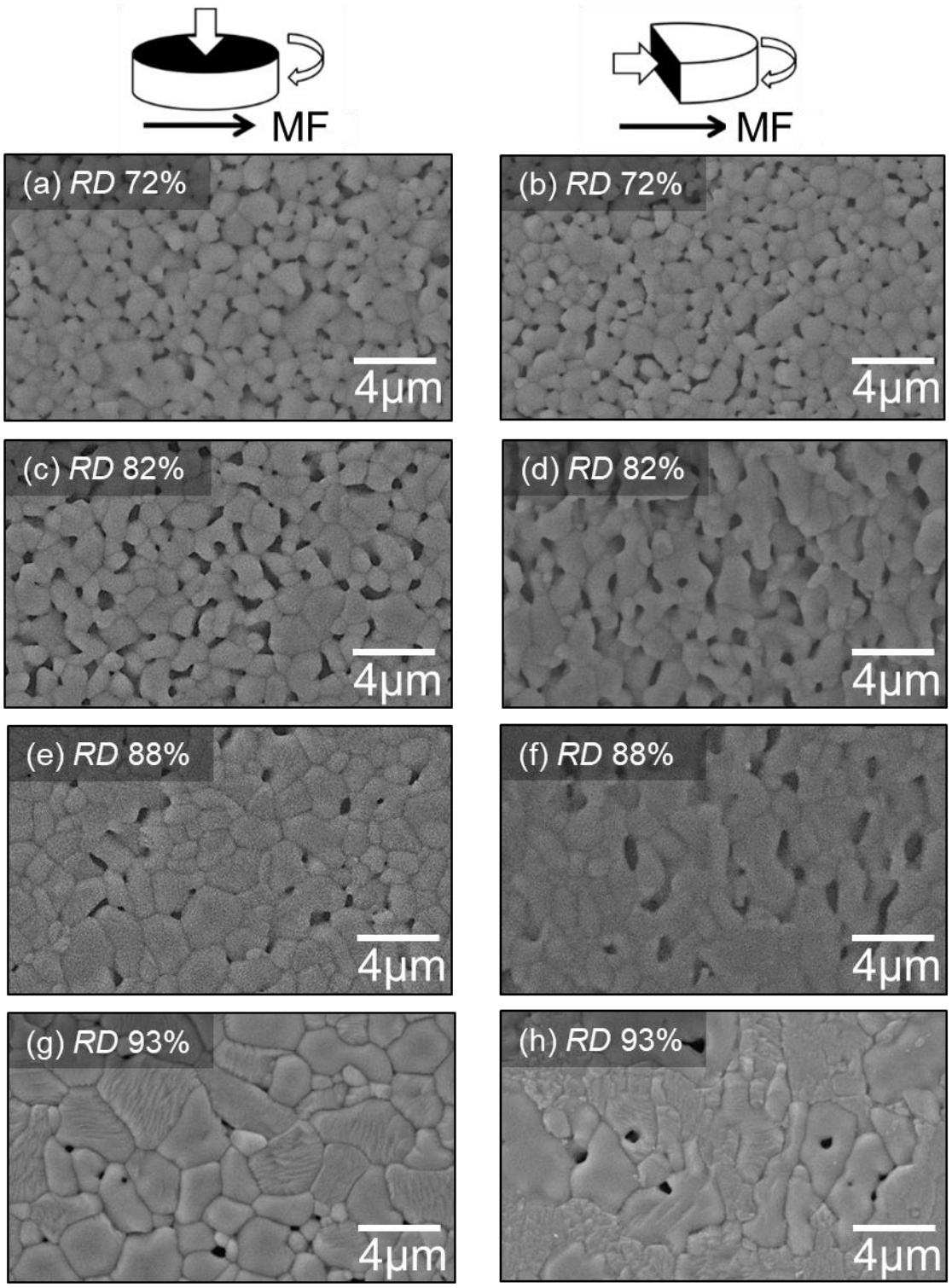

FIGURE 4.9 Microstructure of oriented samples heat treated at (a and b) 1210 ºC, (c and d) 1230 ºC, (e and f) 1260 ºC and (g and h) 1300 ºC for 30 min. The observed directions are (a, c, e and g) perpendicular to the magnetic field and (b, d, f and h) parallel to the magnetic field.

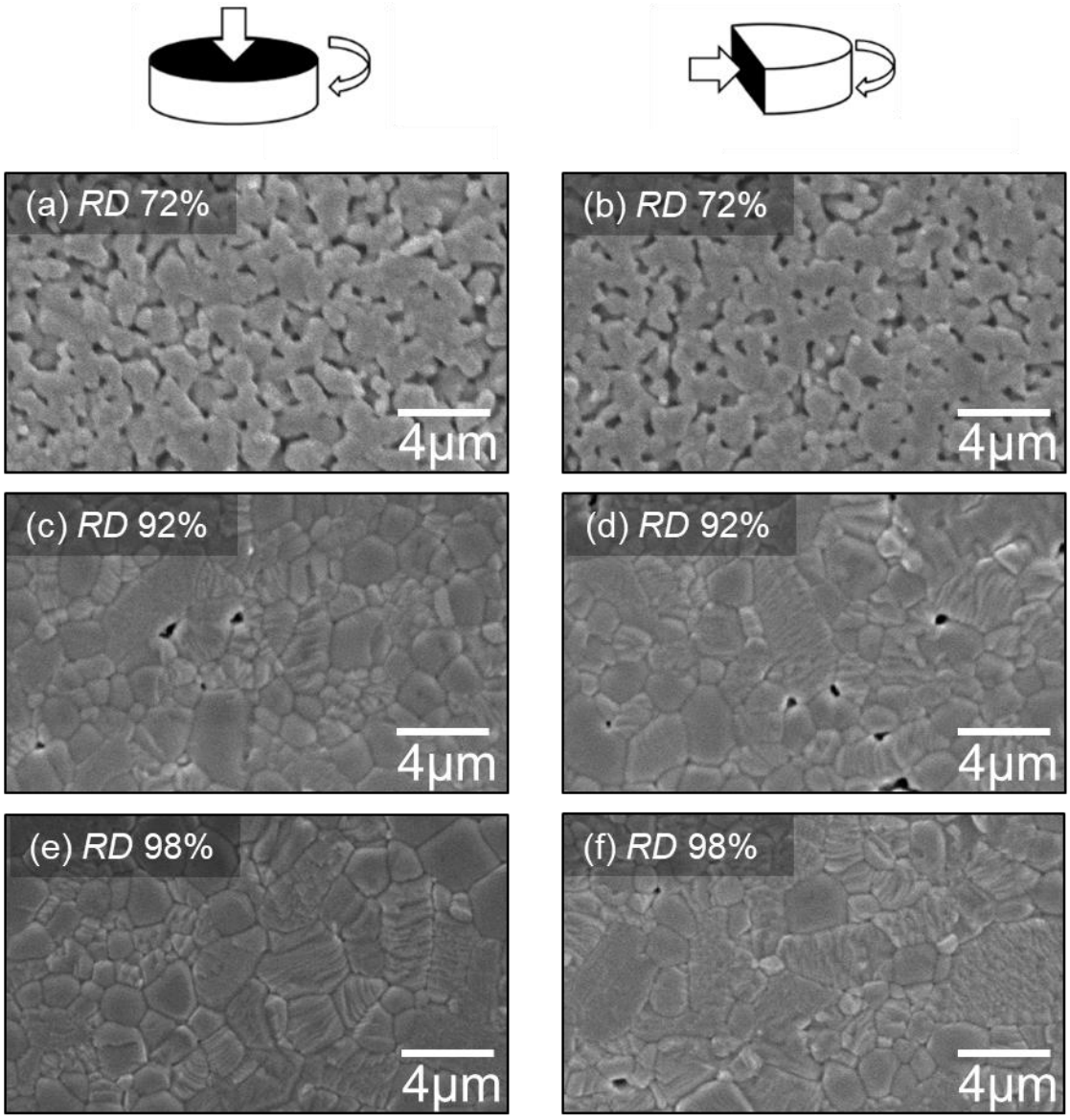

FIGURE 4.10 Microstructure of random samples heat treated at (a and b) 1210 ºC, (c and d) 1230 ºC and (e and f) 1260 ºC for 30 min. The observed directions are (a, c and e) perpendicular to the drying surface and (b, d, and f) parallel to the drying surface.

Figure 4.11 presents the grain sizes and shrinkage rates of the *c*-axis oriented sample for the vertical and horizontal directions as a function of sintering temperature. The vertical direction corresponded to the *c*-axis orientation and longitudinal direction of particles. Shrinkage and grain growth tended to sequentially occur depending on the respective crystallographic orientations. When sintering temperature was increased from 1200 to 1260 °C, shrinkage and grain growth occurred, following those along to the *a*-axis from 1260 to 1300 °C. In SCNN, the preferred direction of grain growth for tungsten-bronze-structured materials is generally along the *c*-axis [11],[17]-[21]. These results

indicate that crystallographic characteristics govern the mobility of ions and grain boundaries. To obtain crystal-oriented SCNN ceramics, grain growth in the *c*-axis direction plays an important role in densification.

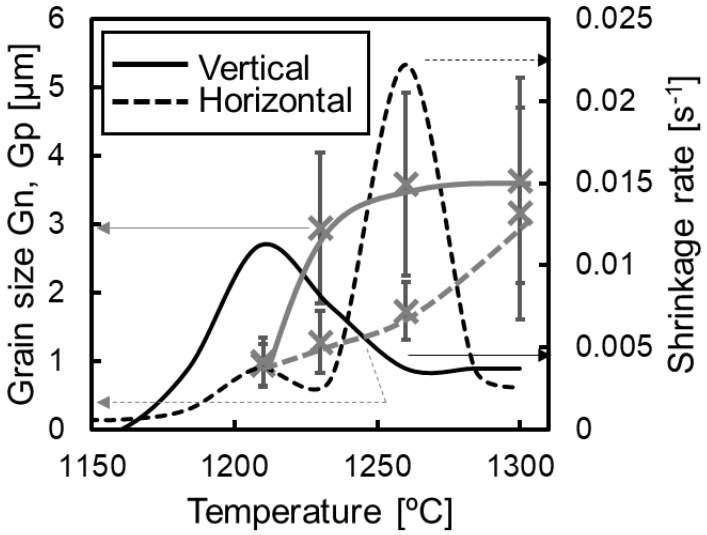

FIGURE 4.11 Grain size and shrinkage rate of oriented sample along vertical or horizontal to the magnetic field as a function of sintering temperature.

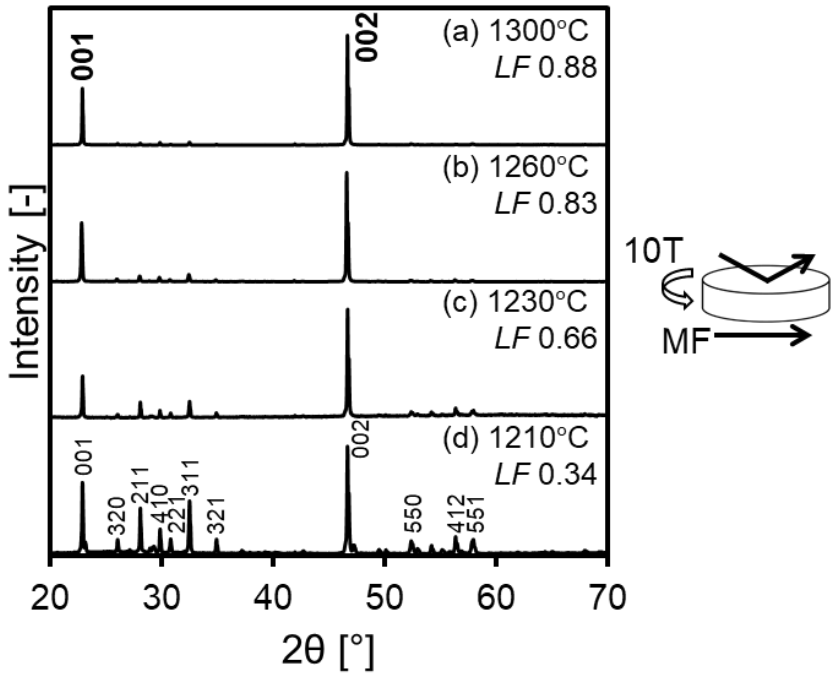

FIGURE 4.12 XRD patterns of oriented samples for various sintering temperature at (a) 1300 ºC, (b) 1260 ºC, (c) 1230 ºC and (d) 1210 ºC.

4.3.3 Development of Crystal-Oriented Structure

Figure 4.12 shows XRD patterns of oriented samples sintered at each temperature in the range from 1210 to 1300 °C. The intensities of diffraction peaks of the *c*-plane increased with increasing sintering temperatures, which peaks relevant to the decrease in *a*- and *b*-planes. The *LF* increased gradually with increasing sintering temperatures. The rocking curves (MRD) of the 002 peaks for these samples are shown in Fig. 4.13. The solid lines are curves fitted by Eq. (3.4). The peak intensity increased with an increase in the sintering temperature. These results show that the oriented microstructure was developed during sintering.

Table 4.1 lists the values of relative density *RD*, *LF*, *r*, and *f* for these *c*-axis oriented samples. The relative density increased from 72 % to 93 % as a function of the sintering temperature. The textured fraction *f* increased with temperature and *r* was constant. This relationship between *r* and *f* indicates that the distribution of orientations remains constant, while the amount of oriented material was increased. This suggests that large grains generally oriented along the vertical direction grow by including random particles.

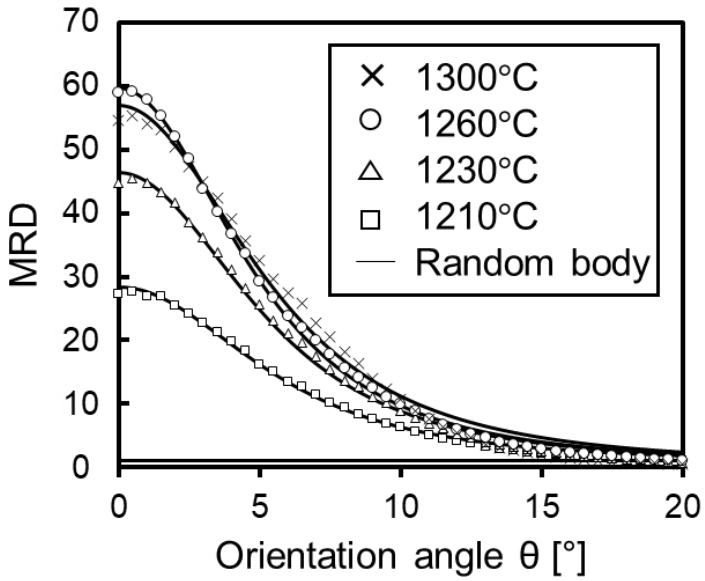

FIGURE 4.13 Rocking curves, MRD, of oriented samples for various sintering temperature in the range from 1210 ºC to 1300 ºC. The solid lines are fitted curves with March-Dollase function Eq. (3.4).

TABLE 4.1 Relative density, Lotgering factor (*LF*), orientation parameter *r* and textured fraction *f* at each sintering temperature.

Sintered temperature [℃]	Relative density [%]	*LF*	Orientation parameter (*r*)	Textured fraction (*f*)
1210	72	0.34	0.25	0.44
1230	82	0.66	0.24	0.66
1260	88	0.83	0.23	0.73
1300	93	0.88	0.25	0.85

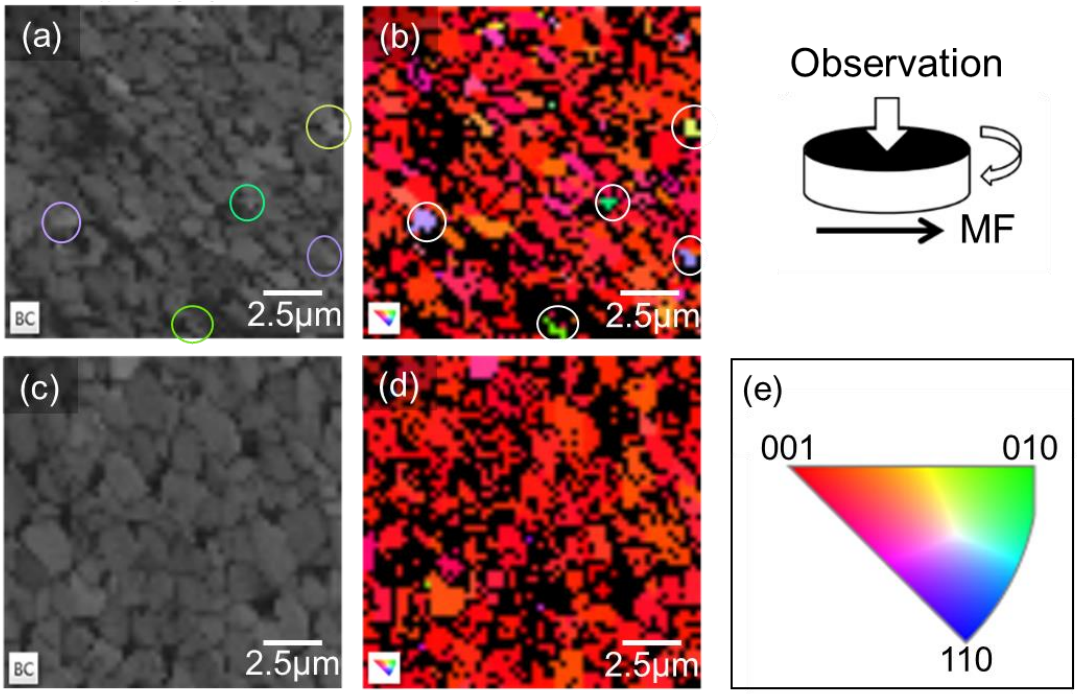

FIGURE 4.14 Band contrast and EBSD map of oriented samples heat treated at (a and b) 1230 ºC and (c and d) 1260 ºC for 30 min observed from perpendicular to the rotating magnetic field. (a and c) band contrasts, (b and d) EBSD maps of x-direction and (e) stereographic triangle.

The grain growth of oriented particles was assumed to contribute to the development of an anisotropic microstructure during sintering. This assumption was confirmed by the EBSD measurement. Figure 4.14 shows band contract and EBSD maps of oriented samples heated at 1230 °C and 1260 °C. The samples were observed perpendicular to the rotating magnetic field, which corresponds to the *c*-axis direction. From the band contrast, remarkable grain growth was observed. In EBSD maps, various colors presented crystal

direction in each region, which was identified by Kikuchi patterns, whereas unidentified regions were shown as black areas. Because the relative density *RD* of these samples was 82 % and 88 %, and these black areas regions were almost pores in the samples. Few unoriented particles, which were small particles and were expressed in violet, green, or yellow, were present in the sample heated at 1230 °C, as shown in Fig. 4.14 (b). Figure 4.14 (d) shows that the grains grew in the sample sintered at 1260 °C and almost all the grains appeared to ret, indicating that almost all particles were aligned along the [001] direction. The observation suggested an oriented microstructure is developed because of the grain growth of oriented particles including unoriented particles.

Models of graded sintering with grain growth and densification for anisotropic microstructure in *c*-axis oriented SCNN ceramics can be schematically illustrated, as shown in Fig. 4.15. Crystal-oriented powder compacts have oriented and unoriented particles. Here, the direction of arrows in the figure indicates the *c*-axis direction of SCNN particles. The large particles in the slurry tend to align easily due to the large magnetic torque (Figure 4.15 (a)). At the initial stage of sintering, the necks between the particles are still randomly formed. Then, as shown in Fig. 4.15 (b), the large particles show neck growth with particles adjacent to the *c*-axis direction of the particle, and some particles lose their grain boundaries and become vertically elongated grains. In other words, it shows grain growth in the c-axis direction. At the same time, the shrinkage of the sample shrinks along the *c*-axis. Although it shrinks slightly in the perpendicular direction, the amount of shrinkage is larger on the *c*-axis (Figure 4.15 (b)). The pores are elongated in the *c*-axis direction. The previous reports suggested that the shrinkage along to the *c*-axis direction was dominant in tungsten bronze-type materials [17,21]. This is because the diffusion rate of ions along the *c*-axis direction is dominant. Alternatively, this anisotropic sintering may be due to the low energy of grain boundary composed of the *c*-plane or the

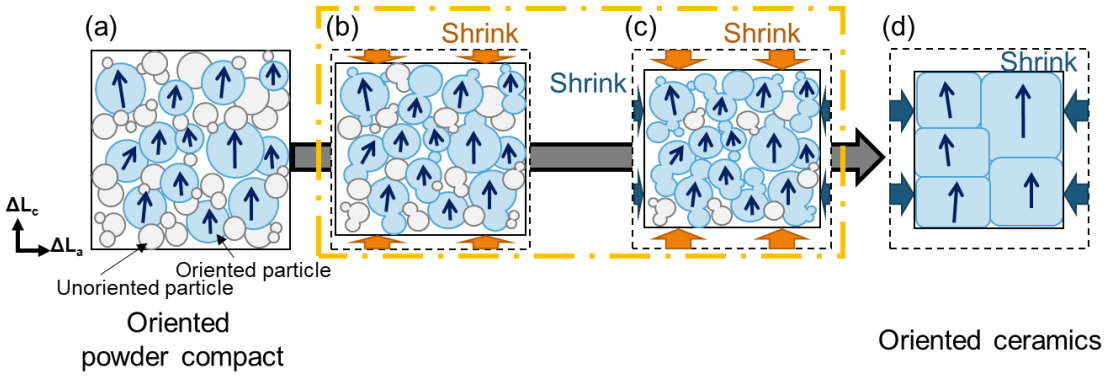

FIGURE 4.15 Schematic illustrations of the grain growth mechanism of *c*-axis oriented SCNN ceramics prepared in a rotation magnetic field.

low energy of the *c*-plane of grain. After the middle stage of sintering, the grain growth starts in a horizontal direction, that is, in the direction corresponding to *a*-axis of the particles, as shown in Fig. 4.15 (c), and the shrinkage in that direction also increases. As a result, the *c*-axis oriented microstructure increased during sintering. At the final stage of sintering, as shown in Fig. 4.15 (d), densification with grain growth was almost finished. Thus, graded grain growth with densification leads to the evolution of anisotropic microstructure. And the grain growth of oriented grains with taking in random fine grains contributes to the development of oriented microstructure.

4.4 CONCLUSIONS

Anisotropic shrinkage and grain growth during sintering of *c*-axis oriented SCNN ceramics were investigated in this study. The sintering along the vertical direction, that is, the *c*-axis direction preferentially occurred at 1200 °C. The neck formation and grain growth along the *c*-axis direction correspond to the large shrinkage. At 1260 °C high temperature, grains preferentially grew along the horizontal direction, that is, the *a*-axis direction. The oriented microstructure in the powder compact developed during sintering. XRD, SEM, and EBSD showed that the grain growth of oriented particles by including random grains contribute to the development of the oriented microstructure. To prepare ceramics with a highly oriented and densified microstructure, it is important to design the particle packing structure in a powder compact to control the structural development during sintering.

REFERENCES

[1] E. Suvaci and G. L. Messing, J. Am. Ceram. Soc., 83[8] (2000) 2041-2048
[2] M. M. Seabaugh, G. L. Messing and M. D. Vaudin, J. Am. Ceram., 83[12] (2000) 3109-16
[3] İ. Ö. Ozer, E. Suvaci, B. Karademir, J. M. Missiaen, C. P. Carry and D. Bouvard, J. Am. Ceram. Soc., 89[6] (2006) 1972-1976
[4] Y. Chang, S. Poterala, D. Yener and G. L. Messing, J. Am. Ceram. Soc., 96[5] (2013) 1390-1397
[5] İ. Ö. Ozer, E. Suvaci and S. Bernik, Acta Materialia, 58 (2010) 4126–4136
[6] E. Suvaci and İ. Ö. Ozer, J. Eur. Ceram. Soc., 25 (2005) 1663-1673
[7] J. S. Patwardhan and W. Roger Cannon, J. Am. Ceram. Soc., 89[10] (2006) 3019-3026
[8] F. V. Dimarcello, P. L. Key and J. C. Williams, J. Am. Ceram. Soc., 55 (1972) 509-514
[9] A. Shui, Doctor thesis, Nagaoka university of technology (2002)
[10] S. Tanaka, Y. Nagashima, R. Furushima and K. Uematsu, Mater. Sci. Eng., 21 (2011) 012008
[11] T. Takahashi, S. Tanaka, Z. Kato and K. Uematsu, J. Ceram. Soc. Jpn., 121 (2013) 411-415
[12] T. Takahashi, J. Tatami, H. Nakano and S. Tanaka, J. Ceram. Soc. Jpn., 127[6] (2019) 435-442
[13] M. N. Rahaman, Ceramic processing and sintering, Marcel Dekker, Inc., 482-506
[14] Suk-Joong L. Kang, Elsevier, 39-76
[15] P. Markondeya Raj, A. Odulena and W. R. cannon, Acta Materialia, 50 (2002) 2559-2570
[16] S. Biswas, D. Schwen, H. Wang, M. Okuniewski and V. Tomar, Comput. Mater. Sci., 148 (2018) 307-319
[17] R. R. Neurgaonkar, W. K. Cory, J. R. Oliver, E. J. Sharp, G. L. Wood, M. J. Miller, W. W. Clark and G. J. Salamo, Mat. Res. Bull., 23 (1988) 1459-1467
[18] R. J. Xie, Y. Akimune, R.P. Wang, and N. Hiroaki, J. Am. Ceram., 85[11] (2002) 2725-2730
[19] L. Wei, X. Chao, X. Han and Z. Yang, Mater. Res. Bull., 52 (2014) 65-69
[20] H. Shimizu, Y. Doshida, S. Tanaka, and K. Uematsu, Jpn. J. Appl. Phys., 47[9] (2008) 7693-7697
[21] W. Chen, S. Kume, C. Duran and K. Watari, J. Eur. Ceram. Soc., 26 (2006) 647-653

Chapter 5

Fabrication of *C*-axis Oriented $(Sr,Ca)_2NaNb_5O_{15}$ Laminated Ceramics Using Repeating Photopolymerization Reaction in Rotating Magnetic Field

5.1 INTRODUCTION

A novel method using a photopolymerization reaction was reported to shorten the solidification time in the magnetic field. It achieved to shorten the forming time in the rotating magnetic field to just 30 s and to fabricate *c*-axis oriented $(Sr,Ca)_2NaNb_5O_{15}$ (hereafter, reoffered to as SCNN) monolayer ceramics. However, the thickness of SCNN sintered sheets was considerably thin below 100 μm because of the light scattering depending on the refractive index difference between the binder and particles and of the absorption by particles. It is necessary to propose the technique for fabricating the thick sintered sample.

One of the solutions for the fabrication of ceramics components is to apply a repeated polymerization processing, which was originally named "stereolithography (SL)" by Hull [1]. Currently, research on stereolithgraphy is going on. A curable system consisting on UV curable resin, photoinitiator, and ceramic powder is prepared to produce a 3D complex shaped bulk ceramics and a laminated ceramic component by additive manufacturing [2]-[6]. Recently, piezoelectric ceramics such as $Pb(Zr,Ti)O_3$ (PZT), $0.65Pb(Mg_{1/3}Nb_{2/3})O_3$-$0.35PbTiO_3$ (PMNT) and $K_{0.48}Na_{0.52}NbO_3$ (KNN) are prepared by SL technique [7]-[9]. Jiang et al. reported the fabrication of PZT thick film on silicon substrate by SL [7]. The fabricated sample showed a pezoelectiric constant d_{33} of 100 pC/N, and a g_{33} of 58.5×10^{-3} V m/N. Woodward et al. developed an SL process for the additive manufacturing of PMNT [8], producing PMNT with a thickness of 1.5 mm, a width of 6 mm, and a relative density of 97.8 %. Chen et al. investigated the fabrication of KNN based lead-free piezoelectric ceramics by SL [9]. However, the SL in a high magnetic field for piezoelectric ceramics has not been investigated.

The objective in this chapter was to fabricate *c*-axis oriented bulk SCNN ceramics by repeatedly performed photopolymerization reaction in a rotating magnetic field and following by sintering. The processing time in the magnetic field required for orientation of the particles was calculated from the viscosity at zero shear rate, as shown in chapter 3. Since the laminated samples tend to result in interface failure (e.g., cracking and

delamination) during sintering [10,11], the structure development of the polymerize green laminated compacts was also examined during sintering. Then, its piezoelectric properties includings *P-E* hysteresis loops and piezoelectric constant d_{33} were evaluated.

5.2 EXPERIMENTAL PROCEDURE

5.2.1 Slurry Preparation and Characterization

The raw powders used in this chapter were same as those discribed in chapter 2. They are also deagglomerated. The morphology of the deagglomerated powder was examined by the scanning electron microscope (SEM, JSM-5310LVB, JEOL Tokyo, Japan).

The slurry for forming the green sheets was prepared in the same method described in Section 2.2.2. The UV-curable resin was used as the dispersion medium and contained polyether acrylate monomer diluted in hydroxyethyl methacrylate with 2 wt% of the photoinitiator 2-hydroxy-2-methyl-1-phenylpropan-1-one. A phosphate ester with 1.2 wt% was used as the dispersant, which acts by both electrostatic and steric repulsion. The volume fraction of the SCNN powders was 55 vol%.

The viscosity of the slurry was measured by the rheometer (Physica MCR301, Anton Paar, Austria) using a cone-plate apparatus (CP25-2) in the stress-controlled mode. The shear rate was varied from 0.001 s^{-1} to 100 s^{-1}. The curve of slurry viscosity was characterized by fitting with the Cross model following Eq. (3.3) using the nonlinear least-squares method.

5.2.2 Fabrication and Characterization of Laminated Green Compacts

After keeping the slurry in a thermostatic bath at 20 °C for 1 hour, it was cast on a poly ethylene terephthalate (PET) film. The cast slurry was spread on the PET film by the spin coater (Opticoat MS-A 100, MIKASA Co. Japan) at 1000 rpm for 5 s in order to control the thickness of the slurryt to approximately 0.1 mm. Then, the slurry sheet on the PET film was placed in a magnetic field (10 T) induced by a superconducting magnet (TM-10VH10, TOSHIBA Co. Japan) for 1 s to 150 s. The magnetic field of 10 T was applied in the direction parallel to the slurry surface, and the sheet was rotated on the axis perpendicular to the magnetic field at a rotation speed of 30 rpm, then UV rays were irradiated for 30 s (i.e., E=10.8 J/cm^2). The casting of the slurry on the sheet and the photopolymerization reaction in the magnetic field were repeatedly performed to produce

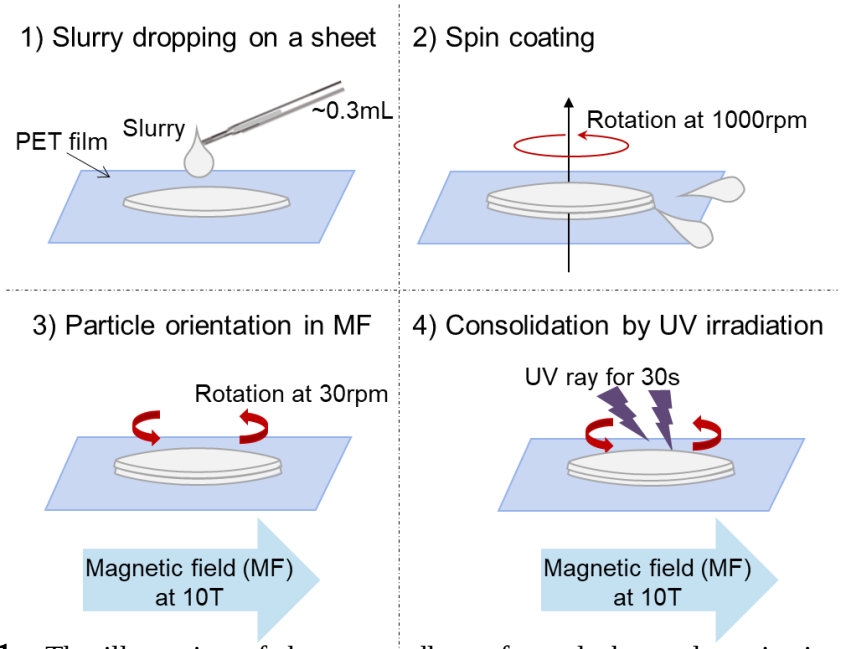

FIGURE 5.1 The illustration of the repeatedly performed photopolymerization reaction processing in the magnetic field.

the laminated green compacts as shown in Fig. 5.1. The laminated green compacts with a thickness of ~700 μm were obtained by repeating seven times in total. For comparison, a sample was prepared without the magnetic field by the same process as shown in Fig. 4.1. The crystal orientations of the surface of the green laminated sheets were evaluated by X-ray diffraction (XRD, Ultima-IV, RIGAKU Japan) using Lotgering's methods. The degree of orientation along the *c*-axis was evaluated in terms of the Lotgering factor *LF* of [00l] orientation. The detail was written in Section 2.2.4.

5.2.3 Binder Removal and Sintering

The de-binding of both the *c*-axis oriented and randomly oriented green compacts were performed at a heating rate of 1 °C/min up to 100 °C and 0.2 °C/min up to 500 °C. Then, the compacts were sintered at a temperature of 1240 °C for 2h. A heating rate was 5 °C/min.

The crystal orientations of the surface of the sintered ceramics were also characterized by XRD analysis. The degree of orientation was evaluated by the Lotgering Factor *LF*. The relative density (*RD*) of the samples was measured using Archimedes method. The microstructures of both the surface and the cross-section of the sintered samples were examined by the SEM. All polished sintered bodies were thermally etched at 1140 °C for 30 min and coated with gold for SEM observation.

As electron backscattering diffraction (EBSD) study was performed through a field-emission scanning electron microscope (FE-SEM, SU8230, Hitachi High-Technologies Corporation) and a silicon drift detector (X-Max^N, Oxford Instruments, UK). The obtained Kikuchi diffraction patterns were recognized automatically by AztecHKL (Oxford Instruments, UK) software. The sintered samples were first polished by an ion milling (Cross Section Polisher, IB-09020CP, JEOL Ltd., Japan) for 7 h. The accelerate voltage was 3.0 kV.

5.2.4 Measurement of Piezoelectric Properties

The polarization curves at room temperature were measured as a function of the electric field by using a commercial apparatus (Type-FCE-1, TOYO Corp., Tokyo, Japan). The samples were poled in silicone oil at 25 °C for 15 min under an electric field of 4 kV/mm, perpendicular to the magnetic field direction. The measurement was conducted at a frequency of 1 Hz. The sample was polished by polishing machines using diamond slurries. Gold electrodes with an circular area of 18.1 mm^2 and a thickness of 1 nm were sputtered on both surfaces of the sample using a sputtering apparatus (FINE COAT, JFC-100, JEOL Ltd., Japan). The piezoelectric d_{33} constant was measured with a d_{33} meter (ZJ-6B, Institute of Acoustics, Chinese Academy of Sciences, China).

5.3 RESULTS AND DISCUSSION

5.3.1 Materials and Slurry

Figure 5.2 shows an SEM image of deagglomerated SCNN powders. The median particle size D_{50} of deagglomerated powders was 0.94 μm.

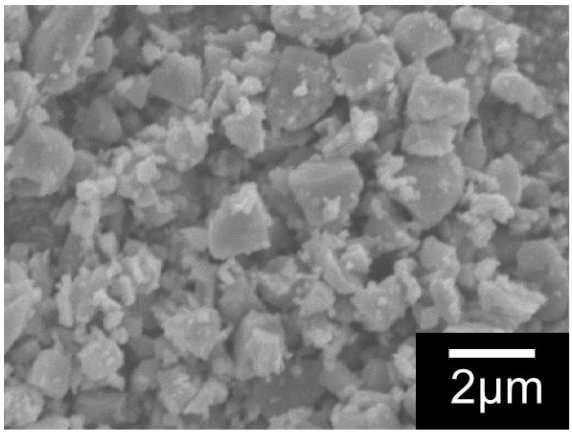

FIGURE 5.2 Particle morphology of deagglomerated powder (D_{50} = 0.94 μm).

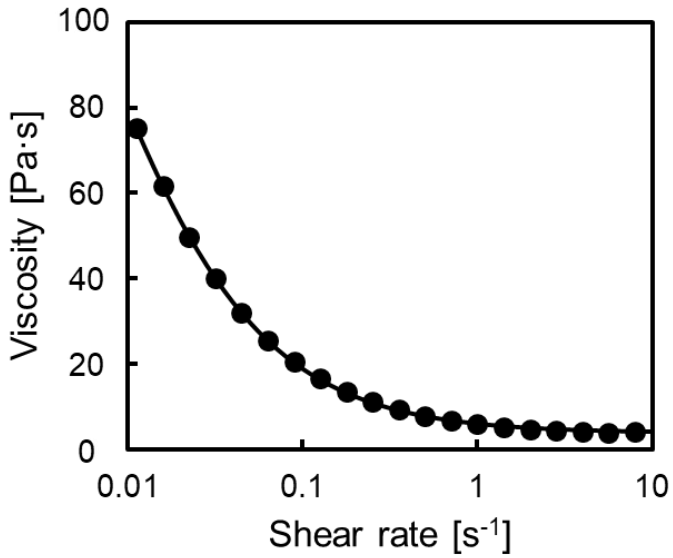

FIGURE 5.3 Viscosity curve of slurry containing 55 vol% SCNN powder, UV curable resin, dispersant and photoinitiator. The solid lines are the fitted curves with Cross model Eq (3.3).

Figure 5.3 shows the viscosity curve obtained from the prepared slurry with a solid content of 55 vol%. The viscosity decreased dramatically with the increase of shear rate. The solid lines are the curves fitted with the Cross model represented in Eq. (3.3). The values of η_0 determined by fitting with the Cross model is 215 Pa·s. Here, the intrinsic magnetic response rate τ^{-1} and orientation time t were calculated from its viscosity at zero shear rate and magnetic flux density of 10 T. The values of τ^{-1} and t estimated using Eqs. (3.1) and (3.2) were 0.017 s^{-1} and 120 s, respectively.

5.3.2 Monolayer Green Sheets

Figure 5.4 shows XRD patterns of the monolayer green sheets prepared for a duration time of 30 s, 60 s and 150 s with and without a rotating magnetic field after spreading the slurry on the PET film by using the spin coater. The intensities of the peaks from *c*-planes of the crystal enhanced with the duration time in the rotating magnetic field. In the diffraction peaks of the green sheet prepared without the magnetic field, the intensity of the peaks from *c*-planes enhanced slightly. The Lotgering factor *LF* of the oriented samples increased with increasing processing time under the magnetic field. The *LF* was 0.34 for the sample prepared in the rotating magnetic field with a holding time of 150 s. The *LF* was 0.07 for the sheet immediately cured after spreading the slurry by spin coater. This suggests that the particles in the slurry aligned due to the shear stress by spin coating [12]. The *c*-plane of SCNN particles oriented along the rotating axis of spin coater because the particles have a slightly anisotropic shape.

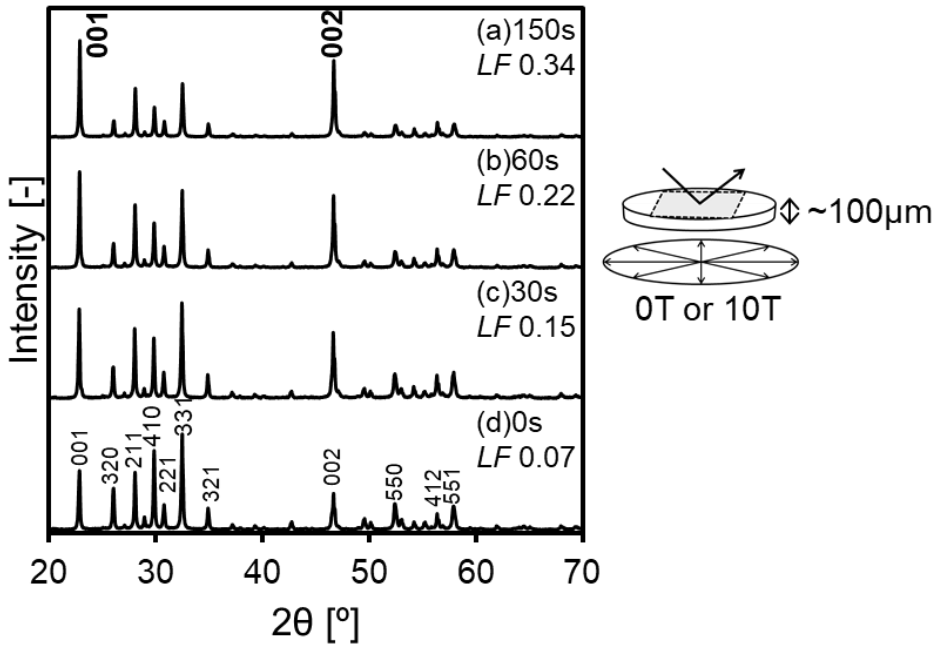

FIGURE 5.4 X-ray diffraction patterns obtained from green sheets for various duration times of (a) 150 s, (b) 30 s and (c) 10 s (a, b and c) with and (d) without a 10 T rotating magnetic field.

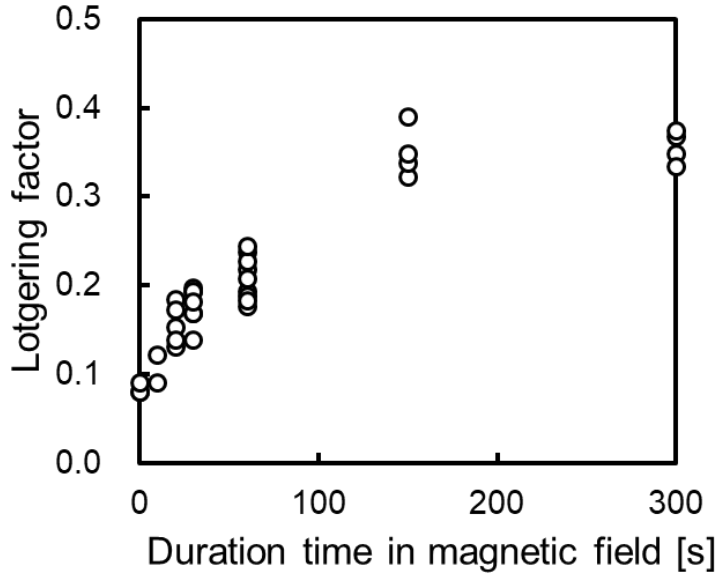

FIGURE 5.5 The orientation degree of fabricated by various duration times in rotating magnetic field of 10T. The solid concentration in the slurry was 55 vol%.

Figure 5.5 shows the relationship between the exposure time of the sample in the magnetic field and the degree of orientation, *LF*, of the green sheets exposed to 10 T. The *LF* depends on the duration of exposure to the magnetic field and gradually increased with exposure time. Several hundred seconds of ~150 s was required to saturate the degree of orientation. It is almost the same value as the orientation time *t* calculated using the applied model equations (at 120 s). The results indicated that the orientation time could be predicted from the measured viscosity of the highly concentrated slurry. However, the saturation value of *LF* was low as ~ 0.4. As seen in Figure 3.10, the inter-particle distance decreased suddenly in the slurry with solid contents of > 45 %. This means that the particles are likely flocculate easily in the slurry. This strongly affects the decrease in the saturated orientation degree.

5.3.3 Laminated Green and Sintered Samples

Figure 5.6 shows XRD patterns of laminated SCNN green compacts prepared for a duration time of 150 s with and without the magnetic field after spreading the slurry on the PET film using the spin coater. As a reference, the green body prepared by the conventional forming process (consolidated by evaporation of a solvent) was evaluated. The measured planes were the top surface of samples. The intensities of the peaks from

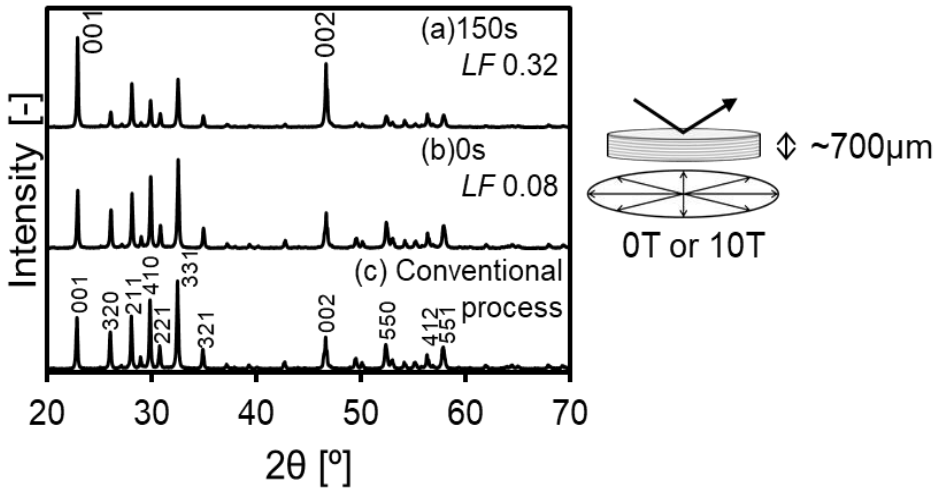

FIGURE 5.6 X-ray diffraction patterns obtained from top surface of multilayer green compacts prepared for duration time of 150 s (a) with and (b) without the rotating magnetic field at 10 T after spreading the slurry on the PET film by using the spin coater, and (c) a powder compact prepared by conventional forming without the magnetic field.

c-planes in the compacts prepared with the rotating magnetic field for 150 s enhanced. Interestingly, for the sample prepared without the magnetic field after spreading a slurry on the PET film by the spin coater, the peaks from the *c*-plane were slightly high. This tendency is the same as the monolayer sheets.

The sintered samples were examined by SEM. Preparing by the SL process, the laminated samples go through the de-binding process due to remove the cured resin surrounding particles. In this stage, the laminated structure between layers or/and cracks tend to be observed [10,11]. Figure 5.7 shows SEM images of the pre-sintered sample heated at 1150 °C observed from the perpendicular directions to the rotating axis of the spin coater. The thickness of the pre-sintered multilayer was about 700 μm. Although a laminated structure was observed, the microstructure in the layer was uniform. Figure 5.8 shows the structures of the sintered sample heated at 1240 °C observed from the perpendicular directions to the rotating axis of the spin coater. The sample thickness shrank from ~700 μm to ~600 μm by sintering and observed a continuous structure. This result indicates that the layers are contiuous during sintering.

Figure 5.9 shows XRD patterns of the top surface of the sintered samples obtained by the sintering of the laminated green compacts and of the random green body. The Lotgering factor *LF* of the sample cured after a duration time of 150 s in the rotating magnetic field was 0.69. In addition, the *LF* value of the sample prepared without applying the magnetic field after using the spin coater was 0.22. The results indicated that *c*-axis oriented SCNN ceramics were produced by sintering of the particle-oriented laminated bodies fabricated by the spin coating and applying the magnetic field.

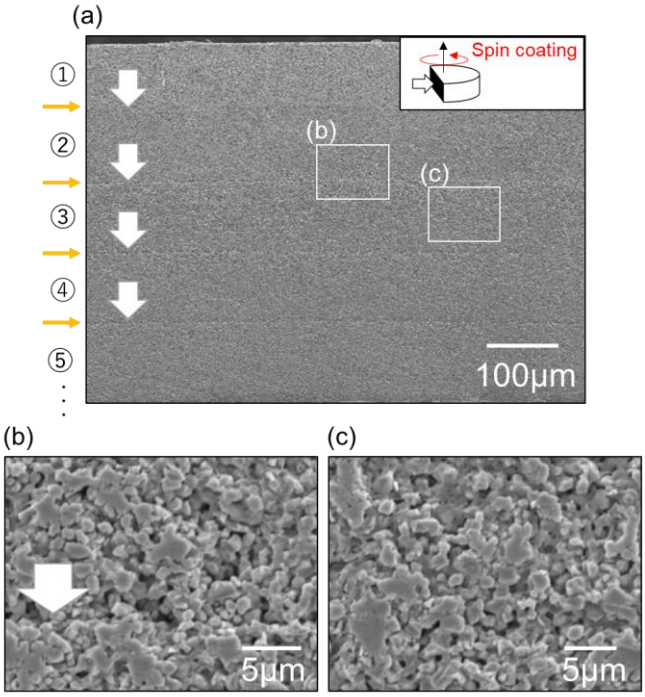

FIGURE 5.7 SEM images of the pre-sintered sample heated at 1150 ºC observed from the perpendicular directions to the rotating axis of spin coater. (a) × 200 and (b), (c) × 5,000.

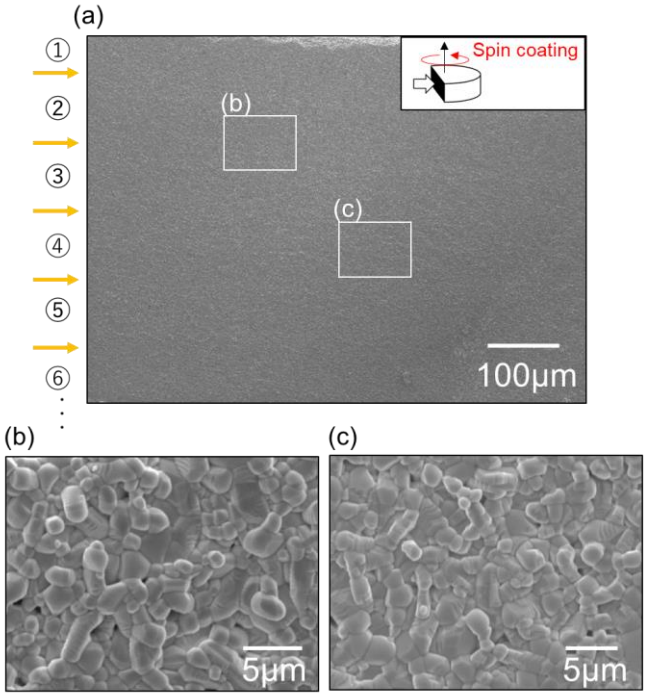

FIGURE 5.8 SEM images of the sintered sample heated at 1240 ºC observed from the perpendicular directions to the rotating axis of spin coater. (a) × 200 and (b), (c) × 5,000.

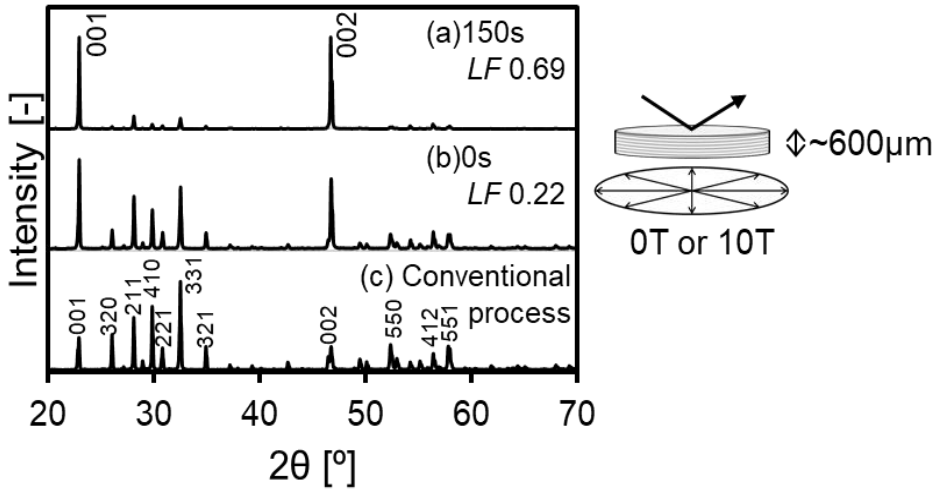

FIGURE 5.9 X-ray diffraction patterns obtained from top surface of sintered compacts prepared for duration time of 150 s (a) with and (b) without the rotating magnetic field at 10 T after spreading the slurry on the PET film by using the spin coater, and (c) a sintered body prepared by conventional forming process without the magnetic field.

Figure 5.10 shows SEM micrographs of the microstructure of the sintered ceramics observed from the parallel and perpendicular directions to the rotating magnetic field. These are the microstructures of the sintered samples with *LF* value of 0.69, 0.22 and randomly oriented. A significant difference was noted in the structures observed from the two directions of the *c*-axis oriented sintered ceramics (Figs. 5.10 (a)-(d)). The grains grew parallel to the rotating axis of the magnetic field and of the spin coating, which is corresponding to the *c*-axis of crystal direction. The results are the same as that in Chapters 2 and 4.

Figure 5.11 shows band contrasts and EBSD maps of samples prepared with and without the rotating magnetic field. The samples were observed perpendicular to the rotating magnetic field, which corresponds to the *c*-axis direction for the sample prepared with the rotating magnetic field. From the band contrasts, the grain size was observed the same as the SEM micrograph. In EBSD maps, various colors presented crystal direction in each region, which was identified by Kikuchi patterns, whereas unidentified regions were shown as black areas. These black areas regions were almost grain boundary. The difference in the crystal direction in the samples can be clearly observed. Misoriented particles were expressed in violet, green, or yellow, were present in the sample prepared without the magnetic field, as shown in Figs. 5.11 (d) and (f). Figure 5.11 (b) shows that almost the grains appeared to red, indicating that almost particles were aligned along the [001] direction.

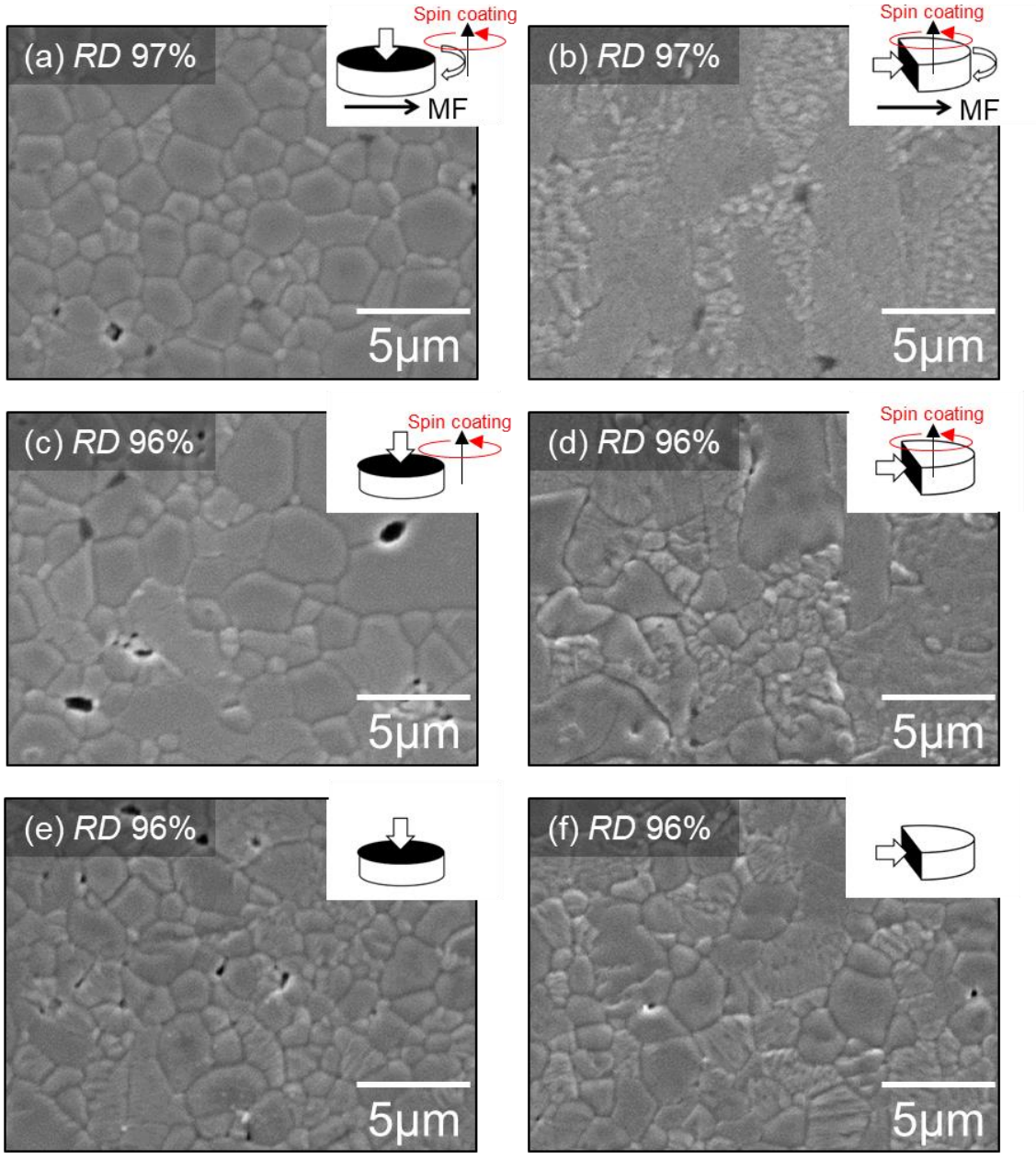

FIGURE 5.10 Microstructure of sintered SCNN ceramics at 1240 ºC for 2 h observed from the (a, c and e) perpendicular and (b, d and f) parallel directions. These are the microstructures of the samples with (a and b) *LF* 0.69, (c and d) *LF* 0.22 and (e and f) randomly oriented.

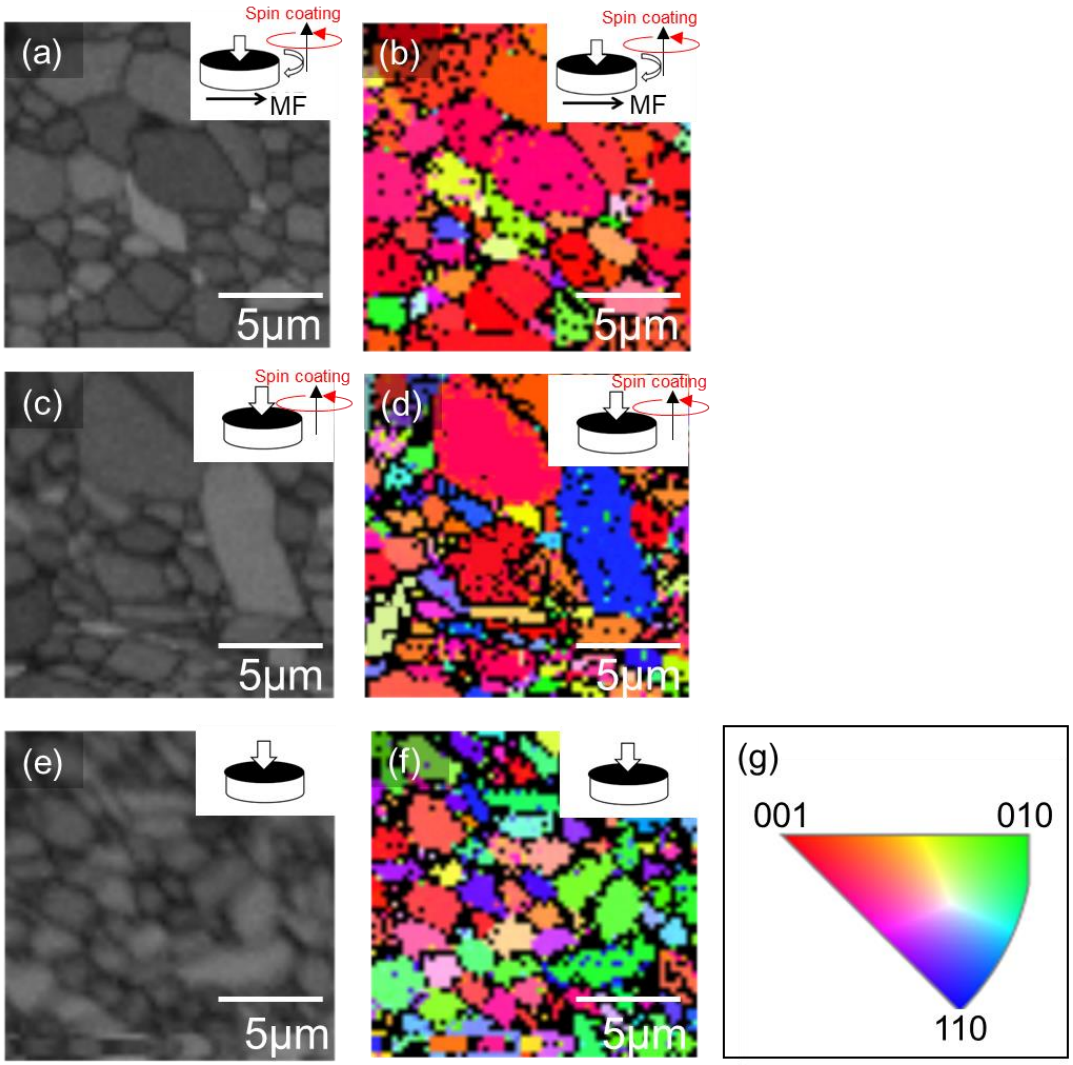

FIGURE 5.11 Band contrast and EBSD map of sintered SCNN ceramics at 1240 ºC for 2 h, which are (a and b) *LF* 0.69 (c and d) *LF* 0.22, and (e and f) randomly oriented samples, observed from parallel to the rotating axis of spin coater. (a, c and e) band contrasts, (b, d and f) EBSD maps of x-direction and (g) stereographic triangle.

5.3.4 Piezoelectric Properties

Figure 5.12 presents the *P*-*E* hysteresis loops of the *c*-axis oriented and random oriented SCNN ceramics. Hysteresis is noticeable in the samples with an oriented structure. In a highly oriented sample, as the applied electric field increases, the residual polarization increases and the hysteresis property becomes remarkable. (Figure 5.12(a)). The values of saturated polarization also enhanced with the orientation degree. At the applied electric field of 40 kV/cm, the saturated polarization was 19.5 μC/cm^2 for the *c*-axis oriented sample with *LF* of 0.69, higher than the 9.3 μC/cm^2 measured for the random sample. The coercive field did not change much with the oriented microstructure. This is probably because the orientation is not so high.

Table 5.1 shows the values of *LF*, relative density (*RD*) and piezoelectric d_{33} constant for each sample. The relative density was almost the same value. The d_{33} value measured for the *c*-axis oriented sample was 74.4 pC/N and approximately six times as high as that of the randomly oriented structure, 12.8 pC/N. The piezoelectric d_{33} constant improved with increasing *c*-axis orientation. Thus, the ferroelectric and piezoelectric properties along to *c*-axis were increased by the oriented structure. This tendency was the same as previous reports [13]-[15]. However, the piezoelectric d_{33} constant of 74.4 pC/N was considerably lower than that of a single crystal, 270 pC/N [16,17]. It is difficult to saturate the polarization of SCNN ceramics due to a low insulation property. In point of fact, multivalent ions as dopants are known to be effective in insulating properties[16]-[18], and this sample is expected to improve as well.

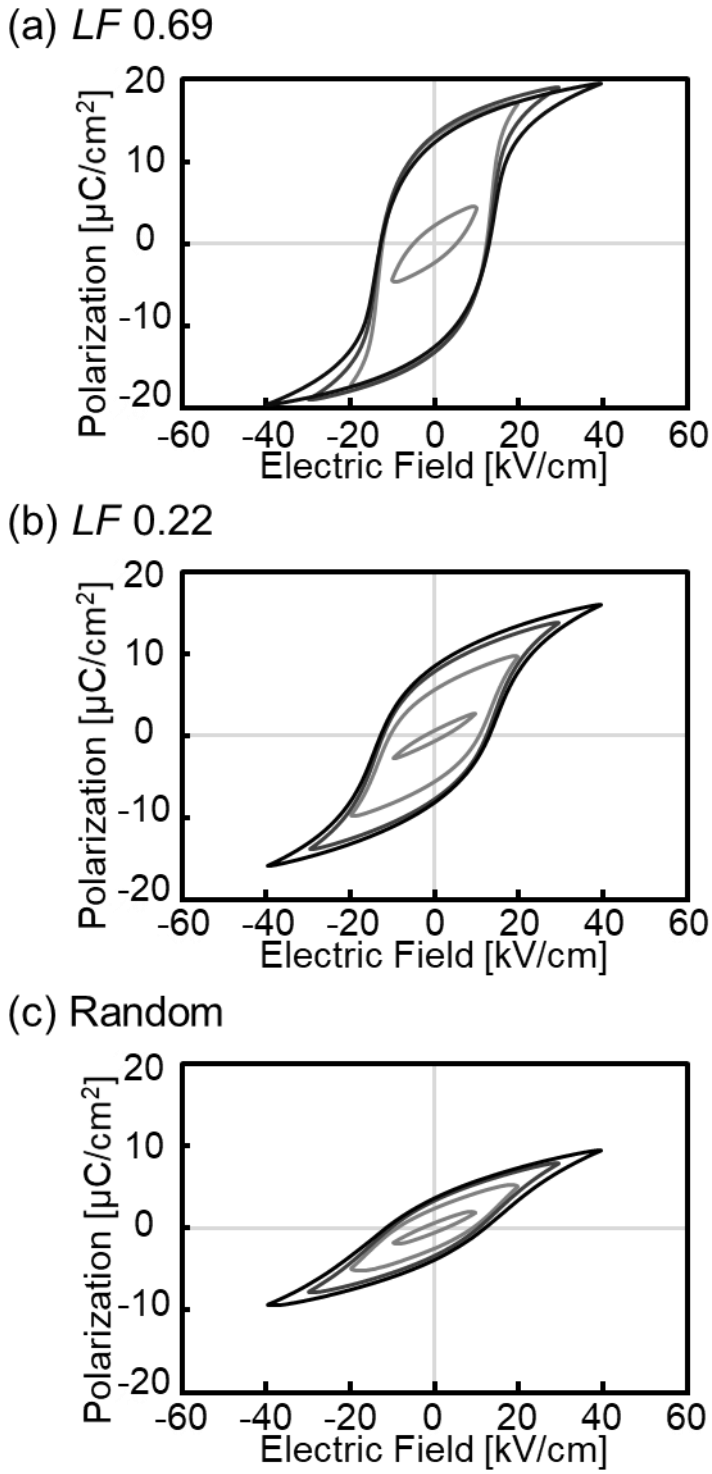

FIGURE 5.12 The *P-E* hysteresis loops measured from sintered SCNN ceramics, which are (a) *LF* 0.69, (b) *LF* 0.22 and (c) randomly oriented sample. Measured direction was along the parallel to the rotating axis of spin coater.

TABLE 5.1 Lists the values of *LF*, relative density *RD* and piezoelectric d_{33} constant for sintered samples prepared by the various forming process.

Forming process	*LF*	*RD*	d_{33}(pC/N)
Conventional process (evaporation of solvent)	-	96	12.8
Spin coating	0.22	96	26.9
Spin coating + Magnetic field for 150s	0.69	98	74.4

5.4 CONCLUSIONS

The photopolymerization reactions in the magnetic field were repeatedly performed to fabricate *c*-axis oriented SCNN piezoelectric bulk ceramics. The technique can prepare the *c*-axis laminated green compacts. Here, spin coating was performed, and the particles were found to be aligned not only by the applied magnetic field, but also by the shear stress generated by the spin coating. The laminate structure was clearly observed in the sample before sintering, while a continuous and homogeneous microstructure was obtained after sintering at 1240 °C. The *c*-axis oriented SCNN ceramics have a piezoelectric constant, d_{33}, 74.4 pC/N, about 6 times higherr than the 12.8 pC/N measured from the randomly oriented sample. It became clear that the piezoelectric properties of crystal-oriented ceramics prepared by the photopolymerization reaction could be improved. This result demonstrates that the repeat of a photopolymerization reaction in the magnetic field and followed by sintering are one of the beneficial techniques to fabricate particle-oriented piezoelectric ceramics.

REFERENCES

[1] C. Hull, U. S. Pat. No. 4575330, 1986
[2] M. L. Griffith and J. W. Halloran, J. Am. Ceram. Soc., 79[10] (1996) 2601-2608
[3] C. Hinczewski, S. Corbel and T. Chartier, J. Eur. Ceram. Soc., 18 (1998) 583-590
[4] T. Chartier, C. Chaput, F. Doreau and M. Loiseau, J. Mater. Sci.,37 (2002) 3141-3147
[5] C. Sun and X. Zhang, Sens. Actuators, 101 (2002) 364-370
[6] T. Chartier, C. Duterte, N. Delhote, D. Baillargeat, S. Verdeyme, C. Delage and C. Chaput, J. Am. Ceram. Soc., 91[8] (2008) 2469-2474
[7] X. N. Jiang, C. Sun, X. Zhang, B. Xu and Y. H. Ye, Sens. Actuators, 87 (2000) 72-77
[8] D. I. Woodward, C. P. Purssell, D. R. Billson, D. A. Hutchins, and S. J. Leign, Phys. Status Solidi A, 212[10] (2015) 2107-2113
[9] W. Chan, F. Wang, K. Yan, Y. Zhang, and D. Wu, Ceram. Int., 45 (2019) 4880-4885
[10] C. J. Bae, and J. W. Halloran, Int. J. Appl. Ceram. Technol., 8[6] (2011) 1289-1295
[11] E. Johansson, O. Lidstrom, J. Johansson, O. Lyckfeldt, and E. Adolfsson, Materials, 10 138 (2017) doi:10.3390
[12] H. Yoshiba, Y. Komoda, H. Imakoma and H. Usui, J. Soc. Rheol., 33[5] (2005) 279-283
[13] R. J. Xie, Y. Akimune, R.P. Wang, and N. Hiroaki, J. Am. Ceram., 85[11] (2002) 2731-2737
[14] L. Wei, X. Chao, X. Han and Z. Yang, Mater. Res. Bull., 52 (2014) 65-69
[15] H. Shimizu, Y. Doshida, S. Tanaka, and K. Uematsu, Key. Eng. Mater., 421-422 (2010) 21-25
[16] R. R. Neurgaonkar, W. K. Cory, J. R. Oliver, E. J. Sharp, G. L. Wood, M. J. Miller, W. W. Clark and G. J. Salamo, Mat. Res. Bull., 23 (1988) 1459-1467
[17] R. R. Neurgaonkar, J. R. Oliver, W. K. Cory, L. E. Cross and D. Viehland, Ferrolelectrics, 160 (1994) 265-176
[18] Y. Doshida, H. Shimizu, Y. Mizuno, K. Itoh, S. Hirose and H. Tamura, Jpn. J. Appl. Phys., 50 (2011) 09ND06

Chapter 6

Fabrication of *C*-axis Oriented Hydroxyapatite Ceramics in Rotating Magnetic Field using Photopolymerization Reaction

6.1 INTRODUCTION

Colloidal processing with a photopolymerization reaction in a magnetic field was studied in this thesis. This novel colloidal technique under the magnetic field is expected to be widely applicable to many types of materials. In this chapter, crystal-oriented bulk green compacts were fabricated by once polymerization reaction in the magnetic field. I focused on hydroxyapatite ($Ca_{10}(PO_4)_6(OH)_2$; referred to as HAp) material system.

HAp has been used for implant materials such as bones and teeth because it has an excellent compatibility with the human body [1]-[3]. HAp has two major crystal planes, *a,b*-plane and *c*-plane. Each crystal plane exhibits different properties with respect to adsorption of biological substances such as proteins and amino acids, the ion-exchange, and in the mechanical properties, respectively [4]-[9]. In order to exhibit each functionality, it is necessary to adopt an appropriate crystal orientation. Asai et al. had reported the fabrication of crystal-oriented HAp ceramics by colloidal processing in the presence of a magnetic field and subsequent sintering [10,11]. The diamagnetic susceptibility of HAp crystal axes exhibits the relation $\chi_c < \chi_{a,b} < 0$; hence, the *a,b*-axes aligns parallel to the magnetic field [10]. The *c*-axis is oriented along the rotational axis by rotating the sample at a specific orientation to the magnetic field direction [11].

The objective in this chapter was fabrication of bulky c-axis oriented HAp ceramics by one polymerization reaction in a rotating magnetic field. The refractive index of HAp particle is only slightly different (Δn) from the refractive index of UV curable binder. The thickness of polymerized slurry was expected to depend on the refractive index difference (Δn). The curing behavior of the slurry and the internal structure of the green body were investigated. The key techniques were to prepare the slurry at a high solid concentration and to fabricate the green compacts having a uniform structure.

6.2 EXPERIMENTAL PROCEDURE

6.2.1 Materials

The HAp powder (HAP-200, Taihei Chemical Industrial Co. Ltd., Japan) was used in this chapter. This raw powder was ground by ball milling for 48h in an azeotropic mixture solvent consisting of methyl ethyl ketone (MEK) and ethanol (EtOH) (60/40 vol.). A zirconia ball having a diameter of 2.0 mm was used.The solvent was evaporated in an oven at 45 ºC for 3 h. The morphology of the raw powder and the ground powder were observed using a scanning electron microscope (SEM, JSM-5310LVB, JEOL Tokyo, Japan). The particle size distribution was determined by the sedimentation method (Sedigraph 5100, Micrometrics, USA). The powder was dispersed in deionized water with 0.025 wt% sodium hexametaphosphate as the dispersing agent.

An UV-curable resin was used as the dispersion medium and containing polyether acrylate monomer diluted in hydroxyethyl methacrylate was used as the dispersion medium and a 2.7 wt% of 2-hydroxy-2-methyl-1-phenylpropan-1-one was used as the photoinitiator. A phosphate ester with 1.2 wt% was used as the dispersant.

6.2.2 Slurry Preparation and Characterization

At first, the photoinitiator and the dispersant were completely dissolved in the UV curable acrylate binder, and then, the ground HAp powder was added to the binder. The volume fraction of the HAp powder was varied between 30 and 50 vol%. The slurry was treated in an ultrasonic bath for 5 min and was stirred by a planetary centrifugal mixer (Awatorirentaro. Are310, Thinky, Tokyo) with the defoaming mode at 2000 rpm for 30 s and by the thin-film spin system high-speed mixer (FILMIX Model30-L, PRIMIX Co. Japan) at 500 rpm for 5 min and at 1000 rpm for 5 min. The mixing treatment was performed at a temperature of 40 °C. Finally, the slurry was de-aired by the planetary centrifugal mixer with the deforming mode at 2000 rpm for 30 s.

The viscosity of the binder mixture and the slurry was measured by a rheometer (Physica MCR301, Anton Paar, Austria) using a cone and plate apparatus (CP25-2) in the stress-controlled mode. The shear rate was varied from 0.001 s^{-1} to 100 s^{-1}. The measurement temperature was set to 20 °C. The slurry viscosity was characterized by fitting with the Cross model following Eq. (3.3) using the nonlinear least-squares method.

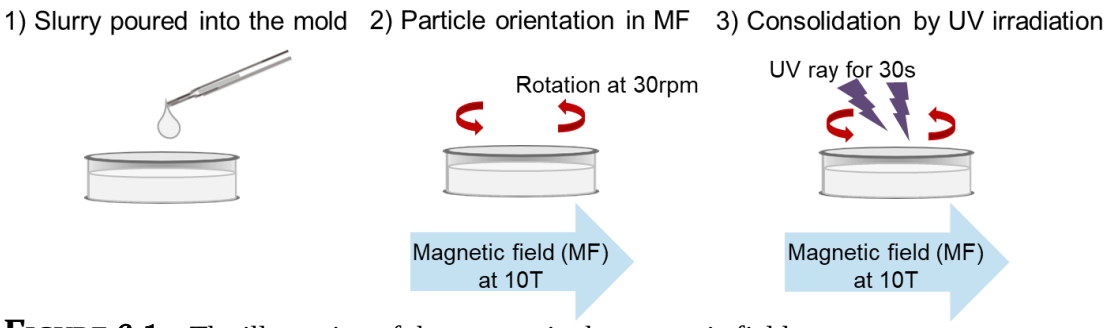

FIGURE 6.1 The illustration of the process in the magnetic field

6.2.3 Fabrication of Polymerized Green Compacts and Sintering

After keeping the slurry in a thermostatic bath at 20 °C for 1 h, slurry was poured into a mold, and the mold was rotated horizontally at 30 rpm in a magnetic field of 10T induced by a superconducting magnet (TM-10VH10, TOSHIBA Co. Japan) spanning from 5 s to 300 s (Figure 6.1). After holding the slurry in the magnetic field for a specified period of time, the slurry was exposed to UV irradiation in the magnetic field for 30 s (i.e., E = 10.8 J/cm^2). For comparison, another sample from the slurry was also exposed to UV irradiation for 30 s without a magnetic field.

After demolding, the binder was removed from the polymerized compacts. The temperature was raised to 100 °C at a heating rate of 0.5 °C/min and to 500 °C at a heating rate of 0.3 °C/min, and then held for 2 hours. The powder compacts after bider-removal were sintered. The sintering temperature was 1000 °C to 1250 °C. The holding time was 2 hours, and the heating rate was 5 °C/min.

6.2.4 Characterization of Green and Sintered Samples

The thickness of the polymerized samples was measured with a micrometer to examine the cured depth of the slurry. The crystal orientations of the surfaced and inside of the powder compact and ceramic were evaluated by X-ray diffraction (XRD) analysis (Ultima-IV, RIGAKU Japan). The degree of *c*-axis orientation was evaluated in terms of the Lotgering factor *LF* of [00*l*] orientation, as described in Section 2.2.4. The interior of the polymerized compacts was examined by whittling 100 μm from the bottom of the polymerized sample. Rocking curves of the 004 reflections for each green body were also measured in order to confirm the orientation distribution and to relate the *LF* value with the orientation degree. The multiple of a random distribution (MRD) was calculated and characterized by fitting with the March-Dollase function containing a texture volume

fraction *f* as follows Eq. (3.4). The detail of the operation condition was described in Section 3.3.2. The microstructures of the cross-section of the sintered samples were observed by SEM. All polished sintered bodies were thermally etched at 1100 °C for 15 min and coated with gold for SEM observation. The relative density (*RD*) of the sintered sample was measured using the Archimedes method.

6.3 RESULTS AND DISCUSSION

6.3.1 HAp Powder and Slurry

Figure 6.2 shows SEM images of the raw and ground HAp powder. The majority of the powders were found to be cylindrical. The agglomerates of particles were included in the raw powder. After ball milling, the particle de-agglomerated and the particle size was reduced to micro. The size of the ground particles was between 0.3 to 1 μm.

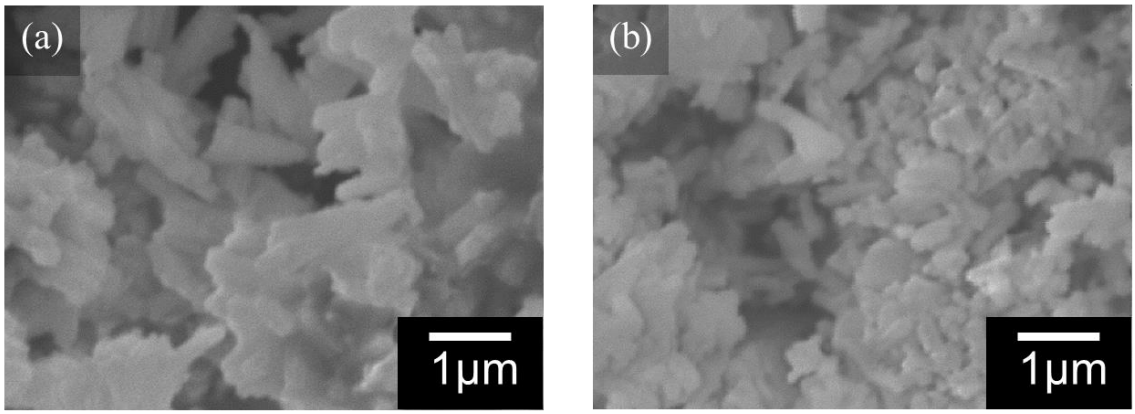

FIGURE 6.2 SEM images of (a) raw powder and (b) ground powder.

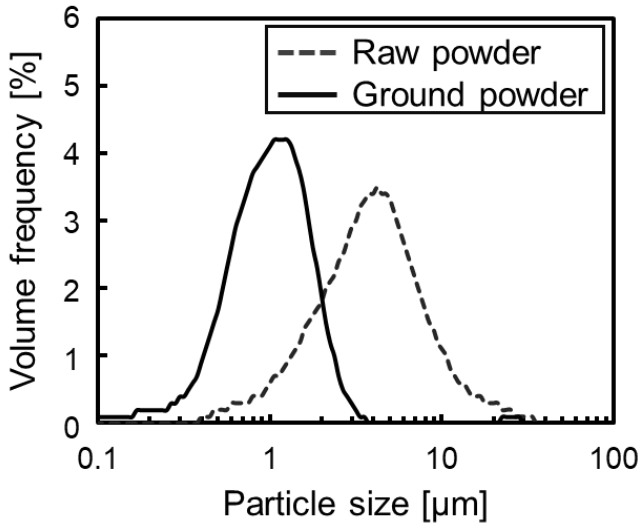

FIGURE 6.3 Particle size distribution of HAp raw powder and ground powder.

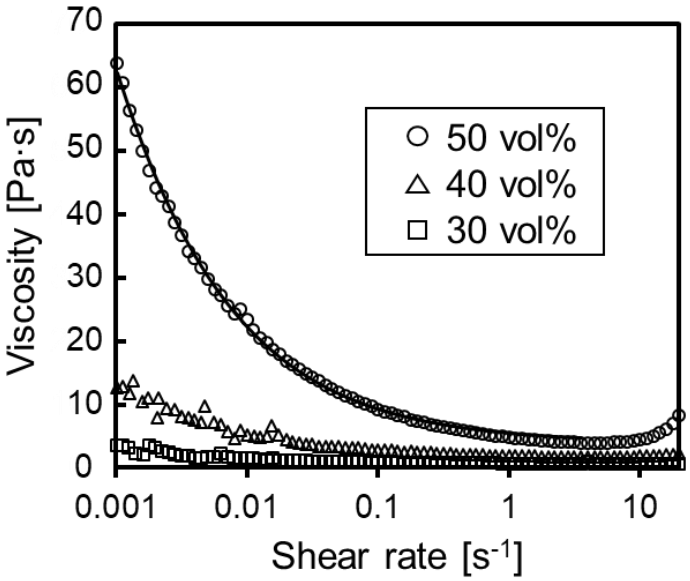

FIGURE 6.4 Shear viscosity of a slurry HAp powder, UV curable resin, dispersant, and photoinitiator at 20 °C. The solid contents are varied between 30 and 50 vol%. The solid lines are the fitted curves with Cross model Eq. (3.3).

Figure 6.3 shows the particle size distributions of the raw and ground powders. The large agglomerated powders found in the raw powder were absent in the ground powder.

Figure 6.4 shows the viscosity curves of the slurry versus the shear rate at solid concentration of 30, 40, and 50 vol%, respectively. The viscosity increased with an increase in solid content. Although slight shear-thinning was observed for the 50 vol% slurry, the HAp slurry with a high solid content can be prepared using the UV curable binder. The solid lines are the curves fitted with the Cross model represented in Eq (3.3). Fitting the curve for the 50 vol% slurry with the Cross model yielded a value of 491 Pa·s for η_0.

6.3.2 Cured Depth of Slurry

Figures 6.5 (a) and (b) show the cured depth of the HAp slurry containing 50 vol% powder, and the photographs of the polymerized green compacts, as a function of UV irradiation time. The cured depth of the slurry increases with increasing UV irradiation time. After irradiation for 30 s (E = 10.8 J/cm^2), the cured depth of the HAp slurry is about 1.6 mm. Thus, a thick HAp compact could be fabricated by a photopolymerization reaction. For comparison, the cured depth of the slurry with 50 vol% $(Sr,Ca)_2NaNd_5O_{15}$ (SCNN) is also plotted in Fig. 6.5(a). After exposure to the SCNN slurry to UV for 30 s, the thickness of the polymerized sample was approximately 0.1 mm. The cured depth of the HAp slurry

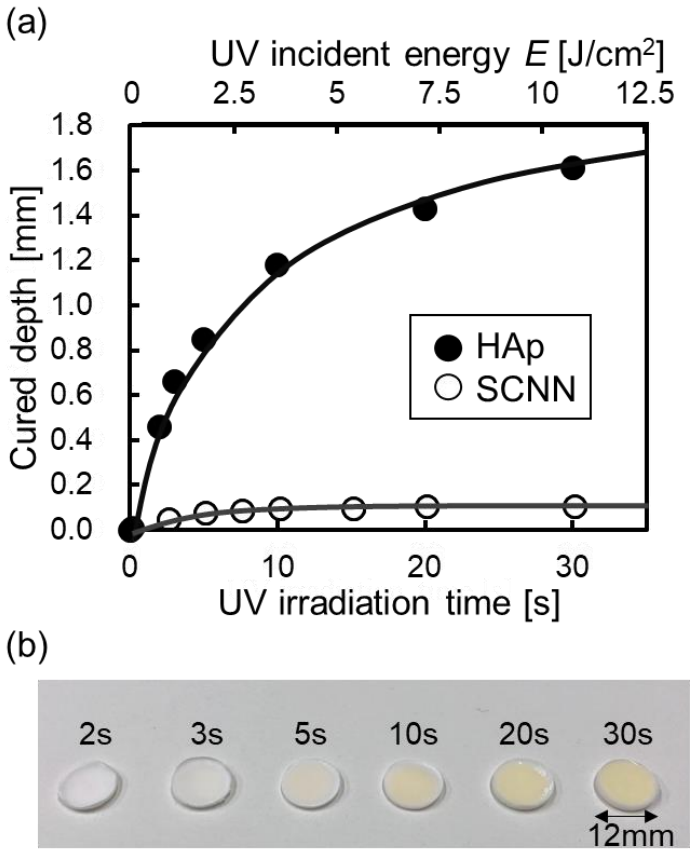

FIGURE 6.5 (a) The cured depth of the slurries containing 50 vol% HAp (filled symbol) and SCNN (open symbols) powder, respectively, and (b) the photographs of the polymerized green compact containing 50 vol% HAp powder.

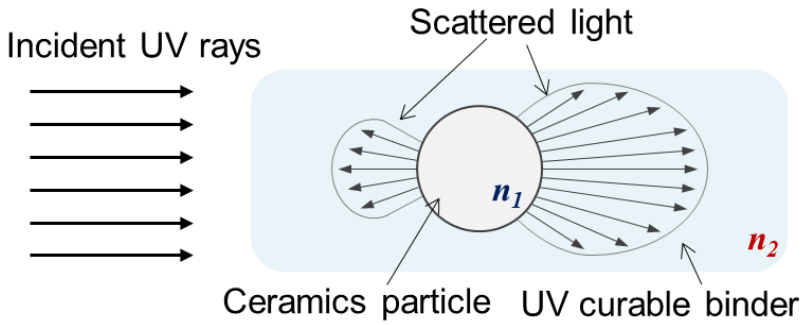

FIGURE 6.6 Scattering of ceramics particle in a UV curable binder.

was approximately 16 times larger than that of the SCNN slurry.

Some researchers have investigated the cured depth of UV photocurable systems and found a theoretical expression deduced from the Beer-Lambert law and is given by: [12-15]

$$C_d \propto \frac{d}{\Phi}\frac{1}{Q}\ln\left(\frac{E}{E_c}\right) \qquad (6.1)$$

where d is the mean ceramic particle diameter, Φ is a function of the volume fraction of ceramic powder, Q is the material scattering ability which has been first described by the Rayleigh-Gans or Mie theories (Figure 6.6) [12]-[14], E (J/cm^2) is the exposure energy and E_c (J/cm^2) is the critical exposure or the minimal exposure energy to provide polymerization of the UV binder. Here, the absorption of UV radiations by particles can be ignored, because the extinction coefficient e of photoinitiator in the UV ray range is much greater than the particle's one. Recently, Q was written as an empirical equation for the highly concentrated slurry: [12,13]

$$Q = \frac{S}{\lambda}(\Delta n)^2 \qquad (6.2)$$

where S is the interparticle spacing and Δn is the difference of the refraction index between the ceramic particle (n_1) and the UV curable binder (n_2). According to Eqs. (6.1) and (6.2), the cured depth largely depends on the difference of refractive index between the particles and the solvent. The refractive indices of HAp, SCNN, and photocurable binders are 1.64, 2.3, and 1.45, respectively. On the basis of Eq. (6.2), Q is higher by a factor of 20 for the SCNN slurry relative to HAp, which is similar to the difference between the experimental C_{sca} values. This result indicates that the cured depth of the obtained sample is associated with the scattering of the UV ray by the particles in the UV binder.

6.3.3 Characterization of Polymerized Powder Compacts

Figure 6.7 shows XRD patterns of the polymerized green compacts with 50 vol% solids fabricated in the magnetic field for 0 s to 150 s. For all samples prepared with a magnetic field, the intensity of the *c*-planes (i.e., 002 and 004) was enhanced relative to the samples prepared without a magnetic field. The longer the sample exposure to the magnetic field before consolidation with UV irradiation, the higher the intensities of the *c*-plane peaks. In contrast, the XRD patterns of the samples produced without the magnetic field matched with the International Centre for Diffraction Data (ICDD) card No. 01-072-1243 for

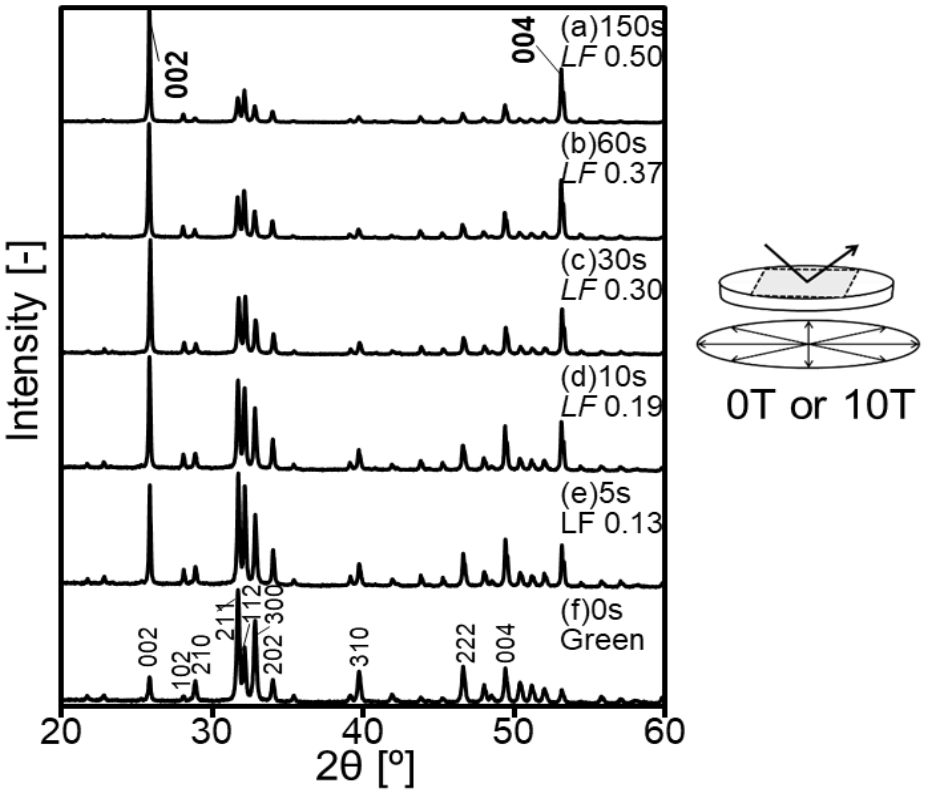

FIGURE 6.7 X-ray diffraction patterns obtained from green compacts with a solid concentration of 50vol% for various durations of (a) 150 s, (b) 60 s, (c) 30 s, (d) 10 s and (e) 5 s (a - e) with and (f) without a 10 T rotating magnetic field.

$Ca_{10}(PO_4)_6(OH)_2$. The *LF* of the oriented samples increased gradually with increasing processing time under the magnetic field.

Figure 6.8 shows the rocking curves (MRD) of the 004 peaks for these samples. The solid curves fitted by Eq. (3.4) are also shown. The intensity of the peak increased with increasing the duration time in the magnetic field. Table 6.1 shows the *LF*, *FWHM*, the *r* parameter, and the textured fraction *f* for these samples. The *r* parameter decreased as the processing time increased. There was no correlation between the textured fraction *f* and the processing time in the magnetic field.

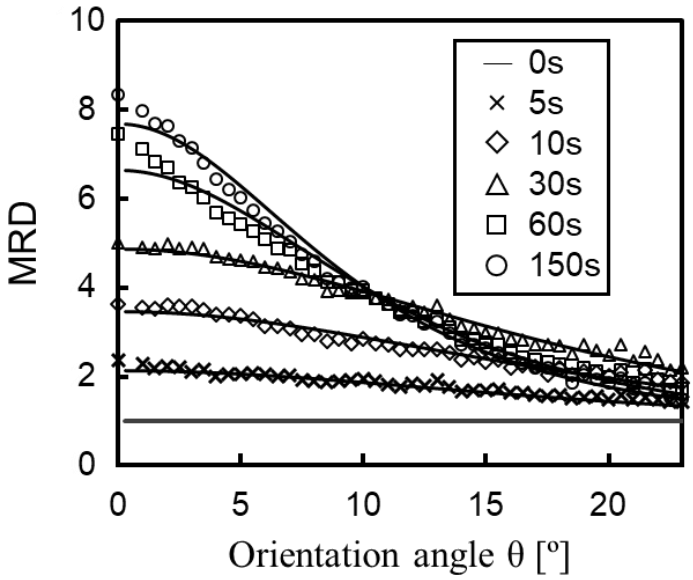

FIGURE 6.8 Rocking curves, MRD of particle-oriented HAp samples with a solid concentration of 50 vol% for various durations with a 10 T rotating magnetic field. The solid lines are fitted curves with March-Dollase function Eq. (3.4).

TABLE 6.1 Full-width at half-maximum (FWHM), Lotgering factor (*LF*), orientation parameter *r* and textured fraction *f* for each processing time

Processing time[s]	*LF*	FWHM[°]	Orientation parameter (*r*)	Textured fraction (*f*)
5	0.13	30.4	0.546	0.218
10	0.19	29.6	0.541	0.465
30	0.30	29.8	0.534	0.695
60	0.41	21.2	0.394	0.367
105	0.46	20.0	0.356	0.315
150	0.48	19.2	0.326	0.222

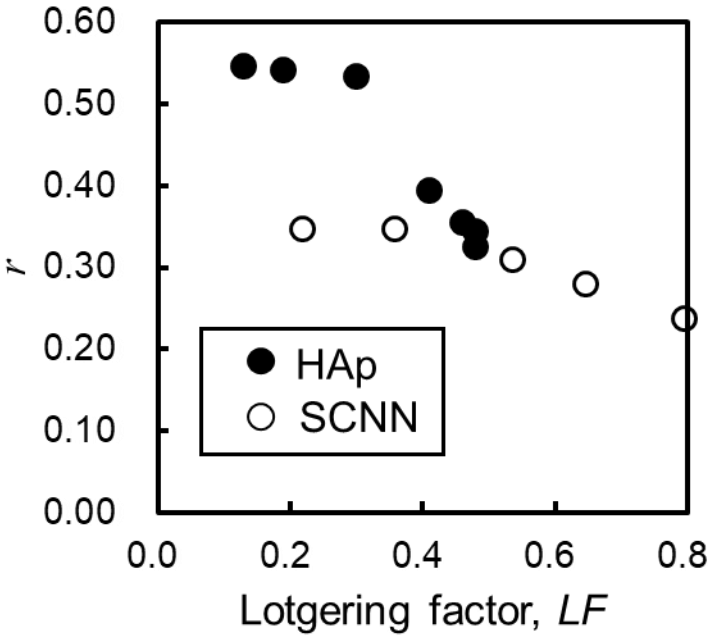

FIGURE 6.9 The correlation between *LF* calculated from the X-ray diffraction (XRD) pattern and parameters *r* determined by fitting March-Dollase function to the MRD in particle-oriented HAp bodies (filled symbols) and SCNN sheets (open symbols).

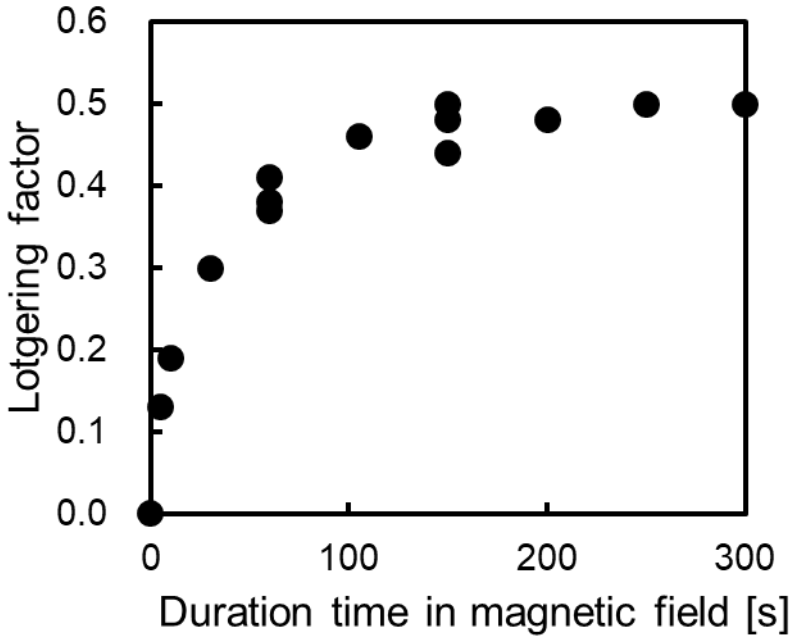

FIGURE 6.10 The orientation degree of prepared by various duration times in rotating magnetic field of 10 T at 20 ºC. The solid content in the slurry is 50 vol%.

Figure 6.9 shows the correlation of *LF* versus the *r* parameters. When the values of *LF* are distributed in the range of 0.1 - 0.5, the linear correlation between *LF* and the parameter *r* was observed. Though *LF* is an equivocal parameter, this result indicates that it is adequate to quantitively estimate the degree of orientation for HAp. However, the results suggested that the *LF* in the range of 0.1 – 0.4 in *c*-axis oriented HAp green bodies is sensitive in comparison with that in *c*-axis oriented SCNN green sheets.

Figure 6.10 shows the relationship between the duration kept in the magnetic field and the degree of orientation, *LF*, for the green compacts prepared in the magnetic field of 10T. The degree of orientation clearly depends on the duration time in the magnetic field and saturated at 150 s. Here, the intrinsic magnetic response rate τ^{-1} and orientation time t of the particles in the rotating magnetic field were calculated from the viscosity at zero shear rate and at a magnetic flux density of 10T. We previously reported that τ^{-1} and *t* could be calculated from the viscosity of the slurry and the magnetic flux density, as investigated in Chapter 3. The values of τ^{-1} and *t* calculated from Eqs. (3.1) and (3.2) were 0.0168 s^{-1} and 125 s, respectively. The value used for the $\Delta\chi$ of HAp is 1.24×10^{-6} [11]. The established orientation time calculated from the viscosity of the slurry and the magnetic flux density was very similar to the experimental values obtained from the XRD data.

Figure 6.11 shows XRD patterns of the samples from the interior bulk of the polymerized green compacts after orientation in the magnetic field, followed by photopolymerization. The thickness of the samples was (a) 1500 μm and (b) 800 μm, respectively. A homogeneously oriented structure in the polymerized compacts was obtained from the sample having 700 μm thickness, which was polished from the bottom side. For both the samples, moving from the region of 700 μm thickness to the UV exposed top surface, the intensity of the (002) and (004) peaks gradually decreased. This result indicates that oriented particles were fluctuated again by the convection in the slurry, which as induced by the exothermic reaction due to the polymerization reaction of the UV curable binder. The effect of the binding force from the mold on the oriented particles was not observed. Figure 6.12 shows SEM images of the released sample heated at 1000 °C, observed from the direction parallel to the magnetic field. The thickness of this sample is ~800 μm. In the part near to the UV exposed surface and in the middle, the cylindrical particles align perpendicular to the magnetic field. On the other hand, a randomly oriented particle exists in the bottom part.

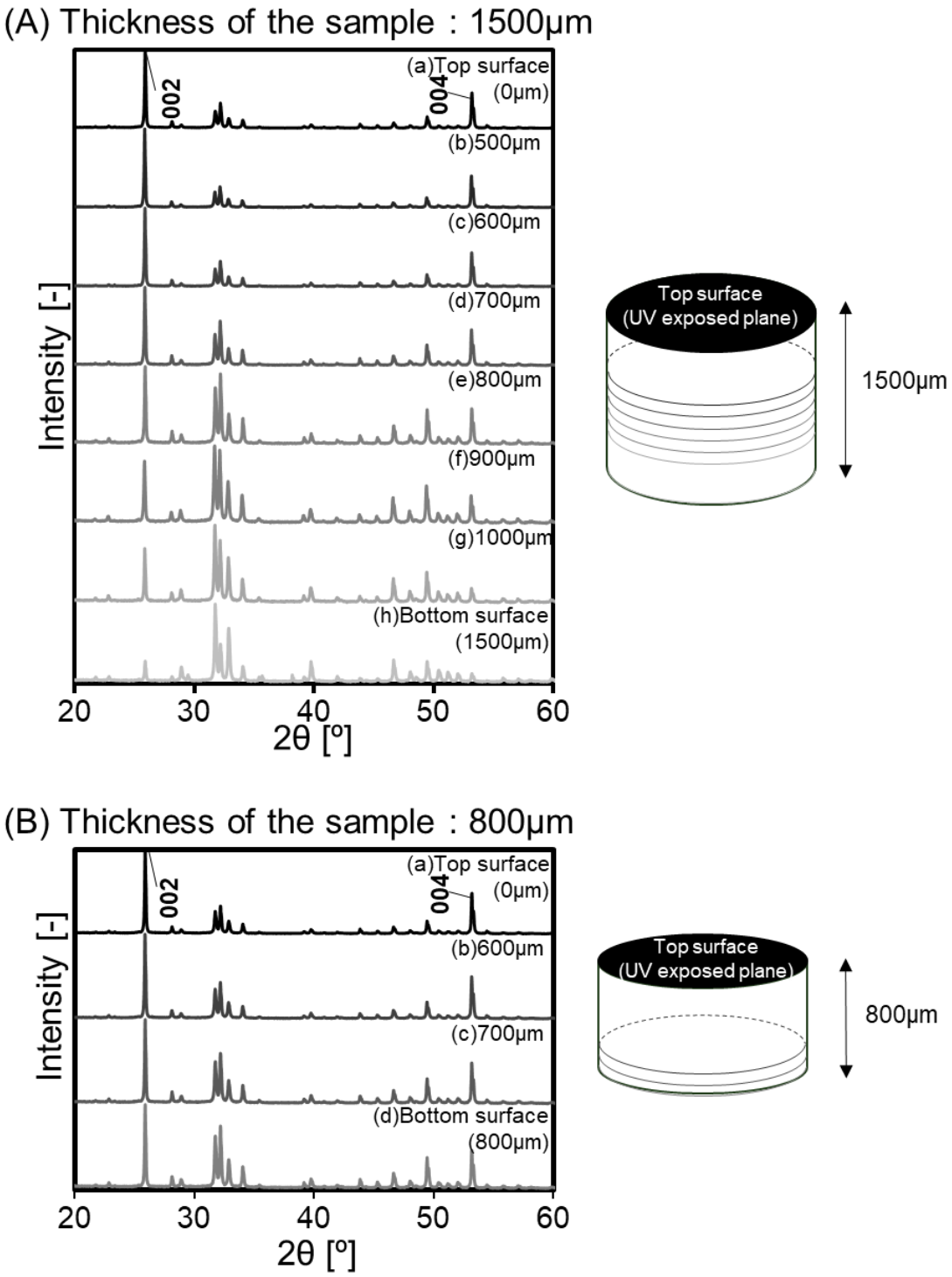

FIGURE 6.11 X-ray diffraction patterns obtained from green compacts with a solid concentration of 50 vol% for 150 s with a 10 T rotating magnetic field. The thickness of polymerized powder compacts were (A) 1500 μm and (B) 800 μm, respectively.

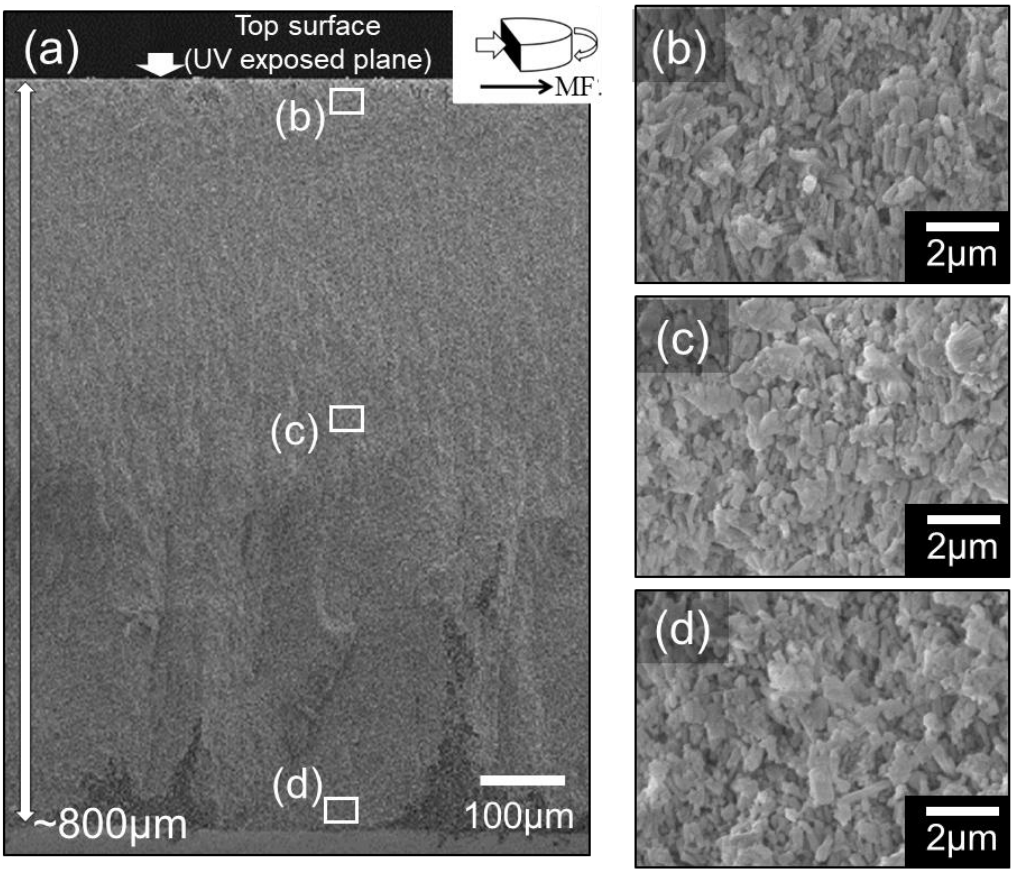

FIGURE 6.12 SEM images of the de-binded sample heated at 1000 ºC observed from the parallel direction to the magnetic field. (a) ×150 and (b), (c) and (d) ×7,500. The thickness of the sample is ~800 μm.

6.3.4 Microstructure Development during Sintering

Figure 6.13 shows SEM images of the sintered sample heated at 1000 °C and 1250 °C. The thickness of the sample heated at 1000 °C was approximately 700 μm. After sintering at 1250 °C, the sample dramatically shrunk to approximately 550 μm, with a uniform structure.

Figure 6.14 shows SEM images of the microstructure of the sintered ceramics observed from the direction parallel to the rotation axis. The duration time in the magnetic field is 150s. At 1000 °C, the cylindrical particles aligned the perpendicular direction to the magnetic field. At the temperature from 1150 °C to 1250 °C, the grain grew isotropically with the progress of densification. For the sample sintered at 1250 ºC, relative density (*RD*) was 97 %.

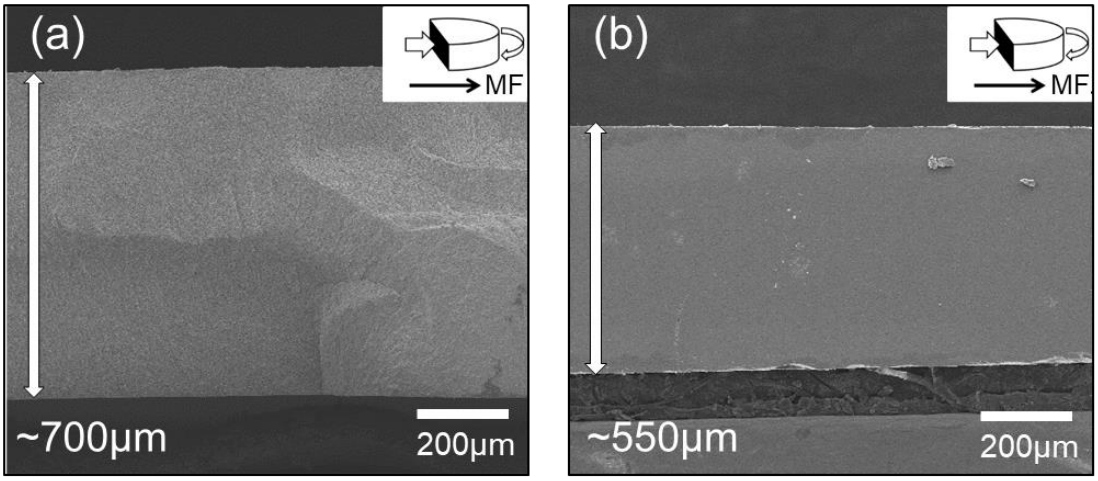

FIGURE 6.13 SEM images of the sintered sample heated at (a) 1000 ºC and (b) 1250 ºC observed from the parallel direction to the magnetic field.

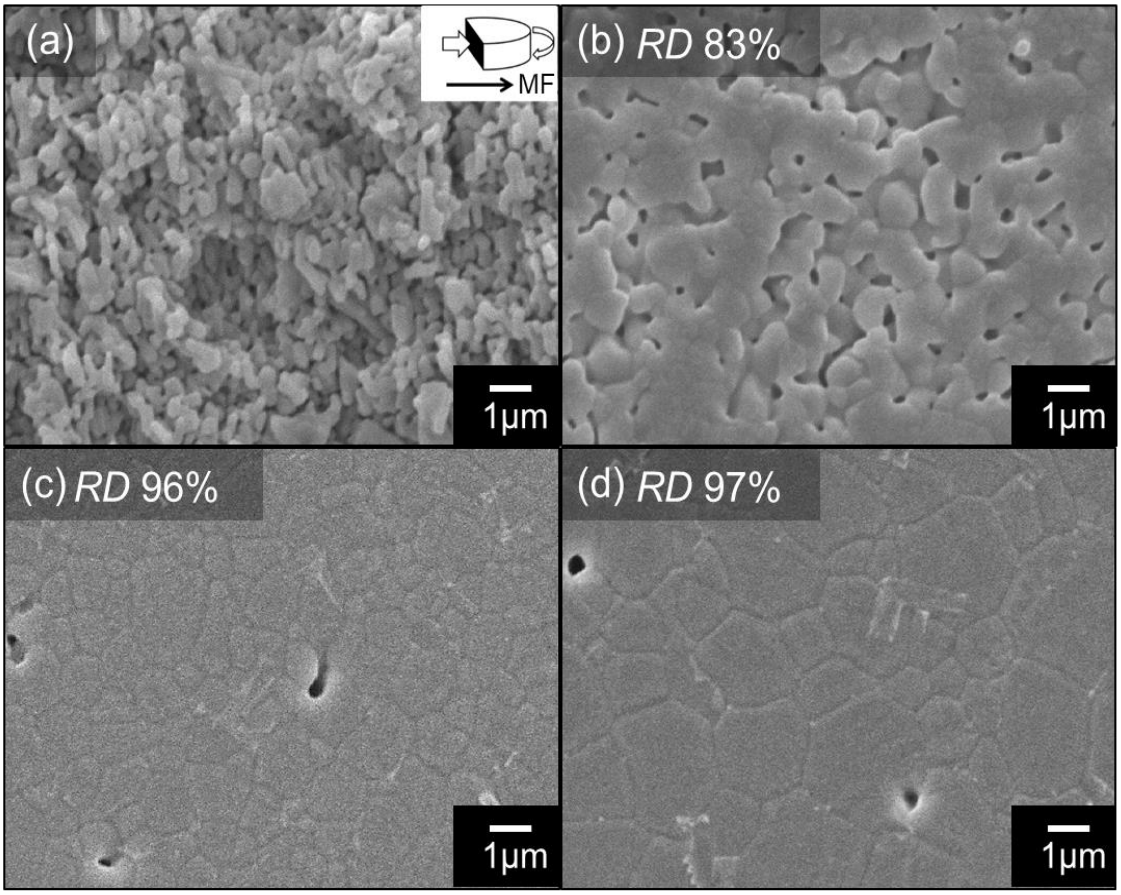

FIGURE 6.14 Microstructure of oriented samples heat treated at (a)1000 ºC, (b)1150 ºC, (c)1200 ºC and (d)1250 ºC for 2 hours. The observed directions is parallel to the magnetic field.

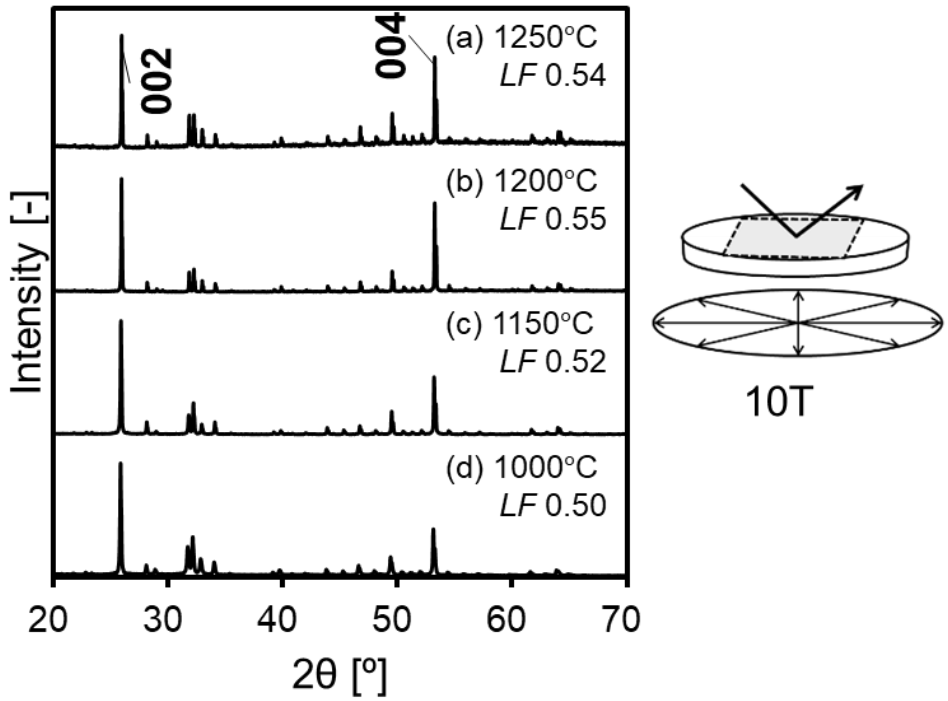

FIGURE 6.15 XRD patterns of oriented samples for various sintering temperature at (a)1250 ºC, (b)1200 ºC, (c)1150 ºC and (d)1000 ºC.

Figure 6.15 shows XRD patterns of oriented ceramics sintered at each temperature in the range from 1000 to 1250 °C. The *c*-axis particle orientation was maintained during sintering. These results indicate that the *c*-axis oriented HAp ceramics could be fabricated by particle orientation and photopolymerization in the rotating magnetic field and subsequent sintering. Furthermore, I suggest that the porous HAp ceramics with a controlled oriented structure for high-performance biomaterials can be fabricated by using this technique in future work.

6.4 CONCLUSIONS

The *c*-axis oriented HAp ceramics were fabricated by colloidal processing using a UV curable resin in a high rotating magnetic field and subsequent sintering. A slurry with high solids concentration was prepared using a UV curable binder as the reactive solvent. The cured depth of the slurry increased with UV irradiation time, and the maximum thickness of the sample was 1.6 mm after UV irradiation for 30 s. The thickness of polymerized compacts depended clearly on the difference in the refractive index between the particles and the UV curable binder. Furthermore, the degree of orientation of the particles increased with increasing exposure time in the high magnetic field, and it saturated at 150 s. This was very similar to the orientation time estimated from the theoretical calculation. The polymerized green compacts were sintered between 1000 to 1250 °C for 2 h. At 1250 ºC, a uniform microstructure was observed after sintering for 2h. Interestingly, the *c*-axis oriented crystal structure was maintained during sintering. This study thus shows that *c*-axis oriented HAp ceramics can be fabricated by photopolymerization reaction in a high magnetic field and subsequent sintering.

REFERENCES

[1] W. Suchanek and M. Yoshimura, J. Mater. Res., 13 (1998) 94-117
[2] H. Aoki, Surf. Sci., 10 (1989) 96-101
[3] M. Aizawa, T. Matsuura and Z. Zhuang, Biol. Pharm. Bull., 36(11) (2013) 1654-1661
[4] T. Kawasaki, M. Nikura and Y. Kobatashi, J. Chromatogr. A, 515 (1990) 125-148
[5] T. Kawasaki, J. Chromatogr. A, 544 (1991) 147-184
[6] T. Nakano, K. Kaibara, Y. Tabata, N. Nagata, S. Enomoto, E. Marukawa and Y. Umakoshi, Bone, 31(4) (2002) 479-487
[7] L. Zylberberg, W. Traub, V. De Buffrenil, F. Allizard, T. Arad and S. Weiner, Bone, 23(3) (1998) 241-247
[8] G. Daculsi and B. Kerebel, J. Ultrastruct. Res., 65(2) (1978) 163-172
[9] M. Iijima, H. Tohda and Y. Moriwaki, J. Cryst. Growth., 116 (1992) 319-326
[10] K. Inoue, K. Sassa, Y. Tokogawa, Y. Sakka, M. Okido and S. Asai, , Mater. Trans., 44(6) (2003) 1133-1137
[11] J. Akiyama, M. Hashimoto, H. Takadama, F. Nagata, Y. Yokogawa, K. Sassa, K. Iwai and S. Asai, 46(11) (2005) 2514-2517
[12] M. L. Griffith and J. W. Halloran, J. Am. Ceram. Soc., 79(10) (1996) 201-2608
[13] T. Chartier, C. Hinczewski and S. Corbel, J. Eur. Ceram. Soc., 19 (1999) 67-74
[14] S. P. Gentry and J. W. Halloran, J. Eur. Ceram. Soc., 35 (2015) 1895-1904
[15] S. P. Gentry and J. W. Halloran, J. Eur. Ceram. Soc., 33 (2013) 1989-1994

Chapter 7

Summary

This present thesis has aimed to develop a novel process with a photopolymerization reaction to shorten the consolidation time in a magnetic field for crystal-oriented ceramics and to elucidate the scientific principle of the fabrication processing from forming to sintering. A particle orientation behavior in a magnetic field and a densification mechanism contributing to structure development during sintering were verified experimentally.

The high concentrated slurry containing $(Sr,Ca)_2NaNb_5O_{15}$ (SCNN) was prepared using a UV curable resin, and the forming method performing the particle orientation in a magnetic field and a photopolymerization reaction was approached. The polymerization by the UV rays achieved to shorten the duration time in the magnetic field for several ten seconds. Next, a theory of rotation behavior of fine particles in a concentrated slurry was proposed. The dependence of the experimental parameters on the orientation behavior of particles in the concentrated slurry was examined experimentally by using the photopolymerization reaction. The results clearly indicated that the orientation time t was proportional to the viscosity of the slurry and the inverse of the square of the magnetic flux density ηB^{-2}, and mostly agreed with the theory. The high influence of solid contents in a slurry on the particle orientation behavior was newly clarified. When the solid concentration in the slurry was low, the orientation time estimated from the experimental data took a long time as compared with that calculated using the applied theoretical equations. It indicated that the increase of a degree of freedom of particles affects the orientation of particles. Furthermore, the densification mechanism leading to the development of crystal-oriented structure during sintering was elucidated by the detailed microstructure observation. The grains in the *c*-axis oriented powder compact preferentially grew along the *c*-axis direction correspond to large shrinkage. The *c*-axis oriented structure was evolved because of the grain growth of oriented particles including random grains. Based on these findings, *c*-axis oriented SCNN laminated ceramic, which has a piezoelectric constant d_{33} of 74.4 pC/N, was fabricated by repeatedly performing the photopolymerization reaction under the magnetic field and followed by sintering. In addition, crystal-oriented bulk green compacts with a thickness of 1.6 mm were fabricated by once polymerization reaction in the magnetic field due to hydroxyapatite (HAp) material system of the low refractive index.

From the above, colloidal processing with a photopolymerization reaction in a magnetic field is an effective technique to provide continuously the particle-oriented green sheets or bodies and is expected to provide continuous mass production. Furthermore, the critical experimental parameter to fabricate crystal-oriented ceramics using magnetic field was elucidated. To fabricate ceramics with a highly oriented and densified microstructure, it is important to design the particle packing structure in a powder compact and to control the structural development during sintering. I hope the results of this study will be valuable information for further development and industrial applications in the future.

The results examined in this present thesis were shown below.

Chapter 1 summarized historically past research of the related topics to crystal-oriented ceramics. The characteristics and problems of the magnetic field alignment technique, which was focused on this thesis, were described. Among them, the objectives of this thesis were described.

Chapter 2 focused on colloidal processing with the photopolymerization reaction in the magnetic field for the fabrication of *c*-axis oriented SCNN ceramics sheets with a thickness of ~ 100 μm. The slurry was prepared from the UV curable acrylic binder, photoinitiator, and dispersant. The amount of photoinitiator and dispersant was optimized to prepare the well-dispersed slurry with high solid concentration. After the particles in the slurry were aligned in the magnetic field, this was consolidated by a UV irradiation for just 30 s. The oriented microstructure in the *c*-axis oriented green sheets was developed during sintering. Also, for SCNN material system, the results indicated that a high degree of orientation in the green sheets prohibited the densification during sintering.

Chapter 3 proposed the theory of the orientation behavior of particles in a slurry, and elucidated experimentally the dependence of a slurry viscosity, a magnetic flux density and a solid concentration in a slurry on orientation behavior of fine particles in concentrated slurries by using the photopolymerization reaction. Form the proposed theory, it expected that the intrinsic magnetic response rate of a particle τ^{-1} was inversely proportional to ηB^{-2}, and the orientation time t was proportional to ηB^{-2}. For the orientation of particles in the 45vol% slurry in the magnetic field, the orientation time t calculated using the theoretical equations was the same order as the experimental data. This means that the orientation behavior was mostly explained by the applied theory. On the other hand, for the slurry with solid contents of < 40 vol%, the orientation time t estimated from the experimental data was longer than that calculated from the theoretical equations. This suggested that a complicated movement of the particles in a slurry

prevents a particle rotation in the magnetic field.

Chapter 4 clarified the mechanism of the oriented structure development in *c*-axis oriented SCNN powder compacts during sintering. The shrinkage and grain growth along the *c*-axis were higher than those along the *a*-axis. The anisotropic microstructure development clearly corresponded to anisotropic sintering shrinkage. The grain growth of large oriented particles with taking surrounding small random particles led to the development of oriented microstructure. To fabricate ceramics with a highly oriented and densified microstructure, it is effective to design the particle-oriented structure in a powder compact looking ahead to the structure development during sintering.

Chapter 5 focused on the fabrication of *c*-axis oriented SCNN laminated ceramics by repeatedly performed the photopolymerization reaction in the magnetic field and followed by sintering. The degree of orientation in the sintered ceramic was 0.69 and the relative density was 96 %. Its piezoelectric d_{33} constant was 74.4 pC/N and larger than that of the randomly oriented structure, 12.8 pC/N. The results clarified that the piezoelectric properties of crystal-oriented ceramics prepared by the photopolymerization reaction could be improved.

Chapter 6 described the fabrication of *c*-axis oriented HAp bulk compacts with a thickness of approximately 1.6 mm by once photopolymerization reaction under the magnetic field. The thickness of polymerized compacts depended on the difference in the refractive index between the particles and the UV curable binder. The oriented structure in the green compacts was obtained, and it was maintained during sintering. This result indicated that the colloidal technique with the photopolymerization reaction under the influence of the magnetic field could be widely applied for many types of materials.

Chapter 7 summarized this thesis.

LIST OF PUBLICATIONS

1. **Shoko Baba**, Tomohiro Harada, Hiroyuki Shimizu, Yutaka Doshida and Satoshi Tanaka, “Colloidal processing using UV curable resin under high magnetic field for textured ceramics”, Journal of the European Ceramic Society, Vol. 36, Issue 11 (2015), pp. 2739-2743 ……**Chapter 2**
2. 馬場 翔子, 田中 諭,“磁場中配向成形におけるスラリー温度の影響”, 粉体工学会誌, 第 53 巻 12 号 (2015), pp. 791-796 ……**Chapter 3**
3. **Shoko Baba** and Satoshi Tanaka, “Particle rotation in colloidal processing under as strong rotating magnetic field”, Langmuir, Vol. 34 (2017), pp. 6862-6469 ……**Chapter 3**
4. **Shoko Baba**, Alexandre Maître, Nicolas Pradeilles, Guy Antou and Satoshi Tanaka, “Graded evolution of anisotropic microstructure during sintering from crystal-oriented powder compact”, International Journal of Applied Ceramic Technology, Vol. 17 (2020), pp. 677-684, DOI: 10.1111/ijac.13360 ……**Chapter 4**
5. **Shoko Baba** and Satoshi Tanaka, “Fabrication of c-axis oriented hydroxyapatite ceramics in a rotating high magnetic field using photopolymerization”, Journal of the European Ceramic Society (submitted) ……**Chapter 6**

Other related paper

1. Antoine Pringuet, Takuma Takahashi, **Shoko Baba**, Yuta Kamo, Zenji Kato, Keizo Uematsu and Satoshi Tanaka, “Fabrication of Transparent Grain-Oriented Polycrystalline Alumina by Colloidal Processing”, Journal of the American Ceramic Society, Vol. 99, Issue 10 (2015), pp. 3217-3219

Patent

1. 特願 2019-057008
   発明名称 結晶軸配向ゼオライト膜およびその製造方法
   発明者 田中 諭, 馬場 翔子, 渡邉 壽也, 内田 雅人
2. 特願 2019-219421
   発明名称 結晶軸配向ゼオライト膜およびその製造方法
   発明者 田中 諭, 馬場 翔子, 内田 雅人, 渡邉 壽也

PRESENTATIONS IN CONFERENCES

1. **馬場 翔子**, 田中 諭, 土信田 豊, 原田 智宏, 清水 寛之, “磁場中紫外線硬化成形法による配向セラミックスの作製”, 日本セラミックス協会秋季シンポジウム, (2015)
2. **馬場 翔子**, 田中 諭, 原田 智宏, 清水 寛之, 土信田 豊, “紫外線硬化成形法を用いた磁場中での粒子配向挙動の解析”, 日本セラミックス協会年会, (2016)
3. **馬場 翔子**, 田中 諭, 原田 智宏, 清水 寛之, 土信田 豊, “回転磁場コロイド成形における粒子配向挙動の解析”, 粉体工学会春季研究発表会, (2016)
4. **馬場 翔子**, 田中 諭, 土信田 豊, 原田 智宏, 清水 寛之, “紫外線硬化樹脂を用いた回転磁場成形による配向セラミックスの作製”, 日本セラミックス協会秋季シンポジウム, (2016)
5. **馬場 翔子**, 田中 諭, “紫外線硬化樹脂を用いた回転磁場成形における粒子配向挙動の解析”, 日本セラミックス協会年会, (2017)
6. **馬場 翔子**, 田中 諭, “磁場内粒子の配向時間に及ぼす磁束密度の影響”, 日本セラミックス協会秋季シンポジウム, (2017)
7. **馬場 翔子**, 田中 諭, “高磁場を用いた透明配向多結晶ルビーの作製”, 日本セラミックス協会年会, (2018)
8. **馬場 翔子**, 田中 諭, Alexandre Maître, Nicolas Pradeilles, Guy Antou, “*c*-軸配向$(Sr,Ca)_2NaNb_5O_{15}$ の焼結による粒子配向構造発達”, 日本セラミックス協会秋季シンポジウム, (2018)
9. **Shoko Baba** and Satoshi Tanaka, “Particle orientation behavior in colloidal processing with UV curable binder under a rotating magnetic field”, 7th International GIGAKU Conference in Nagaoka (IGCN2018), Nagaoka, Niigata, (October 2018)
10. **Shoko Baba** and Satoshi Tanaka, “Fabrication of *c*-axis oriented $(Sr,Ca)_2NaNb_5O_{15}$ in rotating high magnetic field with stereolithography”, 43th International Conference and Exposition on Advanced Ceramics and Composites (ICACC2019), Daytona Beach, Florida, USA, (January-February 2019)
11. **馬場 翔子**, 田中 諭, “回転磁場中光造形法による *c* 軸配向$(Sr,Ca)_2NaNb_5O_{15}$の作製と特性評価”, 日本セラミックス協会年会, (2019)
12. **Shoko Baba**, Alexandre Maître, Nicolas Pradeilles, Guy Antou and Satoshi Tanaka, “Anisotropic sintering for c-axis particle-oriented

$(Sr,Ca)_2NaNb_5O_{15}$ ceramics", XVI Conference and Exhibition of the European Ceramic Society (XVI ECerS Conference), Torino, Italy, (June 2019)

13. **Shoko Baba** and Satoshi Tanaka, "Fabrication of c-axis oriented bulk hydroxyapatite in rotating high magnetic field using UV curable binder", The 13th Pacific Rim Conference of Ceramic Societies (PACRIM13), Okinawa, Japan, (October-November 2019)
14. 馬場 翔子, 田中 諭, "回転磁場成形における粒子回転挙動の解析", 日本磁気科学学会年会, (2019)
15. 馬場 翔子, 田中 諭, 渡邉 壽也, 内田 雅人, "磁場を用いた *c* 軸配向モルデナイトゼオライト膜の作製と特性評価", 日本セラミックス協会年会, (2020)